SAPIENZA
UNIVERSITÀ DI ROMA

Fluid behaviour in biological confinement: gating of the hERG potassium channel via Molecular Dynamics simulations and network analysis

PhD school in Science and Technology for the Industrial Innovation
PhD program in Theoretical and Applied Mechanics (XXXV cycle)

Flavio Costa
ID number 1658103

Advisor
Prof. Alberto Giacomello

Co-Advisor
Dr. Carlo Guardiani

Academic Year 2021/2022

Fluid behaviour in biological confinement: gating of the hERG potassium channel via Molecular Dynamics simulations and network analysis

PhD thesis. Sapienza University of Rome

© 2022 Flavio Costa. This document is distributed under the terms of the Creative Commons Attribution License (CC BY).

This thesis has been typeset by LaTeX and the Sapthesis class.

Author's email: f.costa@uniroma1.it

Contents

List of Publications

Journal Articles

[1] Carlos AZ Bassetto, **Flavio Costa**, Carlo Guardiani, Francisco Bezanilla, and Alberto Giacomello. Noncanonical electromechanical coupling paths in cardiac hERG potassium channel. *Submitted*, October 2022.

[2] **Flavio Costa**, Carlo Guardiani, and Alberto Giacomello. Exploring K v 1.2 Channel Inactivation Through MD Simulations and Network Analysis. *Frontiers in molecular biosciences*, 8, 2021.

[3] **Flavio Costa**, Carlo Guardiani, and Alberto Giacomello. Molecular dynamics simulations suggest possible activation and deactivation pathways in the hERG channel. *Communications biology*, 5(1):1–11, 2022.

[4] **Flavio Costa**, Riccardo Ocello, Carlo Guardiani, Matteo Masetti, and Alberto Giacomello. Identification of the binding mode of the hERG channel activator RPR260243. *In preparation.*

Conference Publications

[1] Carlo Guardiani, **Costa, Flavio**, and Alberto Giacomello. A computational approach to characterize gating in ion channels. In *APS March Meeting Abstracts*, volume 2021, pages E08–008, 2021.

[2] **Costa, Flavio**, Carlo Guardiani, and Alberto Giacomello. Exploring hERG gating through MD simulations and network analysis. In *European Biophysics Journal with Biophysics Letters*, volume 50, pages 105–105. Springer One New York Plaza, Suite 4600, New York, NY, US, 2021.

List of Figures

List of Tables

Abstract

The boundary between biological cells and the external environment is represented by a lipid membrane that does not allow the passage of polar molecules such as ions and water. However, their orchestrated movements are fundamental for the function of vital organs. For this reason, there are transmembrane proteins called as "ion channels" that forming pores on the cells allow the ion to flow through these impermeable membranes.

Normally, an ion channel has three functional states: the open state that is permeable to ions, the closed state where they can not pass, and the inactivated state that is structurally similar to the open state but functionally closed. The mechanisms by which an ion channel switches from the open to the closed state and vice versa are defined as "activation" and "deactivation" respectively, while the transition from the open to the inactivated state is defined as "inactivation". All these transitions define the so-called "gating" mechanism.

The main features of the biological channels are the selectivity, the sensing and the regulation of their gating mechanism. The characterization of these properties gives the possibility to extract the basic principles to design bioinspired artificial channels that can be used, for example, to study various molecules in confined spaces and in real time by current measurements. The biomimetic channels are becoming the focus of attention for bionanotechnology because they offer greater flexibility in terms of shape and size, robustness and surface properties boosting, in this way, their fields of application.

In this context, we studied the human ether-à-go-go–related gene channel (hERG, KCNH2, or $K_v11.1$) that is a voltage-gated potassium channel involved in the heart contraction. hERG malfunctions are associated with severe pathologies such as long QT syndrome type 2 (LQTS2) that can be due to loss-of-function mutations (congenital LQTS2) or channel blockage induced by unspecific interactions with medications (acquired LQTS2). These conditions have been described to promote arrhythmia and sudden cardiac death.

Based on the protein architecture, hERG is a member of the non-domain-swapped channel family where the sensor of the channel is always connected covalently to the pore of the same subunit. The gating mechanism of these channels is still not completely characterized. Due to its importance in human health, we decided to focus on hERG gating addressing the problem with a theoretical approach based on Molecular Dynamics simulations. Using a network analysis, we microscopically identified the kinematic chain of residues that couple the sensor of the channel to the pore. In general, our results could provide the basis for studying the coupling mechanisms between sensors and pores in ion channels to explain the origin of

inherited and induced channelopathies such as LQTS2.

Chapter 1

Introduction

1.1 Ion channels

Membranes of all living cells are composed by a 3 nm thick lipid bilayer that is impermeable to polar molecules. However, ions can pass through these hydrophobic barriers using proteins such as pumps, transporters, and channels. Precisely, proteins that form pores on membranes and allow the ions to move passively across the membranes are defined as "ion channels" [79]. They are gated pores because their opening and closing can be regulated by different stimuli, for example by a ligand or changes in the voltage gradient across the membrane. Ion channels are found in animals, plants, and bacteria, and regulate the homeostasis of all the living systems [7].

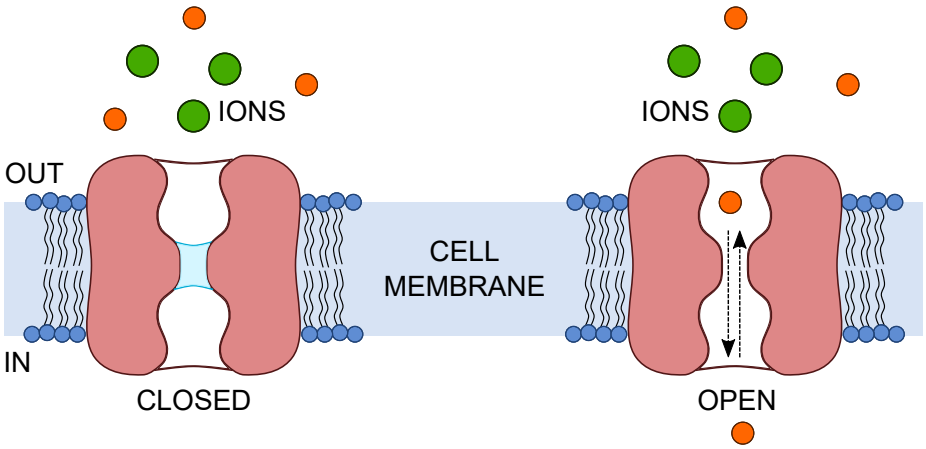

Figure 1.1. Schematic representation of ion channels in the open and closed state.

1.1.1 Role

Ion channels are a special class of proteins that generate holes in the cell membrane allowing the flow of ions. This is of key importance for the transmission of nerve signals. The neurons have a star-shaped body called "soma" and a long tail called

"axon". The membrane of the axon has a negative resting potential. When the action potential arrives, voltage dependent sodium channels close to the soma open, allowing sodium ions to flow in (Figure 1.2 point 1). In such a way, the membrane potential becomes less negative (depolarization). The sodium ions entered into the axon hillock spread downstream depolarizing the next stretch of membrane (Figure 1.2 point 2). This causes the opening of other voltage dependent sodium channels and a further inflow of sodium (Figure 1.2 point 3). With this mechanism the depolarization wave reaches the end of the axon where it induces the release of a neurotransmitter that binds to ligand-gated channels of the next neuron (called post-synaptic). The opening of the ligand-gated channels activates the propagation of the depolarization wave in the next neuron. In this way neuron after neuron the nerve impulse reaches the actuator organs like the muscles that react contracting. In order for the neuron to carry other signals, the resting potential of the membrane must be restored. This is achieved through the closing of sodium channels and the opening of potassium channels that allow the outflow of potassium ions (repolarization).

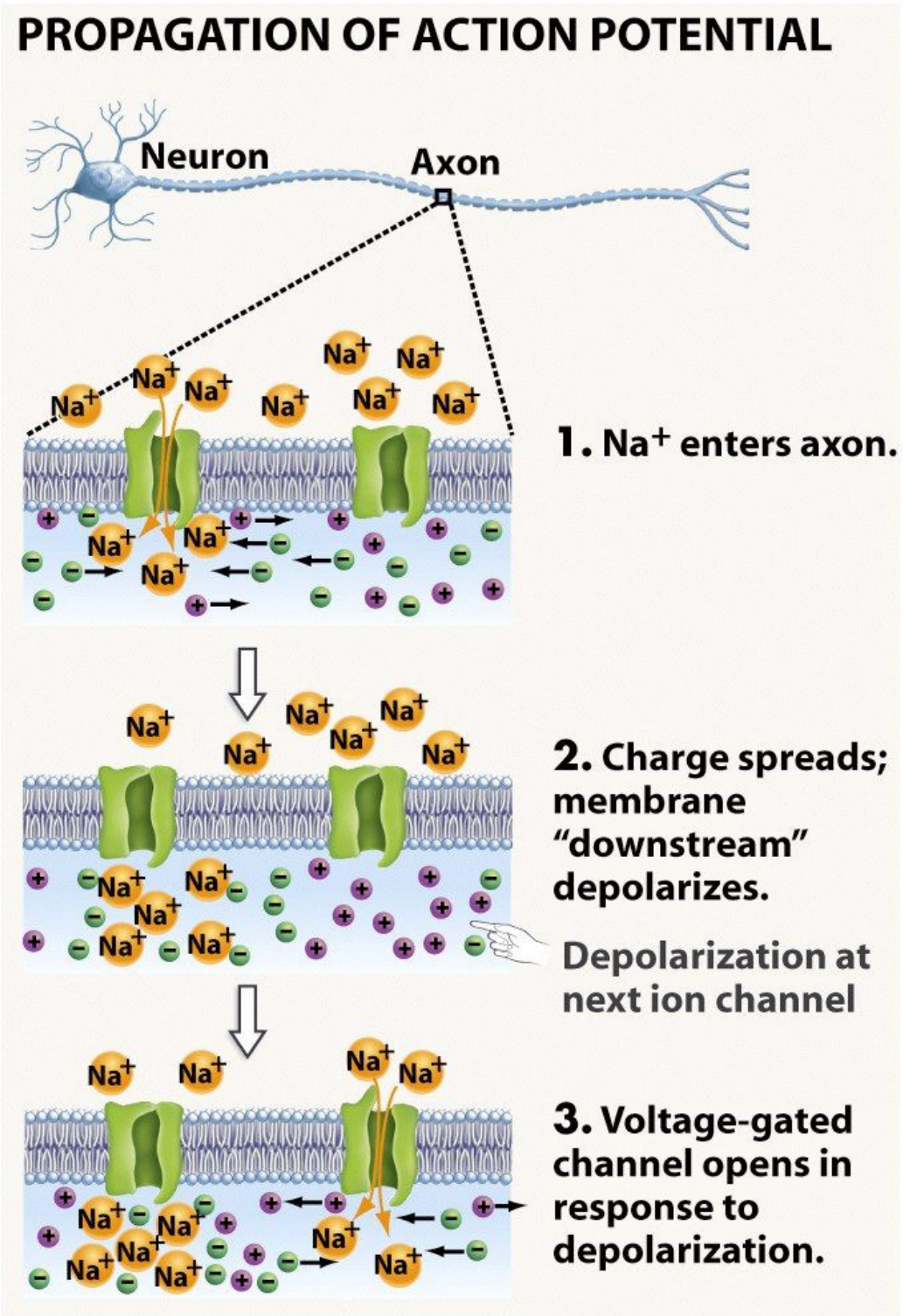

Figure 1.2. Schematic illustration of the onset and propagation of the action potential [79].

1.2 Permeability

The ion's flow through an open channel depends on the permeability of the channel. The direction in which the ions move is governed by the electrochemical gradient across the membrane that allows ions to move across the membranes without spending energy.

1.2.1 The electrochemical gradient

The electrochemical gradient is determinant in the ion movements. It is determined by the ion concentrations on each side of the membrane. To understand its role in the channel permeation, a container divided into two equal parts by an impermeable membrane can be imaged. The first compartment contains a high concentration of positively charged molecules while the other has a very low concentration of the same molecules. If the membrane becomes permeable to that molecules, they will move down their concentration gradient from the higher concentration to the lower one. Moreover, since these molecules have a charge, their movements will be also influenced by the electric field across the membrane. So, the ions will be attracted towards a negative charge but repulsed by a positive one. As a consequence of that, the total force on an ion will therefore be determined by the combined effects of the chemical and electrical gradients. At the equilibrium potential, the electrical and chemical forces on ions match and there is no flux.

1.2.2 The equilibrium potential

The potential at which the electrical force on the ions balances the opposing force of the concentration gradient is known as "equilibrium potential" and it is given by the Nernst equation [200]. For an ion X, the equilibrium potential E_X is:

$$E_X = \frac{RT}{zF} ln \frac{[X]_{out}}{[X]_{in}} \tag{1.1}$$

where R is the gas constant, T is the absolute temperature, z is the valency of the ion, and F is the Faraday constant. $[X]_{out}$ and $[X]_{in}$ are the external and internal concentrations of X, respectively. For example, the equilibrium potential of potassium (K^+) ions is -84 mV because its physiological concentrations are 140 mM inside the cell and 5 mM outside the cell, respectively. This value is close to the resting membrane potential of most cells that assumes values between -60 to -100 mV.

Many channels are permeable to more than one ion. In this case, the equilibrium potential is a function of both the electrochemical gradient for the single ions and of their relative permeabilities. It is given by the Goldman-Hodgkin-Katz voltage equation [154]:

$$E = \frac{RT}{F} ln \left(\frac{\sum_i^n P_{M_i^+} [M_i^+]_{out} + \sum_j^m P_{A_j^-} [A_j^-]_{in}}{\sum_i^n P_{M_i^+} [M_i^+]_{in} + \sum_j^m P_{A_j^-} [A_j^-]_{out}} \right) \tag{1.2}$$

where $P_{M_i^+}$ and $P_{A_j^-}$ are the permeabilities for the monovalent positive (M_i^+) or negative (A_j^-) ionic species, $[M_i^+]_{in\ or\ out}$ and $[A_j^-]_{in\ or\ out}$ are the intracellular and extracellular concentrations of that ions.

The relevant ions in living cell processes are sodium (Na^+), potassium (K^+), calcium (Ca^{2+}), chloride (Cl^-), and magnesium (Mg^{2+}). Values of their concentration and the corresponding equilibrium potentials are summarized in Table 1.1.

Ion	Extracellular Concentration (mM)	Intracellular Concentration (mM)	Equilibrium Potential (mV)
Sodium	135-145	12	+66
Potassium	3.5-5.0	140	-93
Calcium	2.25-2.50	10^{-4}	+135
Chloride	115	2.5-50	-42
Magnesium	1.0	0.5	+9

Table 1.1. Concentrations and equilibrium potentials of ions. Extracellular concentrations refer to the typical range found in human blood while intracellular concentrations are given for a typical mammalian cell. For calcium ions, the intracellular concentration refers to free ions. The equilibrium potentials are calculated at physiological temperature [7].

1.2.3 Selectivity

Ion channels can be classified based on the ions they allow to pass. Some of them are permeable to both cations and anions while others are selective only to one type. The main determinant of this property is the diameter of the channel pore and the size of the ion: large ions are physically unable to permeate small pores. In this view, ion channels act as molecular sieves [79]. However, in most cases they do not simply act as pores that allow free passage of ions below a certain size. They discriminate the ions to permitted to flow. Thus, potassium channels are permeable to K^+ but not to Na^+ ions even if the latter have a smaller ionic radius of 0.95 Å. This behaviour depends on a specific region known as "Selectivity Filter" that selects ions. In potassium channels it is characterized by a particular signature sequence of amino acids, TVGYG or SVGFG, that is highly conserved with the exception that a valine in prokaryotes is often substituted with an isoleucine in eukaryotes [53]. Here, the K^+ ions that are moving through the channel encounter spaced layers of carbonyl oxygen atoms and a single layer of threonine hydroxyl oxygen atoms that create four K^+ ion binding sites numbered 0 to 4 from the extracellular to the intracellular side. At these sites, K^+ ions bind in a dehydrated state surrounded by eight oxygen atoms from the protein (Figure 1.3). Those oxygen atoms mimic the hydrated K^+ ion's hydration shell allowing the ions to move through the channel without large energetic cost [209].

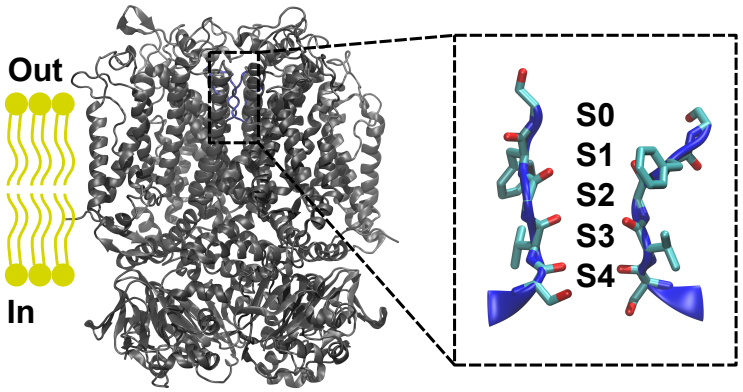

Figure 1.3. Selectivity Filter of potassium channels. Residues that form the ion's binding site (S0 to S4) are shown in licorice.

1.3 The gate

Ion channels can be permeable (conductive) or impermeable (non-conductive) to ions. In other words, they can be functionally open or closed. The transitions between these states is known as "gating". However, a condition of metastability characterizes the behaviour of ion channels because multiple states can exist between the open and the closed states [102]. For this reason, it is not possible to know *a priori* in which state an ion channel is at any time. It is only possible to collect statistics that describes the probability of an ion channel to be in the open or closed state, the average duration of each opening or closing event, and the frequency of the transition between states. Generally, the ion channels remain closed without an external stimulus. When it occurs, the stimulus increases the probability of a channel to be in the open state by stabilizing the open state or destabilizing the closed state. In this way, it determines the channel opening.

Ion channels are classified based on the different stimuli that trigger the channel to open:

1. Voltage-gated channels where the membrane potential variation determines the channel opening. These channels are closed at the resting potential of the cell but when it changes, they undergo a series of conformational changes in the protein structure that result in the opening of the pore. This voltage-dependent activation is sometimes followed by another conformational transition, denoted as inactivation, that occurs very rapidly and blocks the ion passage. The ion movements determine a modification of the membrane potential that returning to the initial values allows the channel to move to the initial closed configuration. Both depolarization and hyperpolarization can activate ion channels. Most of voltage-gated channels are permeable to potassium and sodium but there is a little group of chloride channels that is less known;

2. Ligand-gated channels are opened by the binding of extracellular or intracellular molecules. When the ligand binds the channel, the resulting conformational changes on the protein structure triggers the channel to open. The most common extracellular ligands are the neurotransmitters acetylcholine, glutamate

and glycine while the intracellular ones are AMP, calcium and ATP;

3. Thermosensitive channels are influenced by temperature variations;

4. Mechanosensitive channels that open or close in response to mechanical stimuli such as stretching or deformation of the cell membranes.

The main property of the gating mechanism is that it can be modulated. The most common regulators are cytosolic molecules [172].

Hydrophobic gating

Recently, another gating mechanism has been discovered in different ion channels [5, 73]. It is defined as "hydrophobic gating" because it is characterized by an unusual behaviour of water in narrow hydrophobic pores (below 14 Å). At the nanoscopic level, the water molecules exhibit liquid–vapor transitions and randomly switch between wet and dry states. In this way, the formation of bubbles inside the pore of the channels stop the ions flow determining the closed state of the channel. The transition from the closed to the open state is characterized by little modifications on the protein structure that allow the breaking of the bubble and consequently the ions to flow. This event can be determined by increasing the diameter of the channel or the hydrophilicity of the narrowest region of the pore and by the membrane potential variation across the pore (electro-wetting) [160, 69].

1.4 Potassium channels

Potassium channels are the most prevalent channels in living systems, found in bacterial, archeal and eukaryotic cells. Mutations on their genes lead to a number of human diseases that impair the nerve impulse transmission, the heartbeat, and muscle contraction [115].

1.4.1 Classification

They can be classified in four families based on the stimulus that triggers the pore opening [16]:

1. Calcium-activated potassium channels (K_{Ca}) that open in response to the presence of intracellular Ca^{2+}. They are divided into two groups [197]: the first group includes the small and intermediate conductance channels that are activated only by low concentrations of calcium; the second includes the large conductance channels that are activated by both membrane depolarization and cytosolic level of calcium [137]. The latter group includes the BK channels that regulate the circadian behavioral rhythms and neuronal excitability. They are composed by four subunits organized in different domains: the Voltage Sensor Domain that senses the membrane potential variation, the Pore Domain that opens and closes the channel, and a cytoplasmic C-Terminal Domain with a calcium bowl that binds Ca^{2+} ions and triggers the channel to open or close depending on the calcium concentration [45].

2. Inwardly rectifying potassium channels (K_{ir}) that pass current more easily in the inward direction (into the cell) than out of the cell. When the membrane is hyperpolarized, these channels support the flow of potassium into the cell pushing the membrane potential back to the resting potential. These channels consist of four α-subunits containing two-transmembrane segments (M1 and M2) and a pore loop in between. They participate in many functions such as the control of the resting potential in astrocytes, coupling of energy metabolism with membrane excitability, and maintenance of potassium homeostasis [104].

3. Two-pore channels (K_{2P}) that are normally open or possess high basal activation, such as the resting potassium channels or leak channels that set the negative membrane potential of neurons. K_{2P} channels contain α-subunits consisting of four transmembrane segments and two Pore Domains. They are important for setting the resting membrane potential and contribute to module the action potential duration and responsiveness to synaptic stimuli [70].

4. Voltage-gated potassium channels (VGKC or K_V) that open or close in response to membrane potential variations [185]. They are characterized by six or seven transmembrane α-helices and a single pore region where the S4 helix contains positively charged residues that sense the potential variation. The S1-S3 portion contains negatively charged and aromatic residues that coordinate the movements of S4 [207]. K_V channels play a key role in membrane excitability and duration of the action potential. They include several subfamilies (K_V1-K_V12) consisting of different α-subunits that associate in a tetramer configuration. An important example is the *Shaker*-like K_V family (K_V1-K_V8 subunits) which contributes to hyperpolarize neurons after the depolarization [185].

1.4.2 Architecture of VGKC structures

In VGKC the membrane potential variation is sensed by charged amino acids called "gating charges" on helix S4 that is part of a region denoted as Voltage Sensor Domain (VSD). On the other hand, the pore is located in the Pore Domain (PD), usually delimited by helices S5 and S6. The coupling of the helix S4 motions to the opening of the channel pore is the basis of the gating mechanism [19] and since these portions of the protein are sometimes very distant, the voltage-gated channels can be considered as allosteric machines [12]. Currently, there are two architectures identified amongst VGKC [12]:

1. Domain-swapped channels where the peripheral VSD contacts the PD of a neighboring subunit (Figure 1.4 right). This architecture is typical of the K_V1-K_V9 *Shaker*-like channels [89, 119, 119, 181], the voltage-gated sodium and calcium channels [202, 180] and the Transient Receptor Potential channels (TRP) [124]. Here, the long α-helical element L45 connects the VSD to the PD acting as a mechanical lever that pushing onto the S6 helix opens the channel.

2. Non-domain-swapped channels where the VSD contacts the PD from the same subunit (Figure 1.4 left). This is typical of K_V10 [199] and K_V11 [195] but it is also present in the Slo1 and SK calcium activated channels [80, 108], the

sodium-dependent potassium channel Slo2.2 [81] and the HCN1 activated by hyperpolarization cation channel [113]. Here, the loop L45 is non α-helical and too short to act as a mechanical lever so an alternative gating mechanism is to be sought for.

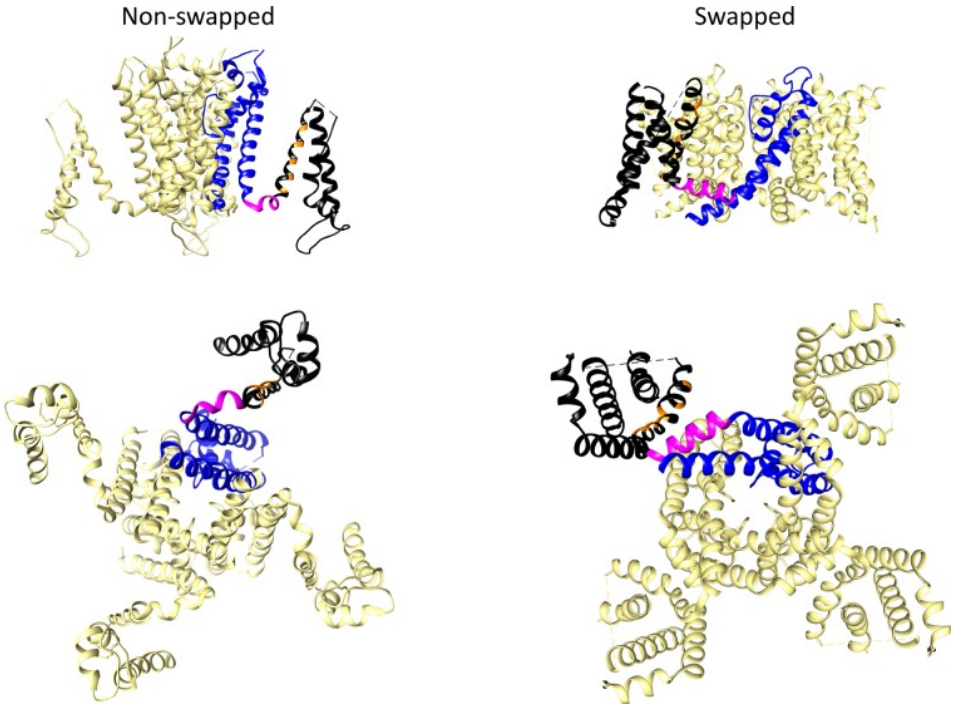

Figure 1.4. Comparison of non-domain-swapped and domain-swapped architectures of K_V channels. Left, hERG (PDB ID: 5VA2) non-domain swapped structure. Right, K_v1.2 (PDB ID: 2A79) domain-swapped structure. Only the transmembrane core domains are depicted viewed from the membrane plane (top) and from the cytoplasmic side (bottom). One of the subunits is shown coloured with the pore domain (PD) structures in blue, the S4–S5 linker in magenta, and the voltage sensing domain (VSD) in black. Orange is used to mark the position of positively charged residues in the S4 transmembrane helix of the VSD. Figure from [11].

1.5 The K_v1.2 channel

The KCNA2 gene encodes the K_v1.2 channel, a mammalian voltage-gated K^+ channel featuring up to 80% homology with the *Drosophila* Shaker channel [178]. It is widely expressed in mammals by visceral smooth muscle cells [193] and neurons of the central and peripheral nervous system [140]. Its defections/malfunction are linked to neuronal deficiency inducing encephalopathies, ataxia, cerebellar atrophy [135], and especially childhood epilepsy [129].

1.5.1 Structure

Based on the experimental structure [34], the K_v1.2 channel is characterized by four identical subunits made of six trans-membrane alpha helices each. There are

three functional domains: the T1 domain at the amino-terminus, the Voltage Sensor Domain (VSD) that encompasses helices S1 to helix L45 and is sensitive to the membrane potential variation triggering the channel to open, and the Pore Domain (PD) delimited by the S5 and S6 alpha helices with the P-Loop and the Selectivity Filter (SF) (Figure 1.5a). It is a domain-swapped channel where the peripheral VSDs interact with the PDs of the *neighbouring* subunit determining the channel opening [12].

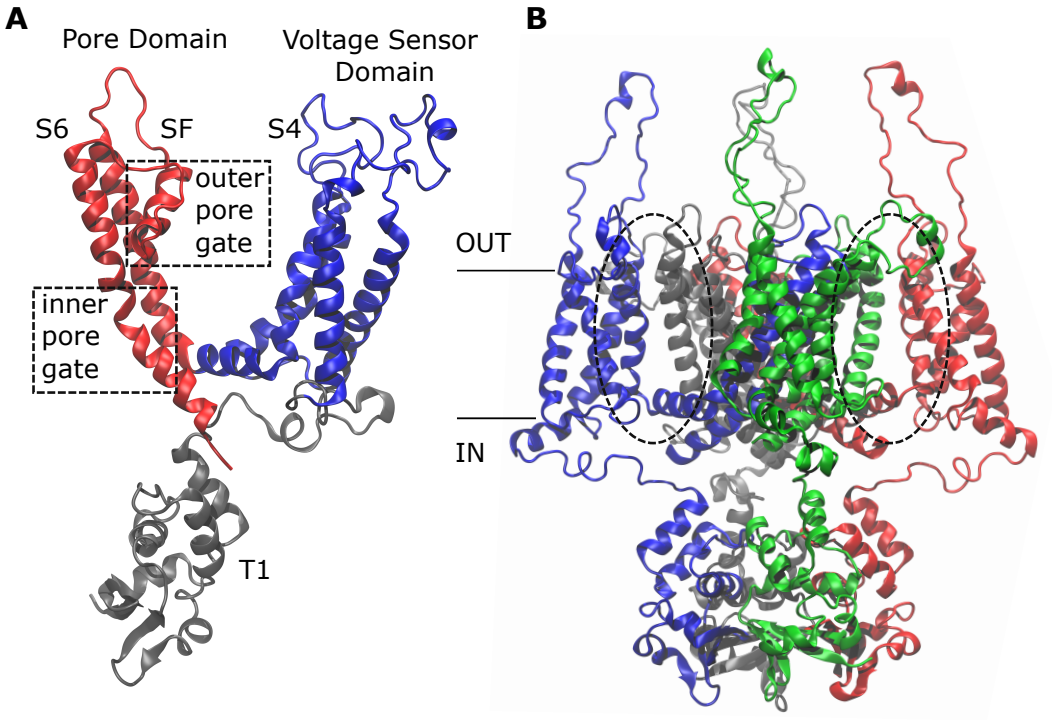

Figure 1.5. Side view of $K_v1.2$ channel. The single subunit **(a)** is coloured by domain: in grey, the T1 domain at the N-term; in blue, the Voltage Sensor Domain (VSD) ranging from helix S1 to loop L45, including the positively-charged helix S4; in red, the Pore Domain (PD), composed of helix S5, P-Loop, Selectivity Filter, and helix S6. The whole protein **(b)** is coloured by subunit: the first subunit in blue, the second in red, the third in gray and the fourth in green. Note that the color code has a different meaning in the two sub-figures.

1.5.2 Gating

The $K_v1.2$ gating is characterized by the transitions between three functional states: closed, open, and inactivated. The transition open-to-inactivated is defined as "inactivation" and it is regulated by the membrane potential variation [142, 120]. There are two types of inactivation: the slow C-type inactivation that depends on structural modification of the SF that closes the outer pore gate and the rapid N-type inactivation where the N-terminus occludes the intracellular mouth of the channel [157]. The transitions open-to-closed and closed-to-open are defined as "deactivation" and "activation", respectively. Here, the ion permeation is regulated by the bending of the S6 alpha helices (at the bottom of S6) [118, 53, 48, 119, 88]

that closes the inner pore gate of the channel. The C-type inactivated state plays a key role in the kinetic behaviour of the channels because it is reached immediately after the inner gate opening and, likewise, it allows the channel to close leading the conformation of the inner gate towards the closed state [134, 44]. Despite its central role in channels function, the molecular determinants of the C-type inactivation remain quite elusive. Based on the KcsA studies about the influence of the inner pore gate on the conformation of the outer pore gate [44], it has been demonstrated that in Shaker the residue I470 at the bottom of S6 helix plays a critical role in the C-type inactivation: when the pore opens, this residue modifies its side-chain orientation and physically makes contact with the SF inducing a constriction capable of stopping the ion flow [151]. These experimental evidences support the idea of a different coupling mechanism implicated in the C-type inactivation driven by the modifications of the S6 helices after the channel opening and not by a direct coupling with the VSD.

1.6 The human Ether-à-go-go-related gene channel

The KCNH2 gene encodes a voltage-gated potassium channel, the human ether-à-go-go-related gene channel (hERG), that is involved in the repolarization phase of the action potential in the heart cells [46, 187]. The impairment of its activity due to genetic mutations or aspecific interactions with a wide range of chemicals [158, 166] results in severe channelopathies linked to arrhythmia referred to as Short and Long QT Syndromes (SQTS and LQTS2, respectively).

1.6.1 Structure

A cryo-electron microscopy structure of the hERG channel was firstly obtained by Wang and MacKinnon [195] at 3.8 Å resolution (PDB ID: 5VA2). Recently, another structure has been solved at 3.9 Å resolution in complex with the blocker Astemizole (PDB ID: 7CN0) [6]. Both of them represent hERG in the open state, indeed the overall transmembrane domains are similar (Root-Mean-Squared Deviation of 884 C_α atoms is 1.40 Å). However, they present some differences: the VSD are slightly shifted outward in 7CN0 than in 5VA2; the atom-atom distances between two diagonally opposed subunits containing carbonyl oxygens in the SF are wider in 7CN0 than in 5VA2; finally, the K^+ density is observed only in 7CN0. However, these differences may be caused by differences in the detergent used and/or grid preparation.

hERG is a homotetrameric voltage-gated potassium channel with each of the four identical subunits consisting of six transmembrane alpha helices (Figure 1.6). They can be grouped in four domains: the Voltage Sensor Domain (VSD), encompassing helices S1 to S4, that senses the membrane potential variation and triggers the channel to open; the Pore Domain (PD), including helices S5 and S6, that forms the pore of the channel where the ions pass [24]; the N-terminus Domain containing the PerArntSim (PASD) [27]; the C-terminus Domain (CTD) containing the cyclic-nucleotide-binding homology domain (CNBHD) [24] along with a distal C-terminal ER retention signal (RXR) [105] and coiled-coil domain (CCD) [87]. Between the S5 and S6 helices, there are the extracellular P-Loop and the Selectivity Filter (SF)

that allow the channel to select for potassium over sodium by thousand-fold [123]. Interestingly, the KCNH2 gene encodes two isoforms of the hERG channel, both of

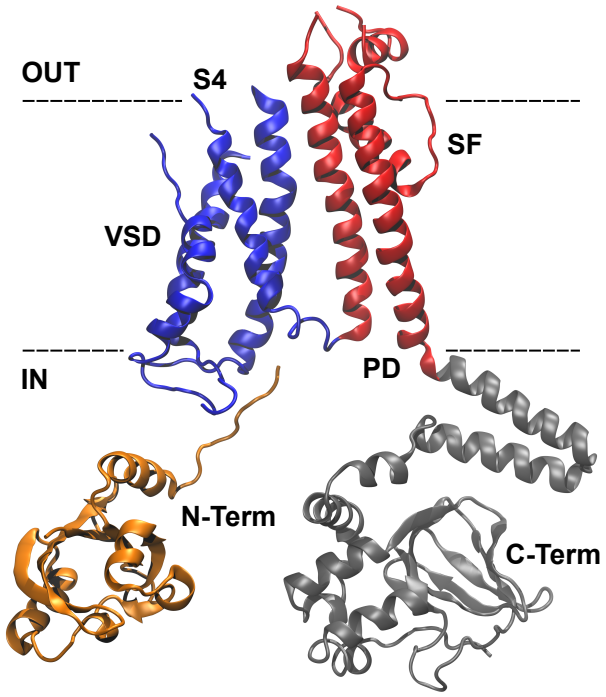

Figure 1.6. Single subunit of hERG experimental structure [195] (PDB ID: 5VA2) colored by domain: in orange, the N-term Domain; in gray, the C-term Domain; in blue, the Voltage Sensor Domain (VSD) ranging from helix S1 to loop L45, including the positively charged helix S4; in red, the Pore Domain (PD), composed of helix S5, P-Loop, Selectivity Filter, and helix S6.

which are expressed in human cardiac tissue [93].The most recently solved isoform was named as hERG-b and it differs from the first-discovered hERG-a isoform in lacking the entire PASD, being 340 residues shorter [110, 176, 145]. Both of them are critical for human cardiac repolarization as testified by a hERG-b specific mutation associated with intrauterine fetal death [92].

1.6.2 Function

The hERG channel is involved in the regulation of cellular excitability in neural, cardiac, pancreatic and smooth muscle tissues [159, 22, 175]. However, its function is best known in the case of the cardiac action potential (Figure 1.7a) that is controlled by different currents, including sodium, calcium and potassium currents, determining the phenotype of the ventricular action potential that has a duration of 350 ms [166]. It contributes to the QT interval in the ECG trace that describes the heart activity (Figure 1.7b). The ventricular action potential has five phases (Figure 1.7a): in phase 0 the influx of sodium ions determines the rapid depolarization of the membrane [167]; in phase 1, the transient outward potassium current and rapid inactivation of sodium channels lead to the partial repolarization of the membrane [139]; in phase 2, known also as plateau phase, the membrane potential declines slowly under the

effect of the balance between the influx of Ca^{2+} ions and the efflux of K^{+} ions [57, 94]; in phase 3, the calcium channels close, the potassium channels open and the membrane potential starts to repolarize [86]; finally, in phase 4 the membrane potential reaches the resting state [78]. Disruption of the hERG repolarizing current

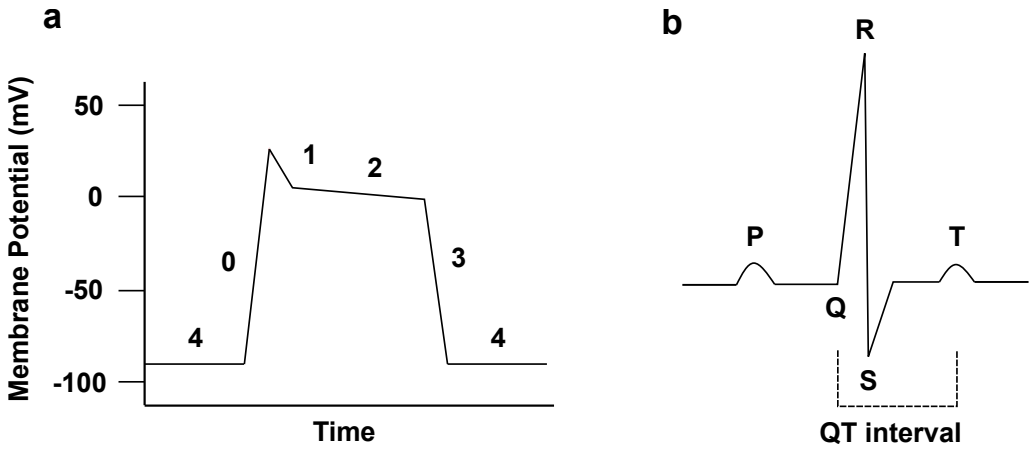

Figure 1.7. Human ventricular myocyte action potential (**a**) and ECG trace for a single cardiac cycle (**b**). The numbers and letters overlaid to the plots highlight the phases of the action potential (0-4) and ECG trace (P-T).

can dramatically alter the action potential duration and morphology predisposing individuals to cardiac arrhythmia.

1.6.3 Gating

The hERG channel is involved in phase 3 of the ventricular action potential and it cycles over 3 different states: closed, open, and inactivated (Figure 1.8). In the

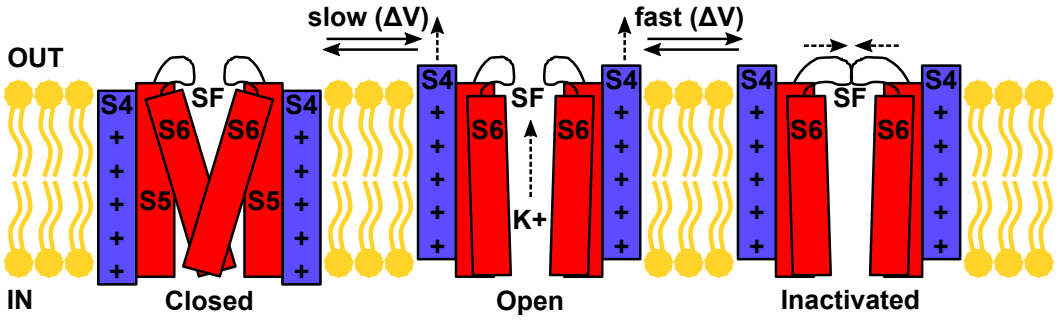

Figure 1.8. The hERG channel scheme of the gating mechanism. The helix S4 of the VSD is shown in blue while the PD encompassing S5 and S6 helices is coloured in red.

closed state the pore is closed and the S4 helices are in their resting conformation. On the other hand, in the open state they are in the activated conformation and the pore is able to conduct ions. The inactivated state is structurally very similar to the open state but functionally closed. Currently, no experimental structures of the closed and inactivated states of hERG are available. However, it has been suggested that the inactivation depends on a little constriction occurring at the SF

that blocks the ion's flow [112]. The transition from the open to the closed state and *vice versa* are defined as "deactivation" and "activation", respectively. The transition from the open to the inactivated state occurring at the level of the SF is known as "C-type inactivation". The channel is closed at negative voltages, for example -80 mV. Membrane depolarization to potentials more positive than -60 mV slowly opens the channel and allows the outward flux of K^+ ions according to the electrochemical driving force. As the membrane potential is progressively depolarized to more positive potentials, the inactivation occurs very rapidly and the channel enters in a non-conductive configuration [112]. When the membrane starts repolarizing, hERG quickly re-opens recovering from inactivation and favouring the rapid repolarization that terminates the cardiac action potential [194]. The hERG gating is different from that of the most other voltage-gated potassium channels: first of all, the inactivation is much faster than the slow activation and it reduces the outward conductance at depolarized potentials prolonging the phase 2 of the action potential; secondly, the recovery from the inactivation is faster than deactivation [166].

Activation

The activation of the hERG channel is voltage-dependent and occurs very slowly. It is associated to structural modification of the VSD that senses the membrane potential variation and moves up and down allowing the channel to open and close. The helix S4 of the VSD carries five positively charged residues that sense the voltage changes: K525, R528, R531, R534 and R537. They are separated by a critical phenylalanine (F463) on helix S2 that acts as the gating charge transfer centre (GCTC). In the open conformation only two of the five positively charged residues are below the critical F463 ring (Figure 1.9). It is not clear how many basic residues must be below the critical F463 in the closed state but using the limiting slope method the gating charge of the hERG channel was experimentally estimated to be ∼6.4e [207]. This results in a displacement of S4 helix by one or two positively charged residues under the F463. Mutations of S4 residues alter the voltage-dependence of the channel impairing its gating mechanism [206]. Precisely, mutagenesis experiments showed that mutating K525, R528 and R531 the activation process is modified because these residues are important in the displacement of S4. In particular, K525 stabilizes the closed state by non-electrostatic functional interactions with the GCTC [179, 155]. This residue is peculiar of the hERG channel and may contribute to the slow activation. The K525R mutation destabilizes the closed state reducing the rate of deactivation [35]. In the same way, K538 at the bottom of the S4 helix is unusual and plays a role in stabilizing the closed state of the channel *via* interactions with the negatively charged residues on the S2 helix [35].

Generally, in domain-swapped channels, the motions of the VSD are transduced to the PD *via* the helix L45. However, in the non-domain-swapped hERG channel (Figure 1.4), the loop L45 is non α-helical and too short to induce the pore opening as a mechanical lever. Nevertheless, several studies showed its crucial role in the activation of hERG as well as the proximity of the loop to the distal part of the S6 helix [163]. For example, in D540K mutant there is a destabilization of the closed

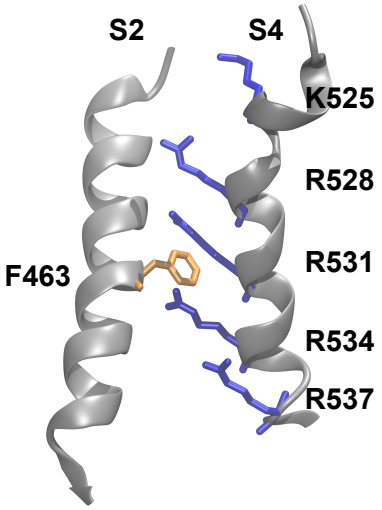

Figure 1.9. Gating Charge Transfer Center (GCTC) with the critical phenylalanine F463 (in orange) on S2 helix and the positively charge residues (in blue) on S4 helix in the open state of the channel.

state at hyperpolarized potentials [163]. Charge reversing and charge neutralizing mutations of the R665 residue on S6 helix re-established the closed state stability at hyperpolarized potentials suggesting that the interactions between the L45 and S6 play a role in stabilizing the closed state. Then, G546L determines a stabilization of the open state favouring the activation process [183]. Recently, it has been shown that cutting the loop L45 at different points influences the gating of hERG in different ways: Y545 split channels were able to activate while cutting near the S4-end of the loop L45 increased the destabilization of the closed state [47].

This evidence suggests that helix S4 and loop L45 are relevant in the activation mechanism of hERG channel. However, the molecular determinants of the slow rate of this process remain quite elusive and need to be investigated.

Deactivation

As the activation, the deactivation of the channel is very slow and this is important for producing the resurgent current during the repolarization of the cardiac action potential [163]. The regulation of this process is associated to different regions on the hERG structure. Mutations on the N-term region accelerate the deactivation while those on the PASD restore the slow deactivation in N-term deleted fast deactivating channels [27]. This behaviour is influenced by interactions between the PASD and the CTD [173] and between the PASD and the loop L45 [194, 47]. Therefore mutations of D460 and D509 on helix S2 destabilize the activated state and accelerate the deactivation kinetics [116].

Inactivation

Contrary to other potassium channels, the hERG inactivation occurs very rapidly. Experimental studies suggest that this mechanism resembles the C-type inactivation of Shaker channels in terms of sensitivity to K^+ ions and to mutations on the P-Loop [66]. It has been shown that the Shaker C-type inactivation is characterized by three different steps where the channels assume three different protein conformations moving from the open to the inactivated state: an initial state that is highly selective for K^+ ions, an intermediate inactivated state that is less permeable to K^+ ions but more permeable to Na^+ ions, and a final more stable inactivated state that is non-conductive [196]. Mutational analyses showed that the hERG rapid inactivation is characterized by two sequential rearrangements on the protein structure that allow to distinguish two mechanisms: the initial "P-type inactivation" where the channel becomes permeable to Na^+ ions and quickly reaches a less stable inactivated state upon depolarization; the "C-type inactivation" where the channel reaches a more stable inactivated state that is impermeable to all ions [120]. The C-type inactivation has been shown to be associated to a constriction on the SF at the level of G626 residues [112]. This constriction is stabilized by the F627 side-chain rotation and the hydrogen bond between Y616 and N629 as key determinants and it is sensitive to the ion occupancy on the SF [169]. Several mutants have been identified to reduce the inactivation rate, S631A, N588K and N588E, or completely abolish it, S620T and G628/S631C [63, 66, 147]. The hERG inactivation is suggested to be characterized by two different mechanisms that both involve a single gate, with the P-type inactivation closing the gate and C-type inactivation stabilizing the gate's non-conductive conformation. However, the molecular determinants of this process remain elusive and not completely understood.

1.6.4 Dysfunction and Long QT Syndrome type 2

hERG malfunctions are commonly associated with severe conditions including arrhythmia diseases such as the Long QT Syndrome type 2 (LQTS2), sudden infant death syndrome (SIDS) and short QT syndrome (SQTS), as well as various forms of cancer, epilepsy and schizophrenia [164]. To date, over 600 mutations in the KCNH2 gene encoding the hERG channel have been identified to be the cause of these channelopathies. Not all of them show a loss-of-function phenotype, suggesting that some mutations may be benign sequence variants or single-nucleotide polymorphisms (SNPs) [2, 189].

The majority of the mutations causes the LQTS2 that is characterized by the prolongation of the QT interval measured by the electrocardiogram signal (Figure 1.7b) [3]. Prolongation of the QT interval and therefore the action potential can lead to an arrhythmia called "torsade de pointes", which can further degenerate into ventricular fibrillation and in extreme cases cause sudden cardiac death. This channelopathy affects an estimated 1 in 5,000-10,000 people worldwide [166].

The LQTS2-linked mutations can be classified into four groups depending on the molecular mechanism that is impaired: class 1, abnormal transcription or translation; class 2, deficient protein trafficking; class 3, abnormal channel gating/kinetics; class 4, altered channel permeability [3]. It has been shown that 62% of mutations are

missense, 24% are frameshift and 14% are a combination of nonsense mutations, insertions or deletions and splice site mutants in the gene. Most of these are localized in the N-term and C-term domains but ∼30% are in the transmembrane domains (VSD and PD) [20]. In terms of molecular mechanism, the largest part of the mutations invoke a class 2 mechanism due to protein misfolding and endoplasmic reticulum-associated degradation. Recent studies identified a small but non-negligible group of class 3 mutations that affect the gating [3]. They can be found in the N-term and C-term domains as well as in helix S6 of the pore. The I711V and R835W mutations alter the hERG gating channel and are localized in cytosolic domain. They determine a faster deactivation while the inactivation remains unchanged [3]. On the other hand, the G584S mutation is localized on the PD and affects the inactivation [136]. Similarly, T613A in the P-Loop was found to cause a high effect on the inactivation [156]. Moreover, mutations impairing the gating mechanism have been also mapped on helices S1 [152] and S4 [130] where they accelerate the deactivation process.

1.6.5 Drug interactions

The hERG channel seems to be the only voltage-gated potassium channel that has a high tropism for external molecules. Indeed, the LQTS2 can also be induced by the interaction with a wide range of aspecific drugs including anti-arrhythmics, antibiotics, antihistamines, antidepressants, antimicrobials, anticancers, and antimalarials [165, 158]. The severity of this condition, defined as Acquired LQTS2, is such that regulatory agencies prescribe the testing of all new drugs for hERG block. In this context, the FDA and a consortium of other regulatory agencies have promoted the Comprehensive in Vitro Proarrhythmia Assays (CiPA) [32, 41], a large scale screening program to test candidate new drugs for cross-reactivity and block of hERG channel. Consequently, much interest has been raised to identify the structural basis of this unusual susceptibility to interactions, with approaches ranging from experimental electrophysiology to *in silico* modeling.

hERG blockers

In general, hERG is characterized by a large inner cavity where the external molecules can enter. Experimental studies demonstrated that hERG blockers, such as Cisapride and Dofetilide [96, 63] sterically block the K^+ ions by interacting with residues on S6 helix (G648, Y652, F656) and residues at the C-term side of the SF (T623, S624, V625) [95, 109, 133, 148] *via* π-cation or π-π interactions [59, 177]. Interestingly, some compounds exhibit a greater affinity depending on the state of the channel. For example, the BeKm-1 scorpion toxin binds hERG in the closed state [131] but the majority of blockers exhibit a high-affinity blockade preferentially for the inactivated state. Nevertheless, the molecular determinants of this behaviour remain quite elusive [9].

hERG activators

In contrast to numerous hERG blockers, many molecules have been discovered to increase hERG activity by modulating channel gating. They become of interest

due to their potential use for people affected by LQTS2 where they can reverse the disease. The hERG activators can be grouped in four classes depending on the mechanism of action [164]: (1) drugs that slow the rate of channel deactivation such as RPR260243 [97], Ginsenoside Rg3 [36] and LUF7346 [162]; (2) molecules that attenuate the inactivation such as PD118057 [208] and NS1643 [30]; (3) drugs that determine a negative shift of the voltage dependence of activation such as Mallotoxin and KB130015 [205, 68]; (4) molecules that increase the channel open probability such as SB-335573 [52]. Experiments suggest that the activators bind to a hydrophobic pocket located outside the central cavity between the P-Loop and helices S5 and S6 of two adjacent subunits by interacting with L553, F557, N658 and V659 as for RPR260243 [150] or with L646 for PD-118057 [150, 149, 71, 67].

In conclusion, the molecular mechanisms by which drugs can interact with hERG prolonging the QT interval or enhancing its activity are complex and not completely clear. However, they could potentially cause a paradigm shift in the clinical management of LQTS2 or perhaps other disorders where hERG channel function is implicated.

1.7 Thesis objectives and outline

The objective of this thesis is to elucidate the gating of the non-domain-swapped hERG voltage-gated K^+ channel. The relevance of this work is associated to the physiological importance of hERG in the generation of the delayed rectifier current (IK_r) that determines the plateau period of the cardiac action potential [163]. To achieve this goal, we addressed the problem using a combination of Molecular Dynamics simulations and theoretical network analyses in different steps:

1. First of all, we implemented the network analysis studying the $K_v1.2$ channel whose gating has been extensively characterized by experiments. This step allows to validate our computational protocol since our results show a good agreement with the experiments. Then, it also enables a comparison between the gating and inactivation mechanisms of domain-swapped channels (like $K_v1.2$) and non-domain-swapped channels (like hERG). This step is described in sections 3.1;

2. Then, we focused on the hERG channel. Here, since the only experimental structure of hERG is available in the open state [195], we integrated the structural data by building a homology model for the closed state of the channel based on the experimental measurement of the gating charge [207]. It is described in section 3.2;

3. We reproduced the transition from the open to the closed state of the channel *via* Targeted Molecular Dynamics simulations. The contact analysis of these trajectories allowed us to formulate two hypothetical activation/deactivation mechanisms involving the loop L45, the C-Linker and helices S5 and S6 that are consistent with previous experimental works [126, 47, 186]. See section 3.3;

4. We identified the activation and inactivation paths *via* a network approach previously used for domain-swapped channels [60, 198]. Interestingly, in both of them a very similar path that resembles the noncanonical gating path found in Shaker channels [28, 13] was identified that involves the interfaces S4/S1 and S1/S5. These results are shown in section 3.4;

5. Then, to test the reliability of our results, we simulated some mutants and split channels [47] that have been experimentally characterized as shown in sections 3.5 and 3.6;

6. Finally, we described the transition from the open to the closed state focusing on some macroscopic observables that are relevant in the activation mechanism as reported in section 3.7.

The main findings and the results of this thesis are discussed in the Discussion and Conclusions sections.

Chapter 2

Methods

2.1 Brief overview of Molecular Dynamics

In last years, the recent advances in molecular biology and biochemistry have provided detailed information about the structure of many molecules essential for life, including proteins and nucleic acids. Although these structures solved with high resolution are very useful, they represent a static "photograph" of systems that, indeed, are flexible entities where the dynamics plays a key role in their function [83]. Molecular Dynamics (MD) simulations have become a widely used tool to investigate biological and chemical systems [72] allowing to simulate the time evolution of a set of interacting atoms by integrating the differential equations embodied in Newton's second law:

$$F_i = m_i \frac{d^2 r_i(t)}{dt^2} \tag{2.1}$$

where m_i and r_i are the ith atom mass and position, respectively, and F_i is the force acting on the atom due to the interactions with the others. These equations are integrated using a finite difference method that introduces a discretization δt of the temporal axis and given an initial set of positions at time t as well as an appropriate potential energy function (the force field), the force acting on each atom is computed. Then, the acceleration is computed to derive the positions and velocities at $t + \delta t$, where the δt is the time-step of the simulation. The computer repeats the calculation on each atom for many steps producing an ordered list of $3N$ atom coordinates for each simulation time. The resulting output is a trajectory that contains a set of configurations distributed according to a statistical distribution function or statistical ensemble that is a collection of various microstates of an equilibrium macroscopic system as determined by the constraints operating on the system [98]. In general, MD is a powerful tool that allows to connect the protein structure to the dynamics and function with an atomic resolution, acting in this way as a computational microscope [54]. In the context of ion channels, MD simulations allow to understand the basis of their gating mechanisms. For example, the most studied channel is KcsA where it has been firstly shown that the opening depends on the bending of S6 helices that delimited the pore [14]. In the same way, MD simulations combined with free-energy calculations revealed with atomistic resolution how the VSD moves during the activation process [49] or the basis of the selectivity [101].

2.1.1 General set-up for MD simulation

Nowadays the most used packages in MD simulations are AMBER [29], CHARMM [25] and NAMD [138]. In all cases, to set up the MD simulation, an initial configuration of particles that form the system is needed. Normally, the structure of large macromolecules like proteins can be obtained from the Protein Data Bank, a database where data obtained by X-ray crystallography, the Nuclear Magnetic Resonance (NMR) spectroscopy and cryo-electron microscopy (Cryo-EM) are accessible on the Internet website https://www.rcsb.org/.

2.1.2 Initialization: the Maxwell-Boltzmann distribution

The initial velocities are generated by sampling the Maxwell-Boltzmann distribution at the simulation temperature. Considering a single component of velocity, v_x, the probability distribution is:

$$f(v_x)dv_x = \frac{1}{\sqrt{2\pi}\sqrt{\frac{kT}{m}}} e^{-\frac{v_x^2}{2\frac{kT}{m}}} \tag{2.2}$$

where k is the Boltzmann constant, T the absolute temperature and m the mass. The higher is the temperature, the higher is the velocity of the atoms. Assuming that the velocities are equally and independently distributed along the three dimensions of the space, the probability of a velocity vector (v_x, v_y, v_z) is:

$$f(v_x, v_y, v_z)dv_x dv_y dv_z = f(v_x)dv_x f(v_y)dv_y f(v_z)dv_z \tag{2.3}$$

that yields:

$$f(V)d^3v = (\frac{m}{2\pi kT})^{\frac{3}{2}} e^{-(\frac{mv^2}{2kT})} d^3v \tag{2.4}$$

where $f(V) = f(v_x, v_y, v_z)$ and $d^3v = dv_x, dv_y, dv_z$.

2.1.3 Force fields

The main ingredient in MD simulations is the force field as a combination of mathematical formula and associated parameters that are used to describe the energy of the system as a function of its atomic coordinates. The interactions between the atoms that form the system originate forces which act upon them determining their motion. As the atoms move, their relative positions change and the forces change as well. Choosing the most appropriate force field is crucial because it is necessary to computationally reproduce the real behaviour of the molecules under specific conditions [75]. The potential energy term can be split in two terms that include bonded interactions referring to covalently bonded atoms (stretching, bending and dihedral potentials) and non-bonded interactions involving atoms not covalently connected (Lennard-Jones and electrostatic potentials):

$$U = U_{bonded} + U_{non-bonded} \tag{2.5}$$

The bonded interactions are intra-molecular interactions that refer to covalent bonds between atoms in a single molecule:

$$U_{bonded} = U_{bending} + U_{stretching} + U_{dihedral} \tag{2.6}$$

they include the stretching energy $U_{stretching}$ that describes the oscillations of the bond length, the bending energy $U_{bending}$ that refers to the angle variation of two bonds between three atoms, and the torsional energy $U_{dihedral}$ describing the torsional rotation of four atoms on a central bond.
On the other hand, the non-bonded interactions refer to intra- and inter-molecular interactions.They are typically written as:

$$U_{non-bonded} = U_{LJ} + U_{Coulomb} \tag{2.7}$$

U_{LJ} is the Lennard-Jones potential:

$$U_{LJ} = 4\epsilon \left[\left(\frac{\sigma}{r} \right)^{12} - \left(\frac{\sigma}{r} \right)^{6} \right] \tag{2.8}$$

where ϵ corresponds to the depth of the potential well, σ is the distance at which the particle-particle potential energy is zero, and r is the distance between two interacting particles. It approximates the Van der Waals dispersion forces.
On the other hand, $U_{Coulomb}$ is the electrostatic potential:

$$U_{Coulomb} = \frac{q_i q_j}{r} \tag{2.9}$$

where q is the charge of the i or j particle and r is the distance between them.
All these factors contribute to the force calculation of the system.

2.1.4 Integration methods

There are many algorithms of finite difference methods for integrating the equation of motion used in MD simulations in order to compute the positions and the velocities at time $t+\delta t$. All of them assume that positions $r(t)$, velocities $v(t)$ and accelerations $a(t)$ can be approximated as Taylor series expansions [107]:

$$\begin{aligned} r(t+\delta t) &= r(t) + v(t)\delta t + \frac{1}{2}a(t)\delta t^2 + \frac{1}{6}b(t)\delta t^3 + \cdots \\ v(t+\delta t) &= v(t) + a(t)\delta t + \frac{1}{2}b(t)\delta t^2 + \cdots \\ a(t+\delta t) &= a(t) + b(t)\delta t + \cdots \end{aligned} \tag{2.10}$$

The Verlet algorithm [191] is frequently used. It uses the position $r(t)$ and the acceleration $a(t)$ at time t and the position at the previous step $r(t-\delta t)$ to compute the position at time $t+\delta t$ and the velocity at time t:

$$\begin{aligned} r(t+\delta t) &= r(t) + v(t)\delta t + \frac{1}{2}a(t)\delta t^2 + \cdots \\ r(t-\delta t) &= r(t) - v(t)\delta t + \frac{1}{2}a(t)\delta t^2 - \cdots \end{aligned} \tag{2.11}$$

By summing these two equations, it is possible to compute the position at $t+\delta t$:

$$r(t+\delta t) = 2r(t) - r(t-\delta t) + a(t)\delta t^2 \tag{2.12}$$

and by subtracting them, the velocity at time t is:

$$v(t) = \frac{[r(t+\delta t) - r(t-\delta t)]}{2\delta t} \tag{2.13}$$

This algorithm is fast and has some advantages, for example the modesty of storage requirements. However, a problem with this Verlet scheme is that the velocities are not synchronized with the positions and it requires the positions at time $t - \delta t$. This means that at the beginning of the simulation $r(t_0 - \delta t)$ should be known that can be computed using the initial position and velocity $r(t_0 - \delta t) = r(t_0) - v(t_0)\delta t$. However, in this case, the computed velocity always lags a step back with respect to the position.

To solve this problem, several variants of the Verlet algorithm have been developed [171] such as the leap-frog algorithm that makes use of the velocity at half time intervals. This is done in two steps. At first, the velocity at time $t + \frac{1}{2}\delta t$ is computed from $a(t)$ and $v(t - \frac{1}{2}\delta t)$:

$$v(t + \frac{1}{2}\delta t) = v(t - \frac{1}{2}\delta t) + a(t)\delta t \tag{2.14}$$

then the position at time $(t + \delta t)$ is obtained with:

$$r(t + \delta t) = r(t) + v(t + \frac{1}{2}\delta t)\delta t \tag{2.15}$$

This algorithm yields more accurate positions because they are calculated using velocity at closer time.

2.1.5 Time-step and time-scale limitations

Another crucial factor in MD simulations is the time-step. If it is too short the simulation will explore only a small part of the conformational space around the initial structure. On the other hand, if it is too long the atom clashes determine force instabilities. Usually, the time-step assumes values between 1 and 2 fs for atomistic simulations [55]. Generally, the time-step chosen is equal to one tenth of the period of the fastest oscillations. If we consider that the C-H bond vibrates with a period of 10 fs, the typical time-step in MD simulations is 1 fs [99]. A short time-step is the major bottleneck of the simulation procedure: it implies that MD simulations are currently limited to nanoseconds or, at most, microseconds, far away from the time scales of biological processes. Generally, since the chemical bonds between hydrogen and heavy atoms are represented with holonomic constraints that eliminate the problem of the high oscillation frequencies, a time-step of 2 fs is often used.

2.1.6 Constant temperature and constant pressure

Finally, in MD simulations it is necessary to specify the conditions of the simulation. The natural ensemble is the NVE ensemble where the number of particles N, the volume V and the energy of the system E are maintained constant over the simulation. However, for a biological system, it is useful to regulate the temperature

T and the pressure P or the volume V, consequently sampling in the so-called NPT ensemble or the NVT ensemble, respectively.

The temperature of the system is related to the time average of the kinetic energy [174] and this prompts to easiest way to control the temperature of the system: rescaling the velocities. If the velocities are multiplied by a factor λ at time t, the temperature variation is:

$$\Delta T = \frac{1}{2}\sum_{i=1}^{N}\frac{2}{3}\frac{m_i(\lambda v_i)^2}{Nk_B} - \frac{1}{2}\sum_{i=1}^{N}\frac{2}{3}\frac{m_i(v_i)^2}{Nk_B} = (\lambda^2 - 1)T(t) \tag{2.16}$$

In this way, in order to move the current temperature $T(t)$ to the desired value T^*, the velocities are multiplied at each time-step by a factor λ:

$$\lambda = \sqrt{\frac{T^*}{T(t)}} \tag{2.17}$$

An alternative way to fix the temperature is to couple it to an external heat bath, applying the so-called Berendsen thermostat [17]. Here, the change in temperature is given by:

$$\frac{dT(t)}{dt} = \frac{1}{\tau}(T_{bath} - T(t)) \rightarrow \Delta T = \frac{\delta t}{\tau}(T_{bath} - T(t)) \tag{2.18}$$

where τ is the coupling parameter between the bath and the system and T_{bath} is the temperature of the external bath. Then, the velocities are scaled at each time-step as follows:

$$\lambda = \left[1 + \frac{\delta t}{\tau}\left(\frac{T_{bath}}{T(t)} - 1\right)\right]^{\frac{1}{2}} \tag{2.19}$$

In the same way, it can be desirable to control the pressure. The system is immersed in a reservoir and the external pressure may be imposed *via* a physical boundary or wall that is present between the system and surroundings. The boundary sets the system volume and allows the system to fluctuate against the imposed pressure. In the Berendsen method [17] the system is coupled to a pressure bath, similar to the heat bath, so the pressure is obtained as follows:

$$\frac{dP(t)}{dt} = \frac{1}{\tau_p}(P_{bath} - P(t)) \rightarrow \Delta P = \frac{\delta t}{\tau_p}(P_{bath} - P(t)) \tag{2.20}$$

where τ_p is the pressure coupling constant, P_{bath} is the pressure of the bath and $P(t)$ is the pressure of the system at time t. Volume is then rescaled by:

$$\lambda = 1 - \kappa_T\frac{\delta t}{\tau_p}(P - P_{bath}) \tag{2.21}$$

where κ_T is the isothermal compressibility that describes the change of the volume as response to the pressure.

Another popular thermostat is based on Langevin equation that couples the system with a heat bath with which it exchanges heat keeping the temperature constant:

$$m_i\dot{v}_i = F_i - m_i\gamma_i v_i + R(t) \tag{2.22}$$

where γ_i is a friction coefficient quantifying the strength of coupling with the heat bath and $R(t)$ is a random force modelling collisions with other particles. From this equation it is clear that the total force $m_i\dot{v}_i$ does not simply coincide with the interaction term F_i (the negative gradient of the force field), but there are other contributions deriving from the coupling with the bath.

There are many methods to maintain constant the pressure [43]. NAMD provides constant pressure simulation using a modified Nose-Hoover method in which Langevin dynamics is used to control fluctuations in the barostat. This method should be combined with a method of temperature control, such as Langevin dynamics, in order to simulate the NPT ensemble. The Langevin piston Nose-Hoover method is a combination of the Nose-Hoover constant pressure method [128] with piston fluctuation control implemented using Langevin dynamics [58].

2.2 Computational protocol for $K_v1.2$ channel

2.2.1 Production of the open state

The initial configuration of $K_v1.2$ was taken from the experimentally solved open structure (PDB ID 3LUT) [34]. Using the CHARMM-GUI [90, 91], it was embedded in bilayers of 880 1-palmitoyl-2-oleoyl-sn-glycero-3-phosphocholine lipids with 65,408 TIP3P water molecules and 0.15 M of KCl to form a simulation box of ca. $150 \times 150 \times 175$ Å totalling 259,933 atoms. The APBS server [8] was used to analyse the protonation states of residues: all aspartates and glutamates were ionized; H271, H378, H486 were predicted to be in the δ protonation state; H264 was assigned to the ϵ protonation state. Then, the channel was equilibrated in the NPT ensemble for 100 ns. Mutants were produced from the pre-equilibrated wild type system. At first, they were equilibrated for 6.5 ns in the NPT ensemble applying a time-varying harmonic restraint on each mutated residue and on its neighbours within a cutoff distance of 5.0 Å. The force constant, initially set to 10 kcal/mol/Å^2, was decreased by 2 units every 0.5 ns of this simulation and then they were equilibrated for 50 ns in the NPT ensemble.

2.2.2 Contact map

The contact map analysis was carried out computing for each couple of residues the probability to be in contact during the equilibrium simulations. Precisely, two residues were considered to be in contact when a pair of heavy atoms of the side-chains was closer than 5.0 Å for at least 75% of the trajectory.

2.2.3 Network analysis

For the network analysis, the protein was represented as a graph [21] where nodes correspond to residues and edges to interactions between pairs. Edge weights were calculated using: $\mathrm{d_{ij}} = -\log|\mathrm{Corr_{ij}}|$ where $\mathrm{Corr_{ij}}$ is the correlation coefficient, that is the normalized covariance of C_α positions:

$$\mathrm{Corr_{ij}} = \frac{\langle(\vec{r}_i - \langle\vec{r}_i\rangle)(\vec{r}_j - \langle\vec{r}_j\rangle)\rangle}{\sqrt{\langle(\vec{r}_i - \langle\vec{r}_i\rangle)^2\rangle\langle(\vec{r}_j - \langle\vec{r}_j\rangle)^2\rangle}} \tag{2.23}$$

where $\vec{r}_i$ and $\vec{r}_j$ are the position vectors of the i and j residues and $\mathrm{Corr}_{\mathrm{ij}}$ assumes values in the interval $[-1, 1]$. Spheres of radius 6 Å were centred on two key residues on S4 and S6 helices and on SF of the neighbouring subunit to identify all residues inside them for at least 75% of the trajectory defining the source and sink regions. Shortest paths were computed using the Dijkstra's algorithm [51]. The betweenness of each residue was computed with Brandes algorithm [23] as implemented in the NetworkX library [76].

2.3 Computational protocol for hERG channel

2.3.1 Production of the open and the closed states

hERG open state was produced from the experimentally solved structure (PDB ID: 5VA2) [195] and the missing loops were modelled using MODELLER [56]. For the closed state, a homology model was initially produced using as a template the EAG1 closed channel (PDB ID: 5K7L) [199] featuring ca. 75% sequence identity. However, the resulting structure was functionally closed but with the VSD in the open configuration. In order to pull the VSD to the close configuration, Steered MD simulations [84] were run in the NVT ensemble for 2 ns applying a helix-axis-orthogonal force on the centre of mass of C_α atoms of each S4 to move it towards S6 of the same subunit to prevent steric clashes; then a force parallel to the axis was applied for 4 ns to the centre of mass of helix S4 to move it down. The pulling velocity was 3 Å/ns and the spring constant of the virtual spring between the dummy atom and the SMD atom was 10 kcal/mol/Å^2. S1, S2, S3, and S5 were fixed and a helical restraint on S4 was applied with a force constant of 1000 kcal/mol/Å^2. Using the CHARMM membrane builder [90, 201], all systems were embedded in bilayers of 337 1-palmitoyl-2-oleoyl-sn-glycero-3-phosphocholine lipids with 49,468 TIP3P water molecules and 0.15 M of KCl to form a simulation box of ca. $125 \times 125 \times 150$ Å totalling $223,584$ atoms. The WHAT-IF server [192] was used to analyse the protonation states of residues. All aspartates and glutamates were ionized. H5, H342, H374, H434 and H437 were predicted to be in the δ protonation state; H88, H95, H165, H181, H190, H277, H290, H306, H334, H365 and H454 were assigned to the ϵ protonation state.

2.3.2 MD simulations

The production run was carried out in the NPT ensemble for 100 ns. All simulations were run with NAMD [153] using the AMBER ff14SB force field for the protein [125], the Lipid17 force field for the lipids [50] and TIP3P water model [127]. Simulations for the tentative production of the inactivated state were run for 150 ns using the CHARMM force field PARAM36 for proteins [121, 122, 18], lipids [100] and ions [15]. Explicit water was described with the TIP3P water model [127]. Pressure was kept at 1.01325 Bar by the Nosé-Hoover Langevin piston method [128, 58] and the temperature was maintained at 303.15 K by a Langevin thermostat with damping coefficient of 1 ps^{-1}. Long-range electrostatic interactions were evaluated with the smooth Particle Mesh Ewald algorithm with a grid space of 1 Å. For short-range

non-bonded interactions, a cut-off of 12 Å with a switching function at 10.0 Å was used. The integration time-step was 2 fs.

2.4 The transition path of the activation mechanism

A first guess of the transition path from the closed to the open state was obtained *via* RMSD-biased Targeted Molecular Dynamics (TMD) [168]. At first, we run TMD simulations for 1 ns in the NPT ensemble using a force constant of 100,000 kcal/mol/Å^2 on C_α atoms. Then, we repeated the simulations for 25 ns in the NPT ensemble using the same force constant. In both cases, the transition paths observed were the same and the analyses described in the next sections produced similar results.

The limitations of the time-step make it impossible to reach biologically relevant timescales of the order of the milliseconds and above using standard molecular dynamics techniques. This problem led to the development of biased MD techniques where the force field is supplemented with a biasing potential that lowers energy barriers accelerating biochemical transitions. One such technique is Targeted Molecular Dynamics, a biasing technique that applies a harmonic bias on the RMSD distance from the current to the target conformation.

$$U_{TMD} = \frac{1}{2}\frac{k}{N}[RMSD(t) - \rho(t)]^2 \tag{2.24}$$

In this protocol the target $RMSD$ distance, ρ, decreases linearly and k is the force constant acting on the N atoms of the system. At each new value of ρ the system jumps on a hypersphere closer to the target where it can diffuse freely (Figure 2.1).

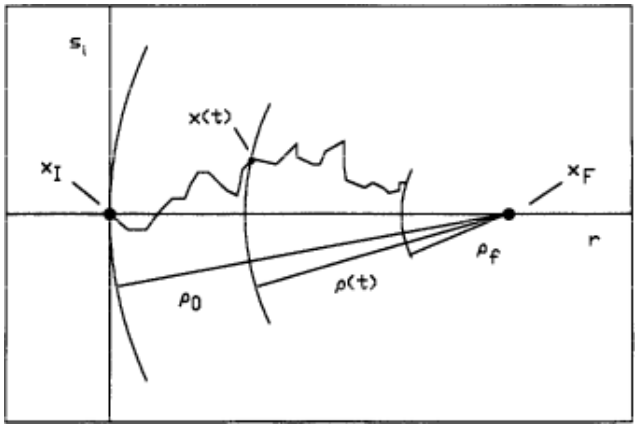

Figure 2.1. Schematic representation of the TMD algorithm. The simulation starts at initial conformation x_I and at each new value of the center of the harmonic restraint $\rho(t)$, the system jumps on a hypersphere closer to the target conformation x_F [168].

The following analyses were carried out on the TMD trajectories.

2.4.1 Contact maps

The contact map was computed for each frame of the TMD simulation, considering two residues to be in contact when a pair of heavy atoms of the side-chains was

closer than 5.0 Å.

2.4.2 Pseudo Potential of Mean Force

Two-dimensional pseudo-PMFs were computed as a function of the geometric observables monitored during the transition: sliding and rotation of the S4 helices; bending of the S6 helices; rotation of cytosolic domains (CTD) with respect to transmembrane ones (PD). Although it has been shown that PMF can be estimated from out equilibrium trajectories using the Jarzynski equality [184], it is very difficult to reach the convergence of the forces in simulations of few nanoseconds as in the case of our 25 ns TMD simulations. For this reason, we used the term "pseudo" referring to the fact that the PMF were computed during non-equilibrium trajectories where the convergence was not reached. They are defined as:

$$\mathrm{PMF(x,y)} = -\mathrm{k_B T} \log \mathrm{H(x,y)} \tag{2.25}$$

Where k_B is the Boltzmann constant, T is the temperature set at 300.0 K and $H(x, y)$ is a normalised two-dimensional histogram of the two observables x and y. The histograms and pseudo-PMFs calculated for each system were: S4 Rotation Angle vs S4 Displacement; S6 Bending Angle vs S4 Displacement; S6 Bending Angle vs S4 Rotation Angle; PD-CTD Rotation Angle vs S4 Displacement; PD-CTD Rotation Angle vs S4 Rotation Angle; PD-CTD Rotation Angle vs S6 Bending Angle.

The bending angle θ of each helix S6 was computed as:

$$\theta = \arccos \frac{\overrightarrow{v_{CT}} \overrightarrow{v_{CB}}}{|\overrightarrow{v_{CT}}||\overrightarrow{v_{CB}}|} \tag{2.26}$$

where $\overrightarrow{v_{CT}}$ is a vector pointing from the middle region of helix S6 (residues 646-650) to the top of the same helix (residues 635-639). Similarly, $\overrightarrow{v_{CB}}$ is a vector pointing from the middle to the bottom end (residues 663-667) of helix S6.

The visual inspection of the open structure of hERG channel reveals that the transmembrane domains (VSD+PD) of non-neighbouring subunits (1-3 and 2-4) are roughly orthogonal to the corresponding cytosolic domains. During the simulations the rotation angles, ϕ_{13} and ϕ_{24}, depart from this value and evolve as a function of time. They are defined by the following vectors: $\overrightarrow{v^{ij}_{TMD}}$: vector connecting the center of mass of the trans-membrane domains (PD+VSD) of chain i with the center of mass of the trans-membrane domains of non-neighbouring chain j. $\overrightarrow{v^{ij}_{CD}}$: vector connecting the center of mass of the cytosolic domain (C-Linker + CTD) of chain i with the center of mass of the cytosolic domain of non-neighbouring subunit j. Angles ϕ_{13} and ϕ_{24} are then computed as:

$$\phi_{13} = \arccos \frac{\overrightarrow{v^{13}_{TMD}} \overrightarrow{v^{13}_{CD}}}{|\overrightarrow{v^{13}_{TMD}}||\overrightarrow{v^{13}_{CD}}|} \tag{2.27}$$

$$\phi_{24} = \arccos \frac{\overrightarrow{v^{24}_{TMD}} \overrightarrow{v^{24}_{CD}}}{|\overrightarrow{v^{24}_{TMD}}||\overrightarrow{v^{24}_{CD}}|} \tag{2.28}$$

The rotation of helix S4 around its axis was computed as follows. In a perfect helical geometry, the vector connecting the center of mass of C_α atoms n and $n+4$ with the C_α atom $n+2$ is orthogonal to the helix axis. The angle α between this vector $\overrightarrow{v^{rot}}(t)$ and its counterpart $\overrightarrow{v^{rot}}(0)$ in the initial conformation defines the rotation angle. To account for local deformations of the helical geometry that might undermine the orthogonality of $\overrightarrow{v^{rot}}$ to the axis, the calculation was performed using the component of $\overrightarrow{v^{rot}}$ orthogonal to the axis:

$$\alpha = \arccos \frac{\overrightarrow{v_\perp^{rot}}(\mathrm{t})\overrightarrow{v_\perp^{rot}}(0)}{|\overrightarrow{v_\perp^{rot}}(\mathrm{t})||\overrightarrow{v_\perp^{rot}}(0)|} \tag{2.29}$$

Defining $\overrightarrow{r_{COM}}(t)$ as the vector corresponding to the center of mass of helix S4, the displacement of S4 along its axis is:

$$\mathrm{d} = [\overrightarrow{r_{COM}}(\mathrm{t}) - \overrightarrow{r_{COM}}(0)]\hat{\mathrm{h}} \tag{2.30}$$

where $\hat{h}$ is the versor aligned along S4 axis.

The displacement and rotation angle of the S4 helices and the bending angle of the S6 helices were the average over the four subunits. For the rotation angle of S4 helices, the average of the rotation angles over the four subunits were computed in the middle and at the bottom of individual S4 helices. Finally, the PD-CTD rotation angle was computed as the average of $\phi_{13}(t)$ and $\phi_{24}(t)$.

2.5 Network analysis

The path communication analysis was carried out representing the protein as a graph [21] where nodes are protein residues and edges interactions between pairs. Two metrics have been used to assign weights to graph edges.

Initially, in the same vein of [60] edge weights were calculated using: $\mathrm{d_{ij}} = -\log|\mathrm{Corr_{ij}}|$. $\mathrm{Corr_{ij}}$ is the correlation coefficient, *i.e.* the normalized covariance of C_α positions:

$$\mathrm{Corr_{ij}} = \frac{\langle(\vec{r}_i - \langle\vec{r}_i\rangle)(\vec{r}_j - \langle\vec{r}_j\rangle)\rangle}{\sqrt{\langle(\vec{r}_i - \langle\vec{r}_i\rangle)^2\rangle\langle(\vec{r}_j - \langle\vec{r}_j\rangle)^2\rangle}} \tag{2.31}$$

where $\vec{r}_i$ and $\vec{r}_j$ are the position vectors of the i and j residues and $-1 \leq \mathrm{Corr_{ij}} \leq 1$. In building the graph two residues are considered linked by an edge only if their communication distance d_{ij} is below a cutoff d_{cut} =0.40. This means that only pairs of residues with an absolute value of the correlation coefficient greater than 0.67 are connected by an arc (see Appendix).

Then, we repeated the network analysis using a more accurate [198] weight expressed as: $\mathrm{w_{ij}} = -\log(\mathrm{C_{ij}}M_{\mathrm{ij}})$ where C_{ij} is a semi-binary contact map and M_{ij} is a matrix that quantifies the motion correlation using the Mutual Information. Here, C_{ij} is a semi-binary contact map that was computed with a truncated Gaussian kernel (Figure 2.2):

$$K(d_{ij}) = \begin{cases} 1, & d_{ij} \leq c \\ e^{-\frac{(d_{ij}^2 - c^2)}{2\sigma^2}}, & d_{ij} > c \end{cases} \tag{2.32}$$

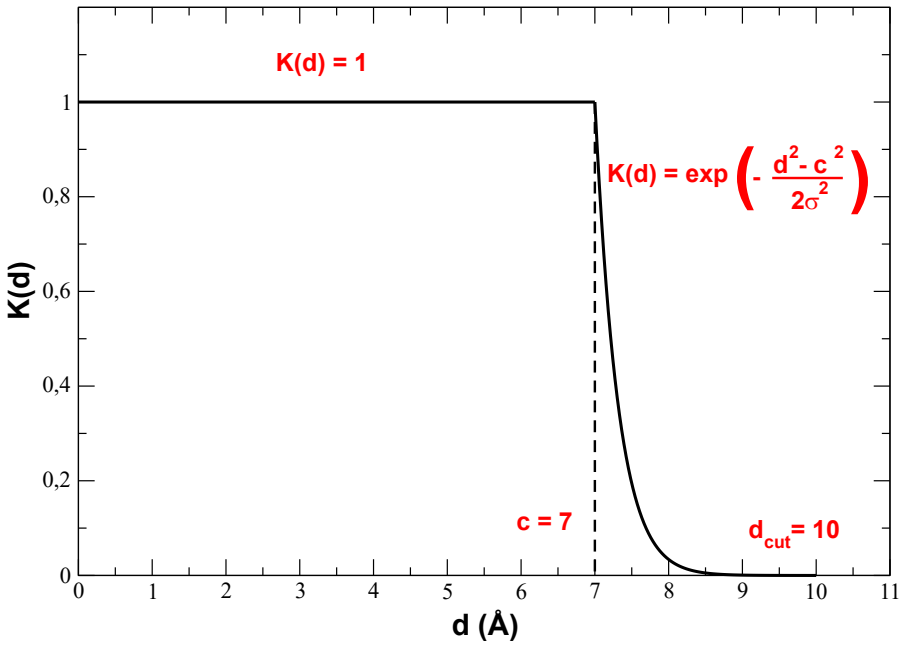

Figure 2.2. The Gaussian kernel used in the definition of semi-binary contact maps.

where d_{ij} is a distance between the C_α of i and j residues and c is the cut-off distance set to 7.0 Å. The width σ of the Gaussian kernel was chosen so as to attain a negligibly small value of the kernel at $d_{ij} = 10$ Å. Specifically, we used $K(d_{cut}) = 10^{-5}$ and $\sigma = 1.48$. The contact map is computed by averaging the value of the kernel over all the frames of the trajectory:

$$C_{ij} = \frac{1}{N_{frames}} \sum_{n=1}^{N_{frames}} K(d_{ij}(n)) \tag{2.33}$$

The mutual information M_{ij} of two random variables is a measure of their reciprocal independence or coupling and was used to quantify the motion correlation of two residues. Defining d_i and d_j as the displacement of the center of mass of the side-chain with respect to its average position, the mutual information is:

$$M_{ij} = \sum_{d_i} \sum_{d_j} P(d_i, d_j) log \frac{P(d_i, d_j)}{P(d_i)P(d_j)} \tag{2.34}$$

In this work, a normalized mutual information was used as the information quality ratio $M'_{ij} = \frac{M_{ij}}{H_{ij}}$ where H_{ij} represents the Shannon entropy [103] of the variables d_i and d_j.

As shown in Figure 2.3, in both analyses, spheres of radius 7 Å were centred on two key residues on helix S4 or loop S4-S5 and on S6 of the same or $n+1$ subunit to

identify all residues inside them for at least 70% of the trajectory defining the source and sink regions. Shortest paths were computed using the Dijkstra's algorithm [51].

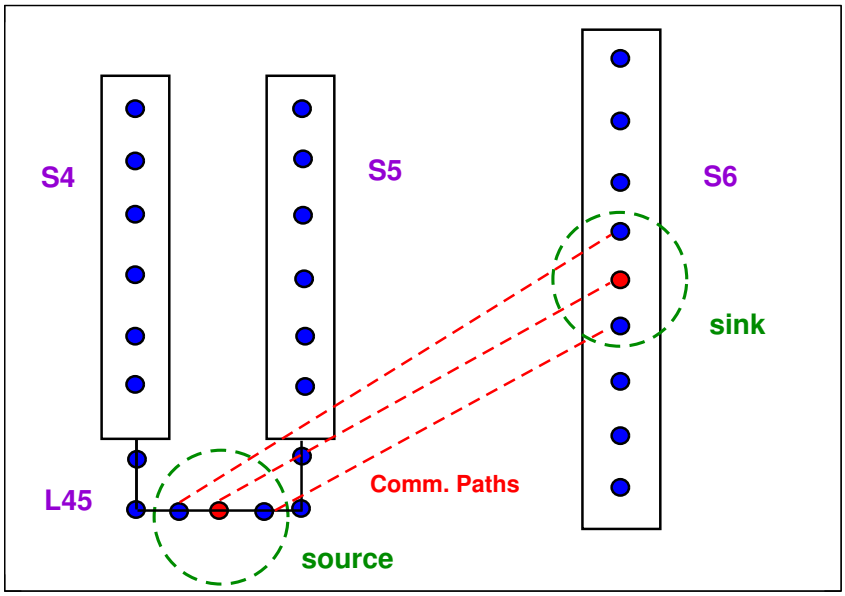

Figure 2.3. Schematic representation of the application of Dijkstra's algorithm to the calculation of VSD-PD communication paths in hERG channel.

The Centrality Index (CI) was computed as the fraction of minimal paths a residue sits on. The betweenness centrality (B) of each residue was computed with Brandes algorithm [23] as implemented in the NetworkX library [76]:

$$B(v) = \sum_{s \neq v \neq t} \frac{\sigma_{st}(v)}{\sigma_{st}} \tag{2.35}$$

where v is a node, σ_{st} is the number of minimal paths that connect nodes s to t, and $\sigma_{st}(v)$ is the number of minimal paths that passing through the node v connect nodes s to t.

2.6 Statistics and reproducibility

The variability of the network weights d_{ij} and w_{ij} was determined using a block analysis [64, 85]. The simulations were split into N_B subtrajectories of 25 ns, long enough to consider the weights computed in the different blocks as uncorrelated measurements. The standard deviation for each element of the matrices was computed as:

$$\sigma(x_{ij}) = \sqrt{\frac{1}{N_B(N_B-1)} \sum_{B=1}^{N_B} (x_{ij}^B - \bar{x_{ij}^B})^2} \tag{2.36}$$

where x_{ij}^B is the value of the weights (d_{ij} and w_{ij}) computed in block B while $\bar{x_{ij}^B}$ is the average over all blocks.

Chapter 3

Results

3.1 Inactivation paths in K_v1.2 channel

Using the network-theoretical approach, we identified two different families of paths for the motion propagation (Figure 3.1) joining the VSD and SF and the PD and the SF, respectively. Since these paths reached the SF excluding the L45 known to be involved in the activation/deactivation of the channel [12], it can be hypothesized that they are both involved in the channel inactivation. In the first case, the motion from the top of helix S4 went down and jumped onto helix S5 of the neighbouring subunit at the level of the residues V301 and S344; at the same time, from the bottom of helix S4 it went up and passed to helix S5 of the neighbouring subunit with I304 and L341. Then, through the P-Loop it reached the SF (red arrows in Figure 3.1a) where the motion of Y377 could affect the dynamics of its counterpart Y377 on the SF of the subunit where the path was originated. The VSD-SF path length averaged for the four subunits was ca. 1. This value is expressed by the sum of the arc lengths (weights) d_{ij} that are traversed along a path of minimal length connecting residues i and j. Arc weights are computed according to equation $d_{\mathrm{ij}} = -\log|\mathrm{Corr}_{\mathrm{ij}}|$ where Corr_{ij} is the correlation coefficient that measured how efficiently the information was transferred from one residue to the other (see *Methods*). Considering the logarithmic nature of this metric, the length value is a pure number which is zero only for perfect correlation. Values in the range $0 < d_{ij} < 2$ typically mean that there is a high correlation of the motion of each pair of residues on the path. In the same way, we saw a direct connection between the inner and the outer pore gates (PD-SF coupling) involving the residues I402 and T373 of the same subunit with an average path length of ca. 1.10. (blue arrows in Figure 3.1a).

The centrality index (CI) and the betweenness (B) of each residue implicated in the paths are shown in Table 3.1: high values correspond to residues that act as hubs in the communication paths and thus are expected to play a key role in the motion propagation.

The microscopic characterization of the inactivation paths was done computing a contact map that highlighted all the conserved interactions formed between residues of the same or the neighbouring subunits. Figure 3.2 represents the contact map of the whole protein and of a single subunit where black dots are the formed interactions between residues for at least 75% of the equilibrium trajectory. The contact pattern

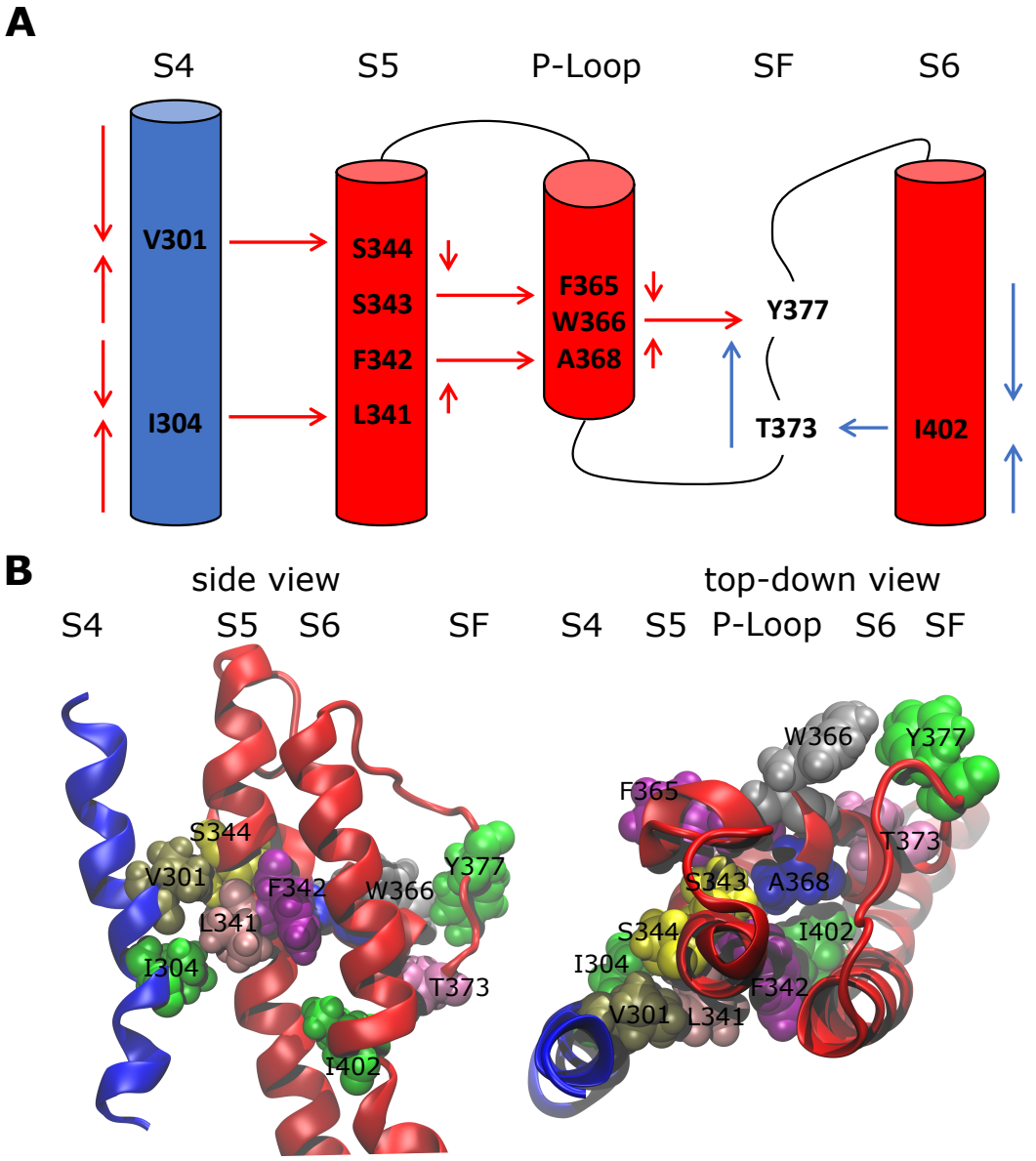

Figure 3.1. Inactivation paths of the wild type $K_v1.2$ channel. **(A)** Arrows describe the preferred routes of motion propagation: red arrows refer to S4→S5→P-Loop→SF route; blue arrows refer to the S6→SF route. **(B)** Side and top-down views of residues implicated in the paths at the interfaces S4\S5, S5\P-Loop, P-Loop\SF and S6\SF.

shown in the whole protein map confirmed the presence of interactions between helices S4 and helices S5 of the neighbouring subunit (red box in Figure 3.2a). Besides, the contacts formed between helices S5 and the P-Loop and helices S6 and the SF of the same subunit (blue box in Figure 3.2b) supported the second part of the paths that we identified in Figure 3.1a.

3.1.1 Inactivation paths in $K_v1.2$ mutants

The network approach allowed to identify two routes of the motion propagation as the molecular bases of a VSD-SF and PD-SF coupling mechanisms. The residues that connect the interfaces S4\S5, S5\P-Loop, P-Loop\SF, and S6\SF are strongly coupled in the equilibrium dynamics of the open state. Many of them have been already demonstrated to influence the Shaker or $K_v1.2$ inactivation if mutated including L361R, L366H and W366F [203, 146, 44, 42, 13] but a microscopic interpretation of the effects of the mutation is still elusive. Moreover, it was hypothesized that the VSD-SF coupling depends on the volume of the residues that lay along the inactivation path [13]. For this reason, in order to describe the microscopic role of each residue implicated in the paths, we applied the same network-theoretical approach to mutated channels and then we computed a contact map to identify the effects of the mutations on the contact formation. In some cases, we reproduced computationally experimental mutants whose effect on the inactivation was already characterized in Shaker channels, e.g. L361R, L366H, W434F. In order to further characterize the role of key residues lying along the paths coupling the VSD and the PD to the SF and for which an experiment was not available, we produced a computational model of $K_v1.2$ with non-conservative mutations obtained by replacing individual residues by an alanine. All the path lengths of $K_v1.2$ mutants are shown in Table 3.2.

At first we focused on the VSD-SF coupling path, starting from residues of the voltage sensor helix S4: L293R, L298H, V301A, I304A. In all cases the coupling paths for the inactivation were qualitatively similar to the wild type but with a different path length. The greatest effects were observed mutating L293 on the top of S4 helix, with the average path length reaching values of ca. 10 in the L293R mutant. It probably depended on the introduction of a new positively charged amino acid that influenced the sensitivity to the membrane potential variation. Considering the logarithmic nature of this metric, a difference of two units in the path length corresponds to a difference of one order of magnitude in terms of correlation, meaning that the path is effectively hindered in the mutant. These results are in agreement with the experiments on Shaker where L361R channels activated and inactivated at much more hyperpolarized membrane potentials, implying that the inactivation was not preserved [203].

In the L298H channel the VSD-SF coupling was extremely weak. The contact map analysis revealed the formation of new contacts between helix S4 and helices S1 and S2 (Figure 3.3). More precisely, in the mutant, the new histidine maintained the hydrophobic interaction with F348 on helix S5 but its larger steric clash induced a displacement of helix S4 by 3 Å towards helices S1 and S2. We hypothesize that the rearrangements of helix S4 is at the origin of the modification of the inactivation paths. These computational evidences seem to be in agreement with the experimental Shaker double mutant L366H:W434F where the currents show a decay under sustained voltage-clamp depolarization reminiscent of C-type inactivation, suggesting this process has not been eliminated but rather mitigated. Indeed, L366H relieves the W434F effect of the inactivation increased speed, converting a non-conductive channel in a conductive one [13].

In the I304A channel the efficiency of the information transfer from VSD to SF became weaker than the wild type. The missing hydrophobic interaction between

A304 and L341 on helix S5 is probably the main cause of the loss of inactivation. Interestingly, we identified a new route that from helix S4 reached helix S5 jumping onto helix S1 of the same subunit at the level of R300-F180 contact but this path had a length greater of ca. 3 (see Table 3.2). Consequently, in I304A channel the inactivation seems to be delayed or completely abolished.

For both V301A and S344A mutants we saw a path qualitatively and quantitatively (length ca. 1) similar to the wild type, meaning that the inactivation would not be affected by the alanine substitutions. Indeed, the contact map analysis revealed that the hydrophobic interactions at the S4\S5 interface were preserved. These results agree with the thesis that the VSD-SF coupling depends on the volume of the residues involved in the inactivation path [13].

Residue F342 on helix S5 plays a central role in the inactivation path connecting the VSD to the SF. Indeed, it is characterized by a very high centrality index. To further dissect its role in this path, we introduced an alanine substitution in each subunit. The mutated channel F342A had a loss of this coupling mechanism. Interestingly, we saw that the F342-A368 interaction was completely broken by the alanine replacement probably due to the the smaller size of the hydrophobic region of the residue.

On the other hand, in the W366F channel we identified the same VSD-SF path as in the wild type but with a lower average length of ca. 0.60. Here, the efficiency of the information transfer was greater than the wild type suggesting the presence of an enhanced and faster inactivation in agreement with the experimental results on $K_v1.2$ channel [42] and on the corresponding W434F of Shaker [146]. However, the contact map analysis did not reveal new broken or formed interactions.

Finally, we focused on the PD-SF coupling mechanism where we performed the mutations T373A and I402A. In both mutants there was an increase of the path length meaning that the information transfer was generally less efficient than in the wild type. No interactions were detected between these residues in the contact map analysis, which suggests that the PD-SF coupling breaks. These results are supported by Cuello and coworkers where strong van der Waals interactions were observed between these residues in the pore-helix of the same subunit [44].

It is noteworthy that the mutation of a residue implicated in one of the two paths that defined the VSD-SF or the PD-SF couplings did not influence the other mechanism. However, the experimental studies showed that mutating a residue along one of the two paths [203, 146, 44, 42, 13] determined the disruption only of that path which is sufficient to impair inactivation. This evidence suggests that the two communication paths are not inter-changeable and both play a role in the C-type inactivation mechanism.

Residue	Centrality Index (CI)	Betweenness
L293	$0.10 \leq CI \leq 0.15$	Low
R294	$0.10 \leq CI \leq 0.15$	Low
V295	$0.10 \leq CI \leq 0.20$	Low
I296	$0.20 \leq CI \leq 0.25$	Low
R297	$0.30 \leq CI \leq 0.35$	Low
L298	$0.30 \leq CI \leq 0.45$	Medium
V299	$0.40 \leq CI \leq 0.55$	Medium
R300	$0.50 \leq CI \leq 0.60$	Medium
V301	$0.70 \leq CI \leq 0.80$	High
F302	$0.70 \leq CI \leq 0.80$	High
R303	$0.70 \leq CI \leq 0.80$	High
I304	$0.80 \leq CI \leq 0.90$	High
F305	$0.70 \leq CI \leq 0.85$	Medium
K306	$0.70 \leq CI \leq 0.80$	Medium
L307	$0.60 \leq CI \leq 0.70$	Medium
S308	$0.40 \leq CI \leq 0.55$	Medium
R309	$0.40 \leq CI \leq 0.55$	Medium
H310	$0.10 \leq CI \leq 0.20$	Low
S311	$0.10 \leq CI \leq 0.20$	Low
L341	$CI \geq 0.90$	High
F342	$CI \geq 0.90$	High
S343	$CI \geq 0.90$	Medium
S344	$0.50 \leq CI \leq 0.70$	Medium
F365	$0.75 \leq CI \leq 0.85$	High
W366	$CI \geq 0.95$	High
W367	$0.90 \leq CI \leq 0.95$	High
A368	$CI \geq 0.95$	High
T373	$CI \geq 0.95$	High
T374	$0.90 \leq CI \leq 0.95$	High
V375	$CI \geq 0.95$	High
G376	$0.80 \leq CI \leq 0.90$	Medium
Y377	$CI \geq 0.95$	High
C394	$0.10 \leq CI \leq 0.15$	Low
A395	$0.10 \leq CI \leq 0.20$	Low
I396	$0.20 \leq CI \leq 0.25$	Low
A397	$0.20 \leq CI \leq 0.30$	Medium
G398	$0.30 \leq CI \leq 0.45$	Medium
V399	$0.50 \leq CI \leq 0.60$	Medium
L400	$0.70 \leq CI \leq 0.85$	Medium
T401	$0.80 \leq CI \leq 0.90$	High
I402	$CI \geq 0.95$	High
A403	$0.80 \leq CI \leq 0.90$	High
L404	$0.70 \leq CI \leq 0.80$	Medium
P405	$0.40 \leq CI \leq 0.50$	Medium
V406	$0.20 \leq CI \leq 0.40$	Medium
P407	$0.20 \leq CI \leq 0.35$	Medium
V408	$0.10 \leq CI \leq 0.20$	Low
I409	$0.10 \leq CI \leq 0.20$	Low
V410	$0.10 \leq CI \leq 0.20$	Low

Table 3.1. Centrality Index (CI) and betweenness of each residue implicated in the paths. Legend Betweenneess (B): low $0 < B \leq 1$; medium: $1 < B \leq 4$; high: $4 < B \leq B_{max}$. Residues whose mutations are implied in epileptic encephalopathy are shown in bold.

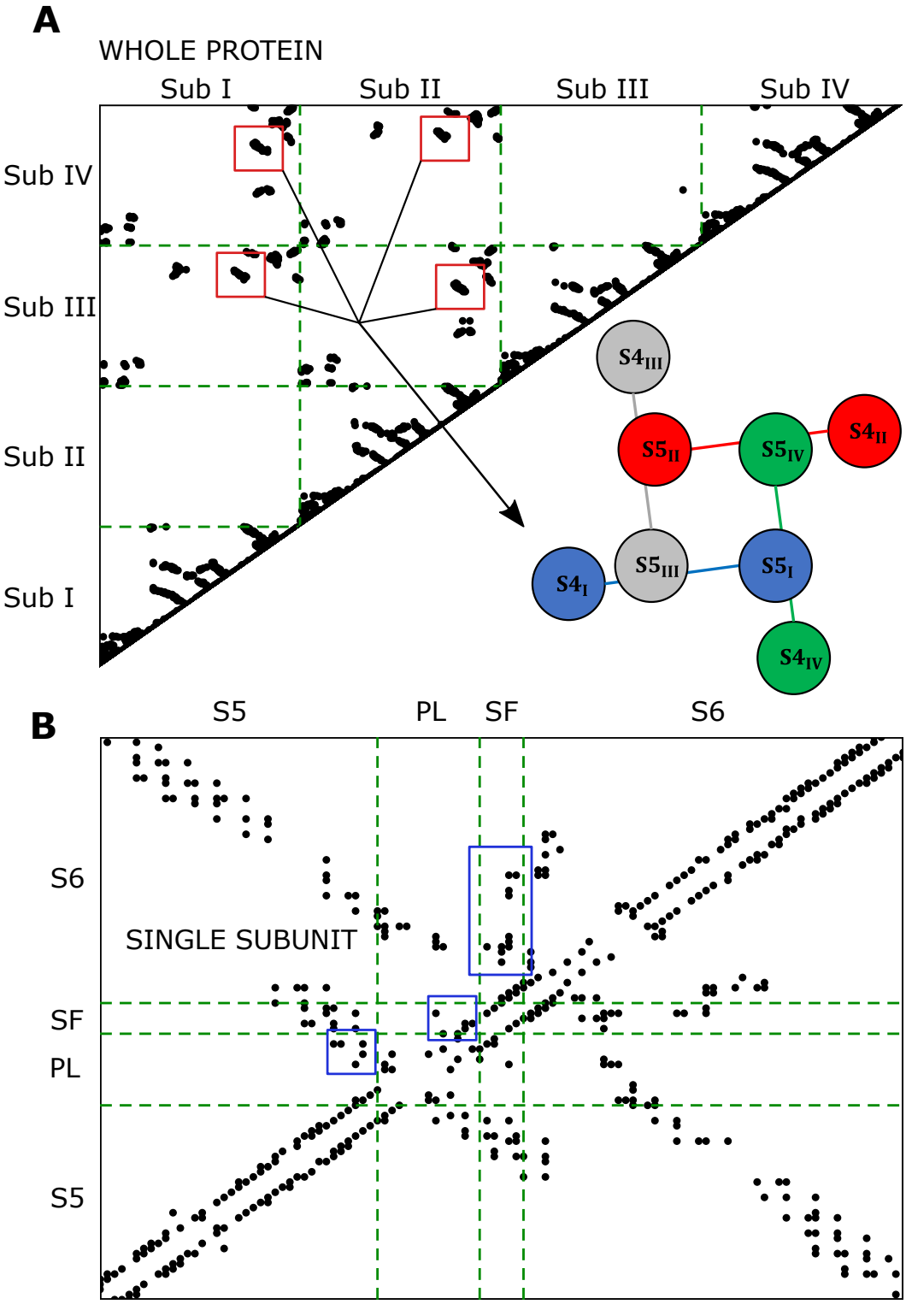

Figure 3.2. Contact maps of the whole protein **(a)** and a single subunit **(b)**. Black dots represent the formed interactions. In the single subunit map the black dots are the formed interactions persisting in at least 75% of the trajectory in 3/4 subunits.

Mutation	VSD-SF path length	PD-SF path length
WT	0.97	1.12
L293R	9.79	2.78
L298H	5.44	1.36
V301A	1.72	1.31
I304A	3.01	1.50
F342A	5.61	1.49
S344A	1.58	1.37
W366F	0.62	1.71
T373A	1.06	2.32
I402A	1.37	4.77

Table 3.2. Comparison of the average paths length for the $K_v1.2$ WT and the mutants.

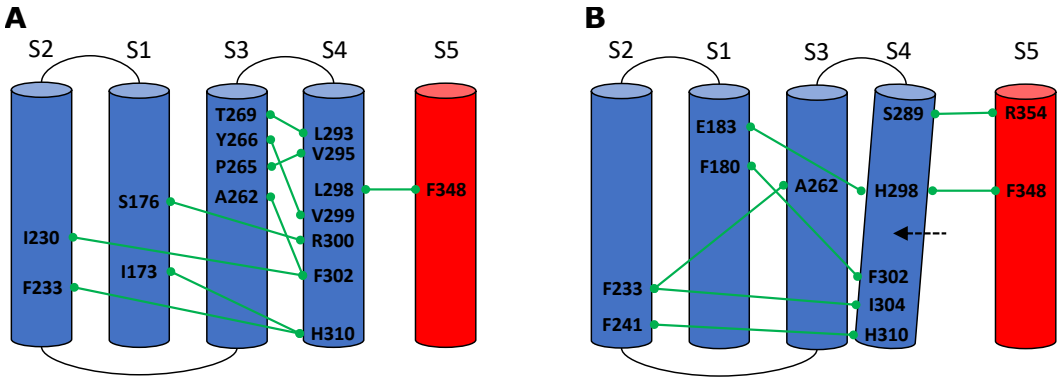

Figure 3.3. Conserved interactions formed between helix S4 and S1, S2, S3 and S5 helices of the same or neighbouring subunits in the wild type **(a)** and in the mutated L298H channel **(b)**.

3.2 Structure of hERG closed state

The open state of hERG was produced from the experimentally solved structure (PDB ID: 5VA2) [195] and the missing loops were modelled by MODELLER [56]. In the structure of the open state a very long fragment (residues 132-397) connecting the PAS domain with the VSD was not experimentally resolved. Since this fragment was too long to be reliably modelled using state of the art bioinformatic tools, the whole N-terminal region (residues 1-397) was not included. The structure studied in this work therefore approximately corresponds to the hERG1b isoform [145, 110, 176] which lacks the entire PAS/Pas-cap domains (it is 340 residues shorter than hERG1a). The hERG1b isoform was recently found to be critical for human cardiac repolarization as testified by a hERG1b-specific mutation associated with intrauterine fetal death [93, 92]. For the closed state no experimental structure was available. A homology model was initially produced using as a template the EAG1 closed channel (PDB ID: 5K7L) [199] but the resulting system inherited from the template a VSD in the open configuration. More in detail, the open or closed conformation of helix S4 depends on its relative position with respect to a critical phenylalanine (F463) on helix S2 that acts as the gating charge transfer centre (GCTC). In the open conformation only two of the five positively charged residues of helix S4 are below the critical F463 ring. It is not clear how many basic residues must be below the critical F463 in the closed state. Using the limiting slope method the gating charge of hERG channel was experimentally estimated to be ∼6.4e [207]. The fact that the technique relies on the ability to measure open probabilities close to zero, however, introduces a strong uncertainty on the experimental measurements that must be considered as a lower bound of the true value. Assuming a 20% underestimation, Zhang et al suggested a corrected value of 8.0e. The variability of the experimental estimates of the gating charge suggests the opportunity to simulate molecular systems with different displacements of helix S4. In particular, in the spirit of Ref. [10], each VSD in the closed state was moved down *via* Steered Molecular Dynamics simulations [84] producing three isoforms of the closed state with different Q_g values: $4e$ with the four S4 helices displaced downwards by a single basic residue, $8e$ with all S4 helices displaced downwards by two basic residues, and $6e$ with S4 helices of subunit I and III displaced by one residue and the remaining ones by two residues (Figure 3.4). During the SMD simulation helices S1, S2, and S3 were kept fixed because no experimental evidence exists of their motion during the dynamics of the VSD [114].

Stability of the closed structures

At first, the stability of the closed state models was assessed through analysis of the Root Mean Square Deviation (RMSD). After a modest increase following the SMD run, RMSD remains roughly constant during the 100 ns of the production run (Figure 3.5).

Then, we focused on interactions that are experimentally known to characterize the closed state of the channel: D411-K538 [206], D456-K525 [206]; E544-R665 [163, 126]. The different patterns of charge pairings enable the discrimination of closed and open states. Indeed, these studies date back to the period when no experimental

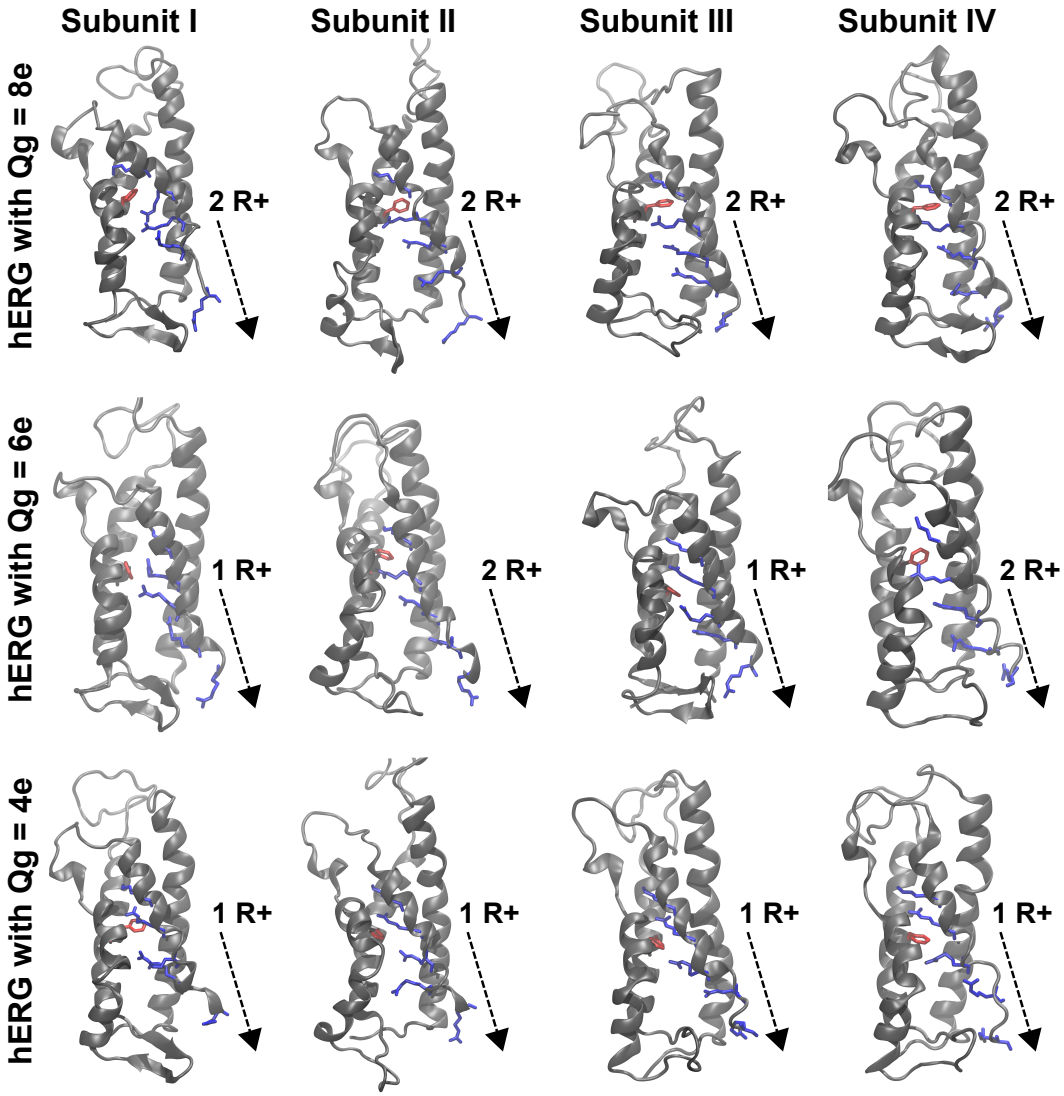

Figure 3.4. S4 configuration in closed states after Steered MD simulations. The positive charged residues (R+) on helix S4 (K525, R528, R531, R534 and R537) are coloured in blue while the F463 on helix S2 that acts as the gating charge transfer centre is coloured in red. Arrows refer to the number of positive charge residues (R+) displaced from the from the open configuration to produce the closed systems.

structure of hERG was available and specific salt bridges provided spatial constraints for homology modelling. In particular, charge reversal mutagenesis experiments by Zhang et al [206] revealed that the K525D and K538D mutations significantly accelerated hERG activation suggesting these lysines could be involved in salt bridges stabilizing the closed state. This hypothesis was confirmed by a mutant cycle analysis showing that D411 (which is peculiar of the EAG family) at the inner end of S1 interacts with K538 at the inner end of S4, while D456 (conserved among K_v channels) at the outer end of S2 interacts with K525 at the outer end of S4. Interactions between charged residues in the trans-membrane segments of hERG may be important for the known slow activation rate of this channel. In fact, it

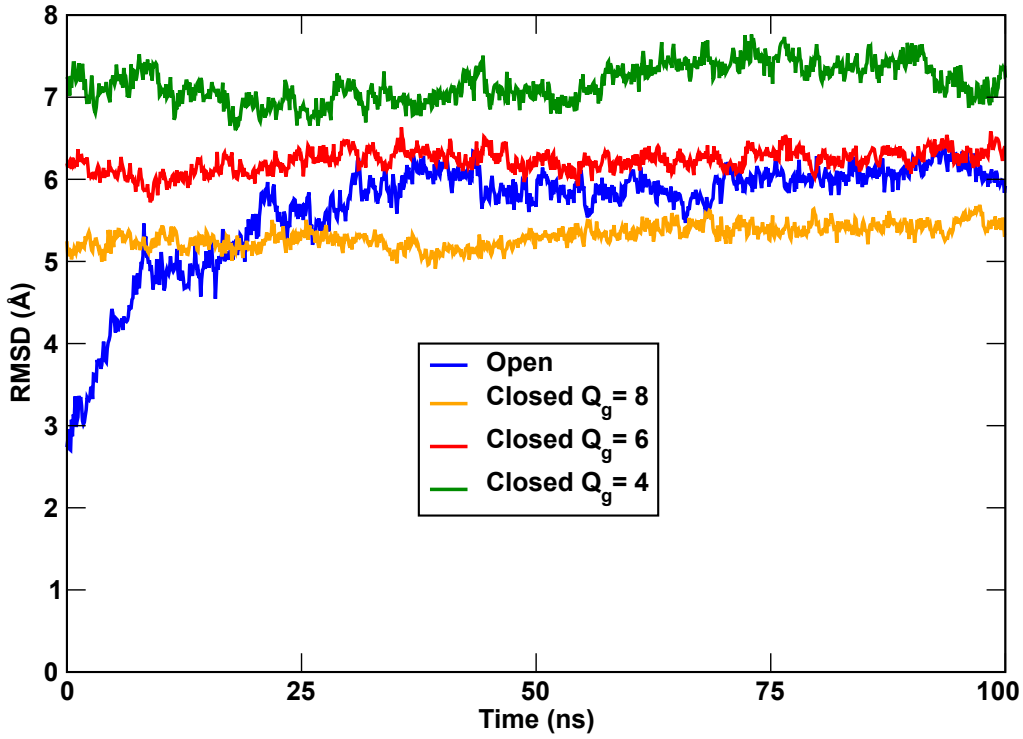

Figure 3.5. The root-mean-square deviation (RMSD) during the 100 ns equilibrium simulations after the Steered MD simulations. The RMSD plot of the open state was computed using as a reference conformation the experimental structure of hERG (PDB ID: 5VA2). For the RMSD profiles of closed states we used as reference structure, the homology model generated from the template EAG1 (PDB ID: 5K7L). The superposition of the current and reference conformations was performed using all backbone atoms.

can be speculated that the strong salt bridges stabilizing the closed state might be the cause of the slow movement of S4 [155] during membrane depolarization. As shown in Figure 3.6 and in Table 3.3, in all of the hERG closed states we generated, using a distance cutoff of 5.0 Å between the ϵ-Nitrogen of the lysines and the δ-Oxygen of the aspartates, we could identify both salt bridge D456-K525 and D411-K538. Another group of contacts stabilizing hERG closed states are those between the S4-S5 loop and the C-terminal end of helix S6. In particular, Sanguinetti and coworkers [163] showed that the D540K mutation endowed the hERG channel with the ability to open in response to membrane hyperpolarization. This unusual behaviour was shown to stem from the breakdown of the D540-R665 salt bridge and the electrostatic repulsion between the lysine placed in position 540 and R665. Another critical residue located on the S4-S5 loop is E544. While the mutation to lysine of this residue does not cause hyperpolarization-induced channel re-opening [163], the E544L mutation significantly enhances the pharmacologic response to hERG activator NS1643 (see [74] and references therein). Based on this evidence, Guo et al designed a set of powerful hERG activators with binding pocket in the neighborhood of D544. The efficacy of these drugs suggests that they prevent the formation of a critical salt bridge between E544 and a basic residue on helix S6.

This mechanism is also supported by the observation [126] that covalently binding, through a disulfide bridge, a peptide mimicking the S4-S5 linker to the channel S6 C-terminus completely inhibits hERG. It is notable that in these experiments the disulfide bond was introduced between E544C and L666C, suggesting that in physiologic conditions a salt bridge is established between E544 and R665. Indeed, as illustrated in Figure 3.6 and in Table 3.3, salt bridge E544-R665 could be observed in all of our hERG closed states. These results show that all the three isoforms produced are good template for hERG in the closed state.

		D456-K525	D411-K538	E544-R665
$Q_g = 8$	Subunit I	6.16 Å	6.95 Å	3.99 Å
	Subunit II	4.91 Å	6.01 Å	3.61 Å
	Subunit III	4.82 Å	6.22 Å	4.26 Å
	Subunit IV	4.65 Å	5.38 Å	4.02 Å
$Q_g = 6$	Subunit I	3.77 Å	4.48 Å	4.21 Å
	Subunit II	5.35 Å	6.89 Å	3.61 Å
	Subunit III	4.52 Å	4.69 Å	4.69 Å
	Subunit IV	4.77 Å	6.29 Å	4.57 Å
$Q_g = 4$	Subunit I	5.23 Å	3.07 Å	3.27 Å
	Subunit II	4.38 Å	5.58 Å	3.65 Å
	Subunit III	6.09 Å	4.40 Å	5.34 Å
	Subunit IV	4.32 Å	5.84 Å	5.29 Å

Table 3.3. Distances for the salt bridges in hERG closed systems averaged for the four subunits. For D456-K525 and D411-K538 the values refer to the distance between the ϵ-Nitrogen of the lysines and the δ-Oxygen of the aspartates; for E544-R665 the values refer to the distance between the ϵ-Oxygen of the glutamates and the ϵ-Nitrogen of the arginines.

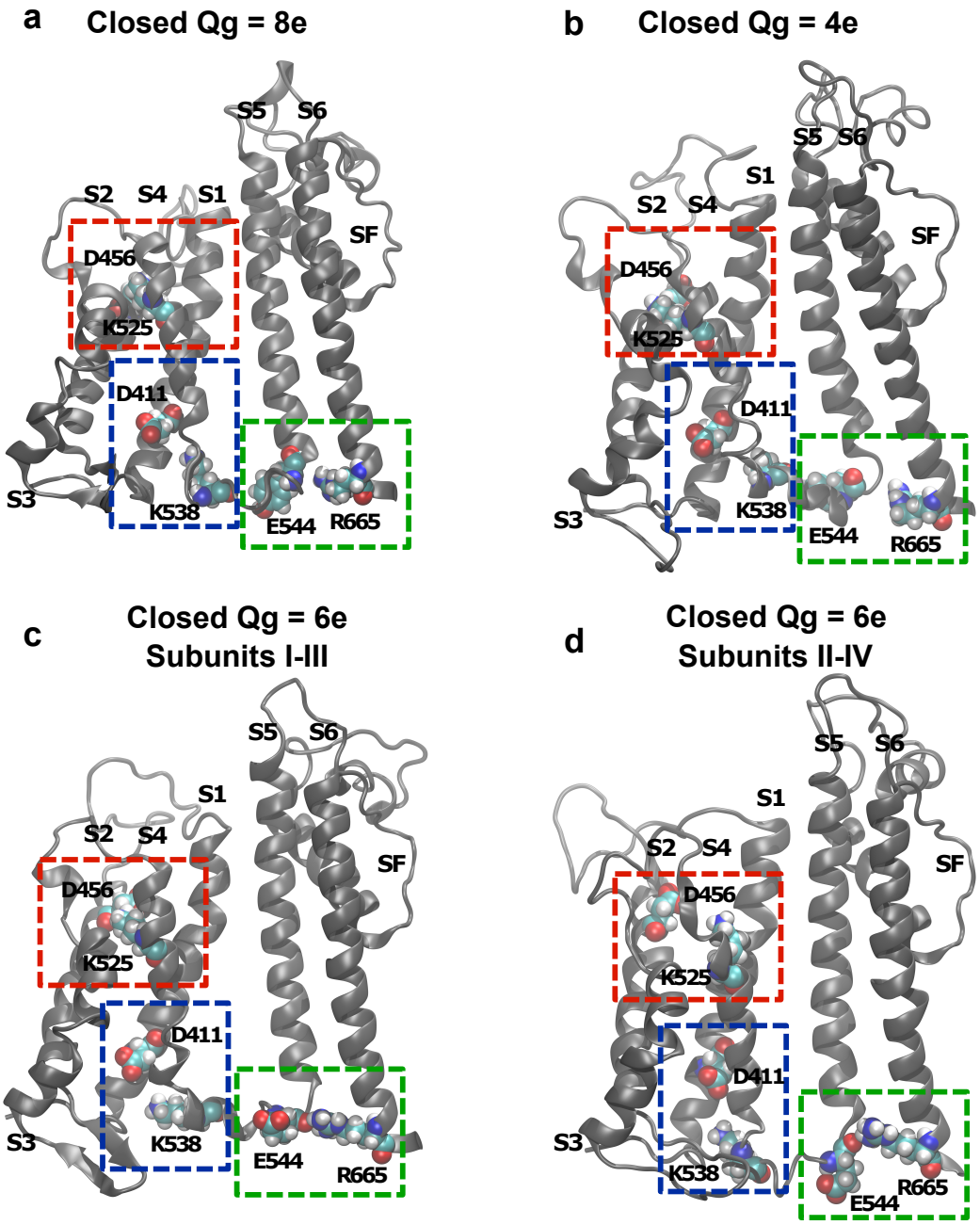

Figure 3.6. Interactions known to stabilize the closed state of hERG: D456-K525 [206], D411-K538 [206] and E544-R665 [163, 126]. For simplicity, in systems with $Q_g = 8e$ (**a**) and $Q_g = 4e$ (**b**) the first subunit is shown after the production run; Panels **c** and **d** show the first and the second subunits of the system with $Q_g = 6e$ that are in the same configuration of the third and the fourth subunits, respectively.

3.3 Contact analysis

The opening/closing of hERG was induced by Targeted Molecular Dynamics (TMD) simulations [168] using RMSD to drive the system from the open to all closed state isoforms. By computing a contact map for each frame of the TMD trajectories it was possible to follow the sequence of contact breakdown and formation events (Figure 3.8). The identification of conserved, formed or broken interactions in all subunits allowed us to formulate two hypothetical activation/deactivation mechanisms (Figure 3.7). The first mechanism is an intra-subunit one based on the

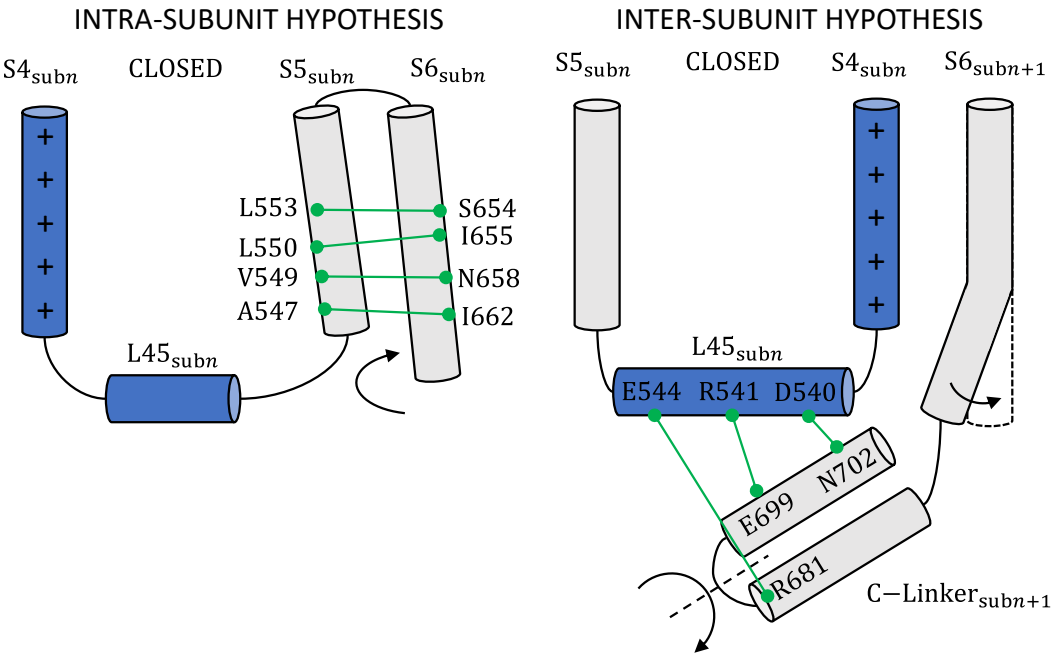

Figure 3.7. Illustration of the two activation/deactivation hypotheses displaying the relevant conserved interactions in the closed states.

conserved interactions between helices S5 and S6 of the same subunit (orange box in Figure 3.8): L553-S654, L550-I655, V549-N658, and A547-I662. The contact pattern suggests that helix S5 might directly push onto helix S6 of the same subunit causing its straightening and consequently the pore closure. By analysing the contact maps of the whole protein, a set of conserved bonds between loop L45 of subunit n and the C-Linker of subunit $n+1$ could be observed (green boxes in Figure 3.8): D540-N702, R541-E699, and E544-R681. In this case, it was hypothesized that the pressure exerted by loop L45 would induce a rotation of the C-Linker resulting in the straightening of helix S6 of subunit $n+1$ and the pore closure. This mechanism is therefore inter-subunit.

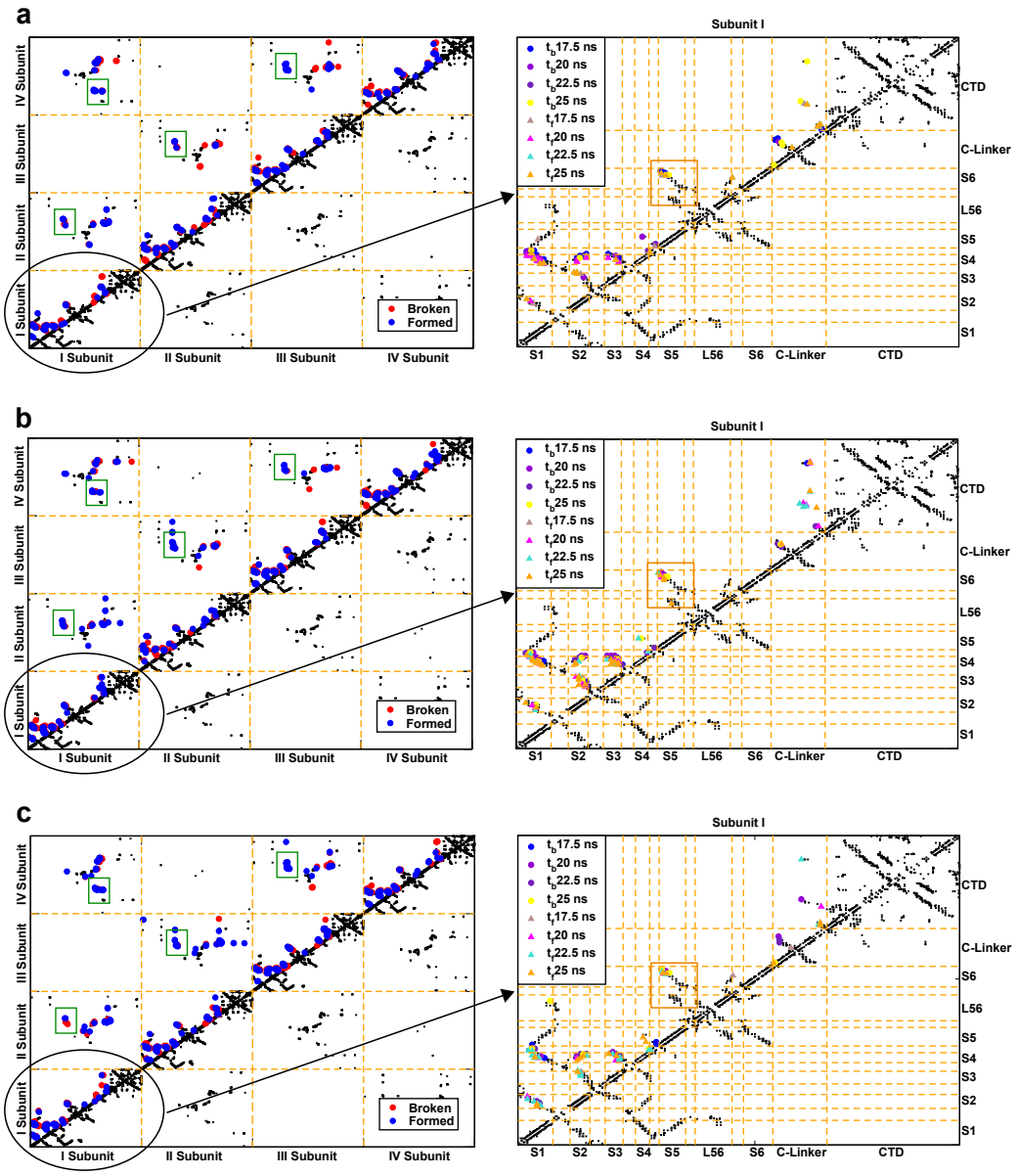

Figure 3.8. Contact maps computed during the transition from the open to closed state of the systems with $Q_g = 8e$, $Q_g = 6e$, and $Q_g = 4e$. Panels (**a**), (**b**), and (**c**) refer to the systems with $Q_g = 8e$, $Q_g = 6e$, and $Q_g = 4e$, respectively. The black dots represent the contacts in the initial open conformation while the coloured symbols indicate the contacts formed or broken at different times t during the TMD simulation. Conserved interactions between the loop L45 of subunit n and the C-Linker of subunit $n+1$ are highlighted in green boxes while those between helices S5 and S6 of subunit n are highlighted in orange boxes. For simplicity, for each system the first subunit contact maps are reported as single subunit maps.

3.4 Network analysis

3.4.1 Activation and deactivation paths

In order to discriminate the most realistic mechanism between those hypothesised from the contact analysis, the propagation of conformational changes inside the channel was studied employing a network approach (see [74, 60] for biophysics applications). In particular, the protein is represented as a graph where nodes correspond to protein residues and edges to interactions between pairs. Edges were assigned a weight based on the information distance $d_{ij} = -\log|Corr_{ij}|$, $Corr_{ij}$ being the correlation coefficient, that measured how efficiently information was transferred from one residue to the other. Using Dijkstra's algorithm [51], the minimal paths between source and sink regions were computed that were chosen to be centred on helix S4 or loop L45 and on helix S6, respectively.

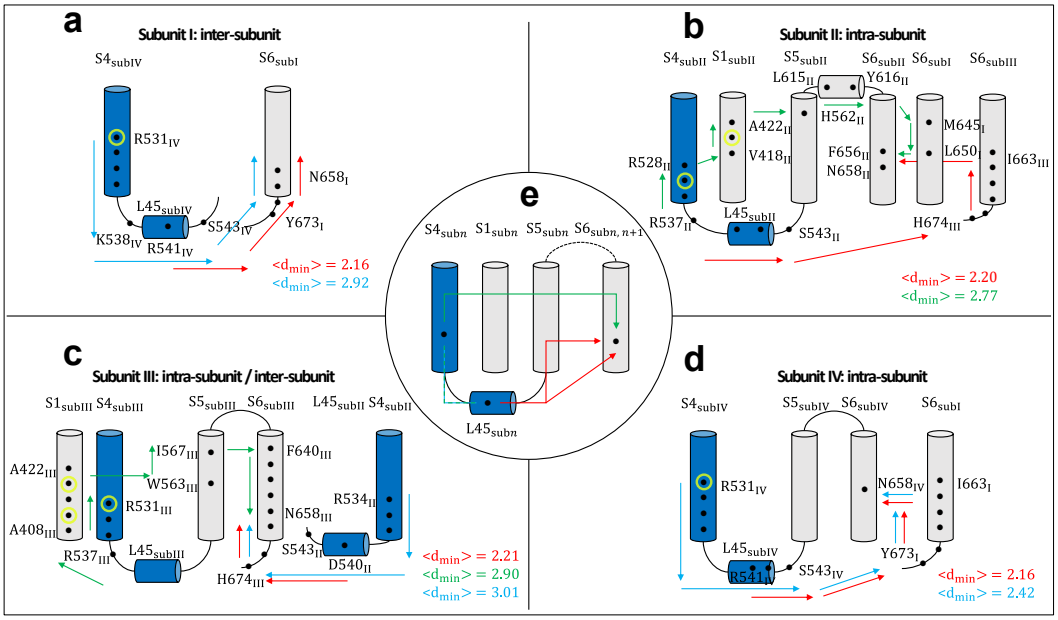

Figure 3.9. Activation/deactivation paths of the closed system with $Q_g = 8e$. Paths identified in subunits I (**a**), II (**b**), III (**c**), and IV (**d**). Panel **e** schematises the main families of gating paths identified in all systems. Arrows describe the preferred routes of motion propagation: blue arrows refer to S4→L45→S6 route; red arrows refer to the L45→S6 route; green arrows refer to S4→S1→S5→S6. Black dots correspond to residues on the path with CI> 0.15; yellow circles refer to the pathological mutation R531Q/W [130] known to alter the gating of the channel inducing the LQTS2. The mutations W410S, Y420C, and T421M impair both the trafficking and the gating [152]. Average minimal path lengths $\langle d_{\min} \rangle$ are also reported.

Two main families of paths that could be either intra- or inter-subunit (Figure 3.9) were identified. In the first family, the motion was propagated downwards along helix S4 and then along loop L45. From there, the motion was propagated directly to helix S6 either belonging to the same or to the neighbouring subunit (Figure 3.9a-b-c-d); this mechanism resembles the intra-subunit activation/deactivation hypothesis in Figure 3.8b. In the second family of paths, motion was propagated upwards along

helix S4 before moving to S1 and S5 of the same subunit (Figure 3.9b-c). From there, the path reached the helix S6 of the same subunit. This mechanism corresponds to the noncanonical path identified also in domain-swapped potassium channels [28]. The two identified paths are not mutually exclusive but can coexist in the same channel molecule; they were identified also in the systems with gating charge $6e$ and $4e$ (Figure 3.10)

Some interesting differences among the systems, however, were also detected. In the system with $Q_g = 4e$, there is an asymmetry between the paths originating from side S4 and side S5 of loop L45. In one of the four subunits the paths starting from side S5 followed the L45→S5→S6 route while those starting from side S4 followed the L45→S4→S1→S5→S6 route. In the other three subunits, all the paths originating from loop L45 were qualitatively similar regardless of their starting point. In all of the four subunits, however, the paths originating from side S5 of L45 were significantly shorter than those starting from side S4, typically accounting for a more effective propagation of motion. This trend was also confirmed in the systems with gating charge $8e$ and $6e$. These results show a functional asymmetry between the ends of loop L45 that is in agreement with experiments on hERG split channels [47]. It is to remark that in the system with $Q_g = 4e$, the S4→L45→S5→S6 path was always much shorter than S4→S1→S5→S6 such that the latter is expected to play a minor role in the dynamical coupling between S4-L45 and S6. Surprisingly, in the system with $Q_g = 6e$ the information transfer was generally less efficient than in the other systems. In particular, in the second and third subunits paths of average minimal length $\langle d_{\min} \rangle \approx 4$ in contrast with $\langle d_{\min} \rangle \approx 2$ in the other systems were found. Considering the logarithmic nature of this metric, a difference of two units in $d_{\min}$ corresponds to a difference of one order of magnitude in terms of correlations suggesting that in this system the S4-S6 coupling should be extremely weak. As a final remark, it was noted that none of the most efficient communication paths involved the C-Linker of the neighbouring subunit which disproved the hypothetical inter-subunit mechanism (Figure 3.8b).

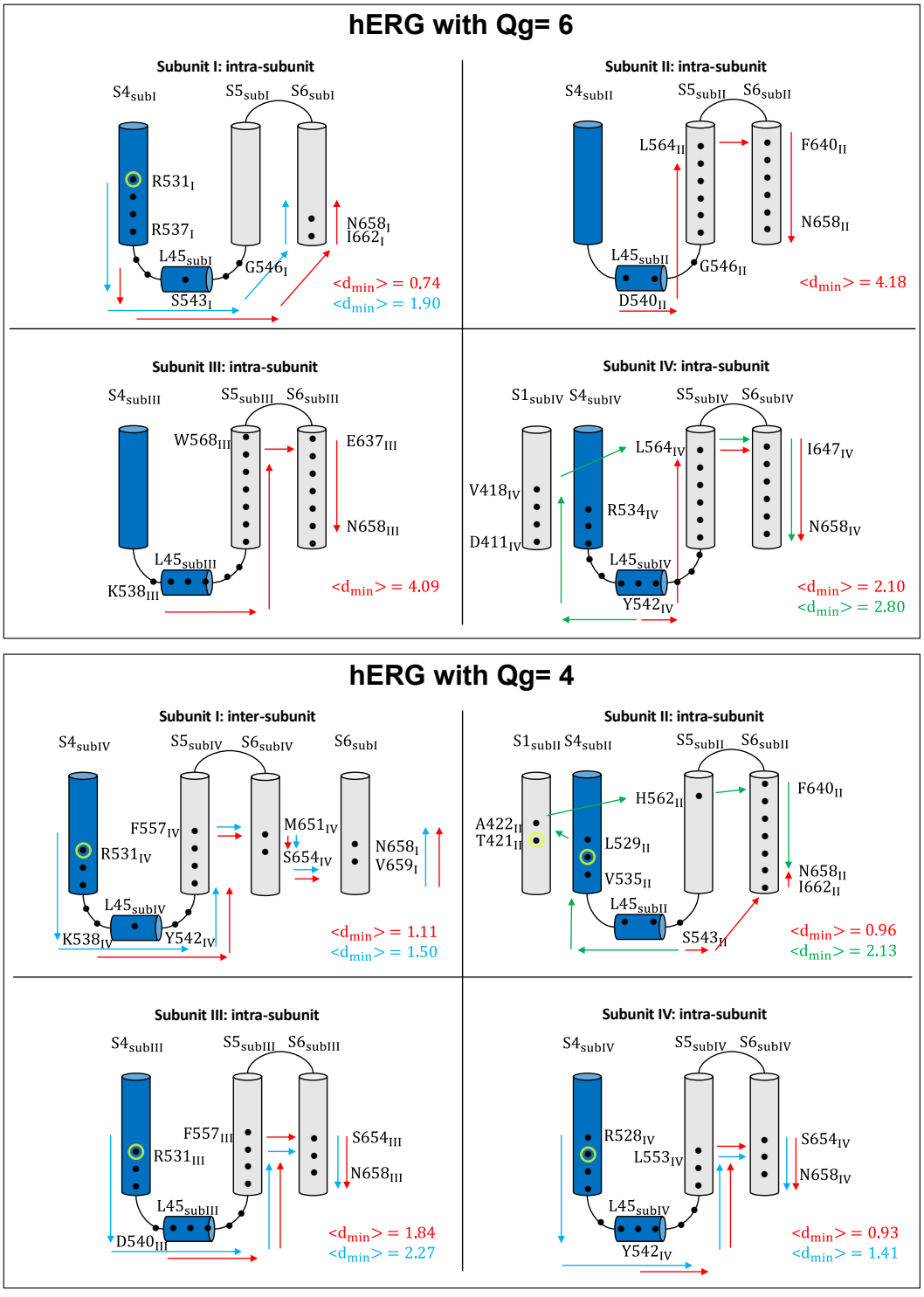

Figure 3.10. Activation/deactivation paths of the closed system with $Q_g = 6e$ and $Q_g = 4e$. Arrows describe the preferred routes of motion propagation: blue arrows refer to S4→L45→S6 route; red arrows refer to the L45→S6 route; green arrows refer to S4→S1→S5→S6. Black dots correspond to residues on the path with CI> 0.15; yellow circles refer to the pathological mutation R531Q/W [130] known to alter the gating of the channel inducing the LQTS2. The mutations W410S, Y420C, and T421M impair both the trafficking and the gating [152]. Average minimal path lengths $\langle d_{\min} \rangle$ are also reported.

3.4.2 Tentative production of the inactivated state

To clarify the role of the noncanonical path that has been suggested to play a role in the inactivation mechanism of Shaker channels [13], we tried to produce an inactivated state of hERG to analyze with the same network-theoretical approach. No experimental structure is available for hERG in the inactivated state. However, the paper by J. Li et al. [112] reveals a possible inactivated state of hERG produced *via* MD simulations. In this case, the system was initialized without ions inside the Selectivity Filter (SF) and was simulated for over 2 μs using the CHARMM force field [121, 100, 15]. They showed that the system, starting from the open configuration, spontaneously reaches a state characterized by an asymmetrical constriction of the SF measured at the level of G626 residues of two opposite subunits. Since this constriction was observed also in other K_v channels [44, 111], they suggested that this state could correspond to the inactivated state of hERG. Generally, experimental and theoretical evidences predict an average occupancy of 2 K^+ or 1 K^+ in the SF of potassium channels when they are open or inactivated, respectively [82, 79, 209, 4, 33]. In this context, to produce a more representative structure of hERG in the inactivated state, we tried to reproduce the system simulated by J. Li et al., [112]. We simulated the following systems:

1. System with 0 K^+ inside the SF
2. System with 1 K^+ inside the SF
3. System with 2 K^+ inside the SF

For each of them, simulations of 150 ns using the AMBER and CHARMM force fields were run. Moreover, since we were focusing on the inactivation that occurs at positive voltages, in the same vein of [132] we decided to simulate each system at 0 mV and +750 mV. The use of a potential much greater than physiological one is a common practice in computational biophysics to speed up equilibration (*e.g.* [132, 141]). We also simulated an extreme case where the channel has 2 K^+ inside the SF, applying an electric field of +900 mV to see further possible effects. As shown in Figure 3.11, each system reaches a structural stability based on the RMSD analysis.

Then, we compared the K^+ ion positions inside the SF in the starting configuration and at the end of the production run. Figure 3.12 shows that AMBER systems reached an inactivated configuration of the SF, defined in terms of K^+ occupancy where only one K^+ is present in the SF at the level of the S4 binding as suggested by Roux et al [112], only when the system is initialized with 1 K^+ inside the SF and positive electric field is applied. When no voltage is applied, only the system with 0 K^+ inside the SF had a K^+ ion at the S4 binding site. A different situation was observed in CHARMM systems, as described below. When systems were initialized with 2 K^+, the system simulated with 0 mV electric field reached a possible inactivated configuration referring to the K^+ positions: the ion at S1 moved to the extracellular side while the ion at S3 moved to the S4 binding site. Moreover, when the systems were initialized with 1 K^+ inside the SF, only with a positive electric field applied, the S4 binding site was occupied. Finally, with no ions

inside the SF at 0 mV no ion occupancy events were observed while at +750 mV the S4 binding site was occupied by a K^+ ion.

These results show that the ion occupancy associated to an inactivated configuration is reached only when an electric field is applied to the system. The only exception is represented by the AMBER system started with 0 K^+ inside the SF that reaches an inactivated configuration at 0 mV. Anyway, the CHARMM systems suggested by Li et al. [112] were not obtained.

Finally, we focused on the geometrical descriptors suggested by Li et al. [112] to see if the systems reached the inactivated asymmetrical constriction of the SF. As shown in Figure 3.13, the AMBER systems maintained an open SF while those simulated with CHARMM and initialized without ions inside the SF reached the suggested constriction. Anyway, also in these latter cases, the values of the distances between G626 of two opposite subunits were not the same as predicted by Li et al. [112] (green dashed lines).

Since the predicted inactivated state by Li et al. [112] was not obtained by our simulations and considering the heterogeneity of the results, we decided to compute the inactivation paths in the open state because it is the only experimental available structure and it is expected to be very similar to the inactivated state [195].

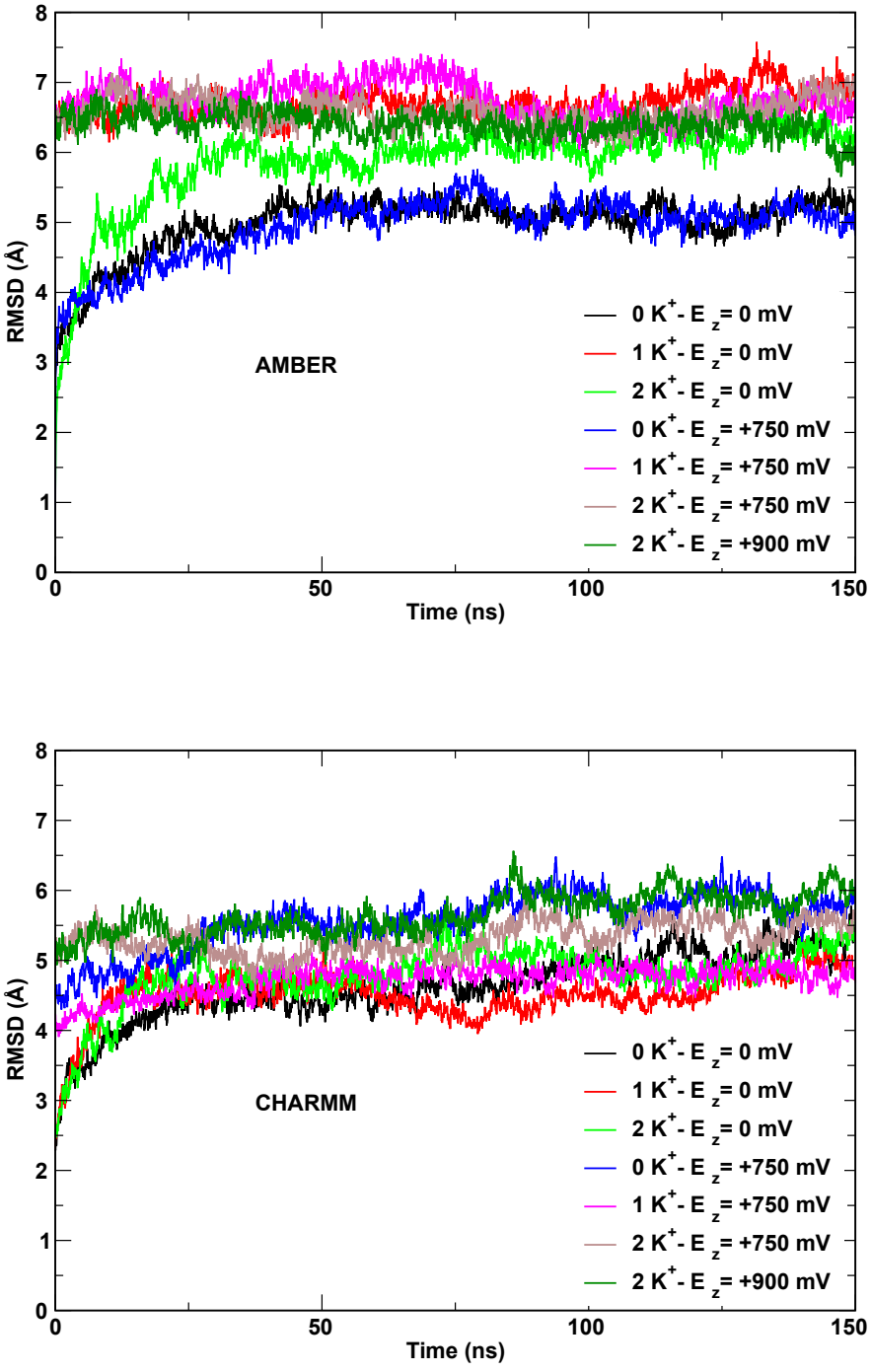

Figure 3.11. The root-mean-square deviation (RMSD) during the 150 ns equilibrium simulations of AMBER and CHARMM systems. The reference conformation is the starting configuration of each system before the equilibration. The superposition of the current and reference conformations was performed using all backbone atoms. The RMSD calculation was performed using all backbone atoms.

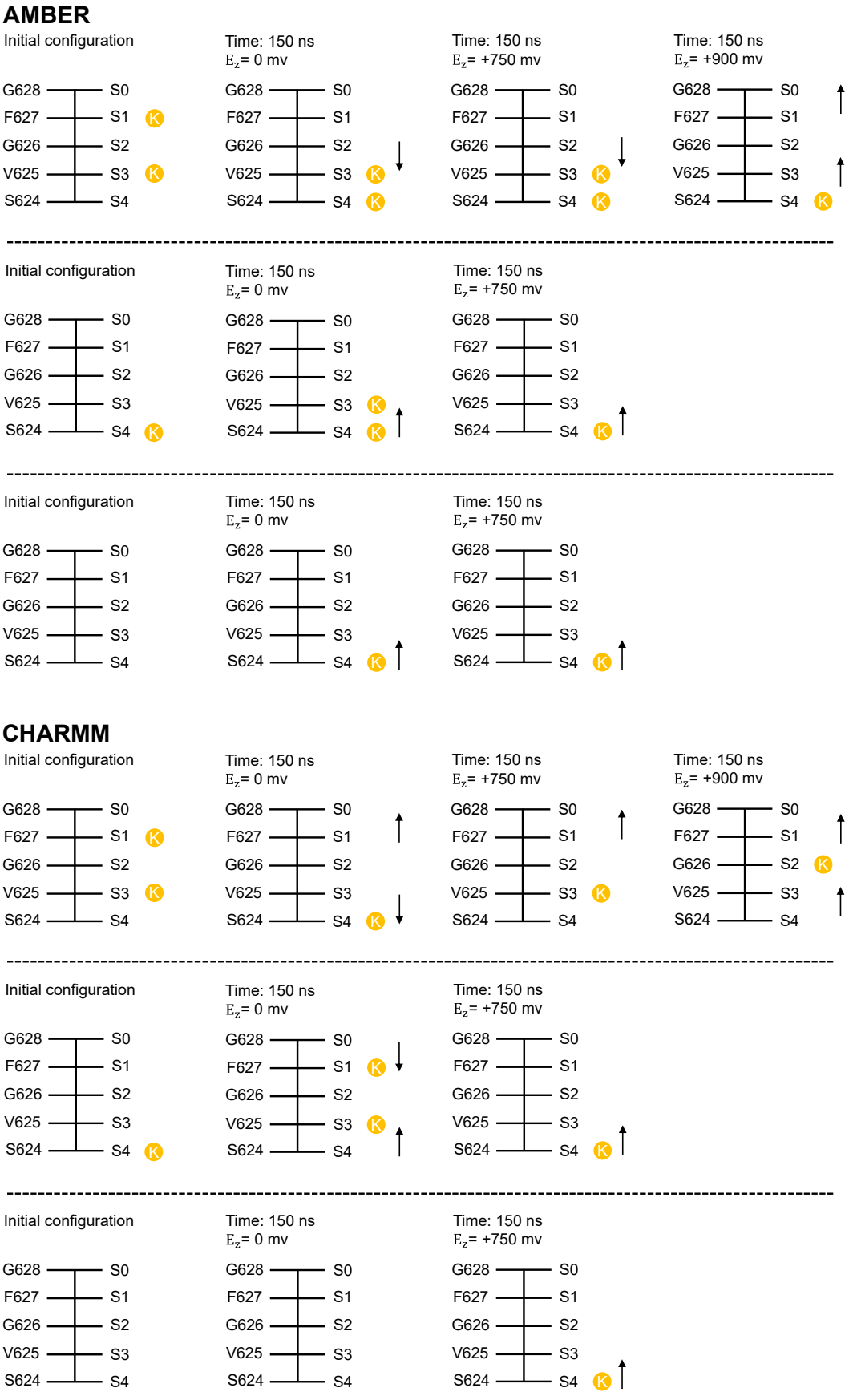

Figure 3.12. Ion occupancy in AMBER and CHARMM systems at the end of the 150 ns production runs. Arrows describe the movements of ions during the production runs with respect to the initial configuration.

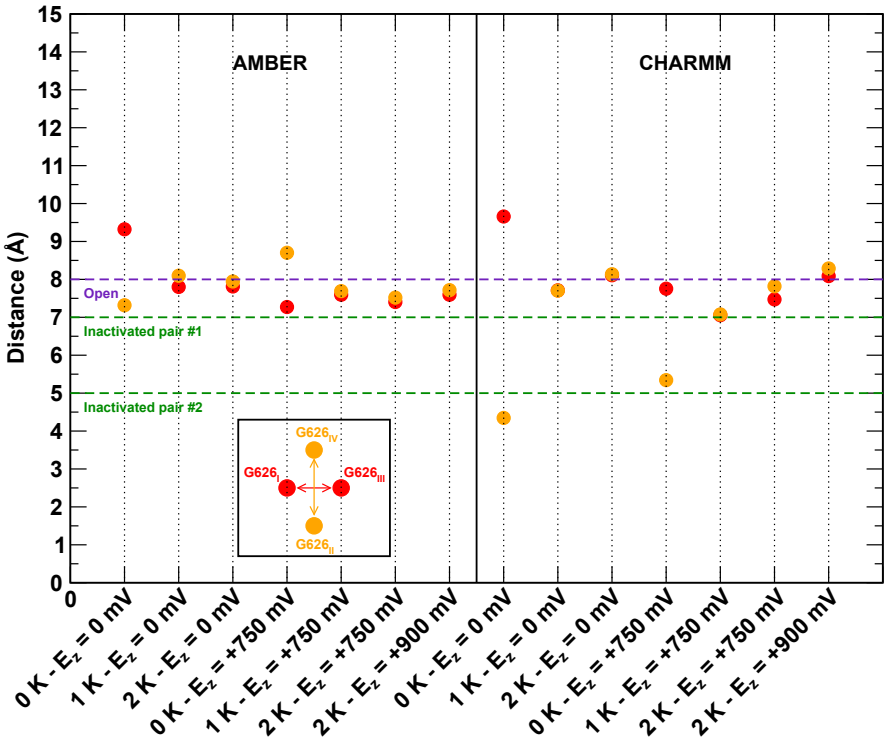

Figure 3.13. Distance between G626 of two opposite subunits in AMBER and CHARMM force fields. The blue dashed line corresponds to the value in the open state; the green dashed lines to values in the inactivated state (first and second couples of G626 of two opposite subunits) predicted by Li et al. [112]

3.4.3 Inactivation paths

The inactivation path was computed analyzing the open state trajectory of hERG. As described before, the protein was represented as a graph and a weight was assigned to edges $w_{ij} = -log(C_{ij}M_{ij})$ which, in this case, quantifies the electromechanical coupling in terms of contacts between residues and correlations of their motion. In the same way, Dijkstra's algorithm [51] was used to determine the shortest paths between S4-SF (see Methods). The source region was set on helix S4 because it appears that the inactivation is intrinsically voltage-sensitive [61]. In the same way, the sink region was centered on the SF because many evidences show that the C-type inactivation is associated to conformational changes of the SF [112]. A path following the S4→S1→S5→P-Loop→SF route was obtained suggesting to be involved in the C-type inactivation of hERG channels. The motion propagates from helix S4 passing

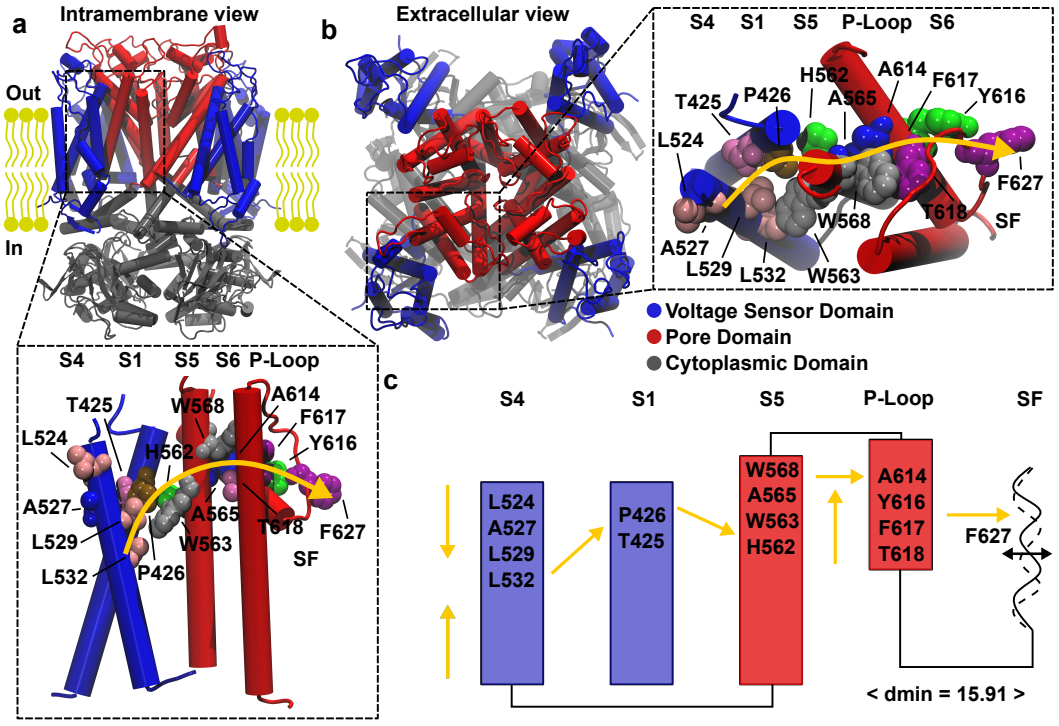

Figure 3.14. Molecular basis for the noncanonical inactivation path in the hERG channel. Panels (**a**) and (**b**) show the intramembrane and extracellular views of the open state from MD simulations of the wild type colored by domains: VSD in blue and PD in red. Panel (**c**) schematizes the noncanonical paths involved in the inactivation (yellow arrows) that couple S4-SF. Average minimal path length $\langle d_{\min} \rangle$ is also reported as the mean over the four subunits.

through S1 and S5 following the same noncanonical route as previously described for the closed trajectories involved in the activation paths (Figure 3.9). Then, *via* the P-Loop, it reaches the SF determining the constriction relevant in the C-type inactivation.

3.4.4 The role of residues in the gating paths

The role of each residue in the predicted activation and inactivation paths was quantified by computing a Centrality Index (CI) and performing betweenness centrality [23] calculations on the wild type open and closed states. They correspond to the fraction of minimal paths in which a residue is present and express the importance of it in the transfer of motion. The Centrality Index (CI) assumes values in the interval $[0, 1]$ and if $CI = 1$ it means that the residue plays a key role in the communication path. Since in the calculation of the Centrality Index only one minimal path is considered between two residues, we also performed betweenness (B) centrality calculations [23] using the NetworkX software [76] where all the minimal paths connecting two residues are considered (see Methods). B assumes values in the interval $[0, B_{max}]$ and higher values of B correspond to a more important role in the communication path. As shown in Table 3.4, higher values of CI correspond to higher values of B showing a good agreement between these quantities.

Residue		Activation		Inactivation	
		CI	B	CI	B
S1	A408	CI $\geq$ 0.95	4.11 $\pm$ 0.1	CI $\leq$ 0.15	0.17 $\pm$ 0.1
	W410	CI $\geq$ 0.95	4.95 $\pm$ 0.2	CI $\leq$ 0.15	0.23 $\pm$ 0.1
	D411	CI $\geq$ 0.95	4.48 $\pm$ 0.2	CI $\leq$ 0.15	0.56 $\pm$ 0.1
	V418	CI $\geq$ 0.95	3.95 $\pm$ 0.2	0.25 $\leq$ CI $\leq$ 0.45	0.85 $\pm$ 0.1
	Y420	CI $\geq$ 0.95	4.74 $\pm$ 0.2	0.35 $\leq$ CI $\leq$ 0.45	1.13 $\pm$ 0.2
	T421	CI $\geq$ 0.95	4.05 $\pm$ 0.1	0.35 $\leq$ CI $\leq$ 0.45	1.90 $\pm$ 0.1
	A422	CI $\geq$ 0.95	4.12 $\pm$ 0.3	0.85 $\leq$ CI $\leq$ 0.95	2.25 $\pm$ 0.2
	T425	CI $\geq$ 0.95	3.60 $\pm$ 0.2	CI $\geq$ 0.95	4.58 $\pm$ 0.2
	P426	CI $\geq$ 0.95	8.29 $\pm$ 0.2	CI $\geq$ 0.95	6.60 $\pm$ 0.4
S4	L524	0.25 $\leq$ CI $\leq$ 0.45	1.12 $\pm$ 0.2	0.25 $\leq$ CI $\leq$ 0.45	1.20 $\pm$ 0.1
	A527	0.55 $\leq$ CI $\leq$ 0.65	1.49 $\pm$ 0.2	CI $\leq$ 0.15	0.19 $\pm$ 0.1
	R528	0.85 $\leq$ CI $\leq$ 0.95	4.14 $\pm$ 0.5	0.85 $\leq$ CI $\leq$ 0.95	4.08 $\pm$ 0.2
	L529	0.85 $\leq$ CI $\leq$ 0.95	2.60 $\pm$ 0.2	0.25 $\leq$ CI $\leq$ 0.45	1.81 $\pm$ 0.1
	L530	CI $\leq$ 0.15	2.45 $\pm$ 0.3	CI $\leq$ 0.15	0.40 $\pm$ 0.1
	R531	0.55 $\leq$ CI $\leq$ 0.65	2.97 $\pm$ 0.1	0.55 $\leq$ CI $\leq$ 0.65	3.04 $\pm$ 0.2
	L532	0.55 $\leq$ CI $\leq$ 0.65	2.10 $\pm$ 0.2	0.85 $\leq$ CI $\leq$ 0.95	3.00 $\pm$ 0.1
	R534	0.35 $\leq$ CI $\leq$ 0.45	2.16 $\pm$ 0.2	0.35 $\leq$ CI $\leq$ 0.45	1.74 $\pm$ 0.3
	V535	0.25 $\leq$ CI $\leq$ 0.45	2.53 $\pm$ 0.1	CI $\leq$ 0.15	1.14 $\pm$ 0.1
	A536	0.85 $\leq$ CI $\leq$ 0.95	3.10 $\pm$ 0.1	CI $\leq$ 0.15	0.12 $\pm$ 0.1
L45	R537	CI $\geq$ 0.95	5.58 $\pm$ 0.2	0.20 $\leq$ CI $\leq$ 0.35	0.18 $\pm$ 0.1
	K538	CI $\geq$ 0.95	6.01 $\pm$ 0.1	0.20 $\leq$ CI $\leq$ 0.35	0.13 $\pm$ 0.1
	D540	CI $\geq$ 0.95	7.19 $\pm$ 0.3	CI $\leq$ 0.15	0.11 $\pm$ 0.1
	R541	CI $\geq$ 0.95	7.54 $\pm$ 0.2	CI $\leq$ 0.15	0.00
	Y542	CI $\geq$ 0.95	7.17 $\pm$ 0.2	CI $\leq$ 0.15	0.00
	S543	CI $\geq$ 0.95	7.41 $\pm$ 0.1	CI $\leq$ 0.15	0.00
	E544	CI $\geq$ 0.95	6.54 $\pm$ 0.1	CI $\leq$ 0.15	0.00
	G546	CI $\geq$ 0.95	9.14 $\pm$ 0.2	CI $\leq$ 0.15	0.00
	L552	CI $\geq$ 0.95	7.59 $\pm$ 0.1	CI $\leq$ 0.15	0.00
	L553	0.85 $\leq$ CI $\leq$ 0.95	3.94 $\pm$ 0.2	CI $\leq$ 0.15	0.00
	F557	0.85 $\leq$ CI $\leq$ 0.95	3.91 $\pm$ 0.1	CI $\leq$ 0.15	0.00
	A558	0.70 $\leq$ CI $\leq$ 0.80	3.98 $\pm$ 0.1	CI $\leq$ 0.15	0.11 $\pm$ 0.1
	L559	0.70 $\leq$ CI $\leq$ 0.80	3.92 $\pm$ 0.1	CI $\leq$ 0.15	0.15 $\pm$ 0.1
	H562	CI $\geq$ 0.95	7.30 $\pm$ 0.1	0.70 $\leq$ CI $\leq$ 0.80	2.50 $\pm$ 0.1
	W563	0.70 $\leq$ CI $\leq$ 0.80	3.75 $\pm$ 0.3	CI $\leq$ 0.15	0.35 $\pm$ 0.2
	L564	0.70 $\leq$ CI $\leq$ 0.80	3.79 $\pm$ 0.2	CI $\leq$ 0.15	0.51 $\pm$ 0.1
	A565	0.85 $\leq$ CI $\leq$ 0.95	4.00 $\pm$ 0.1	0.45 $\leq$ CI $\leq$ 0.55	2.25 $\pm$ 0.3

	I567	$0.70 \leq CI \leq 0.80$	3.84 ± 0.2	$0.70 \leq CI \leq 0.80$	3.1 ± 0.1
	W568	$CI \geq 0.95$	5.90 ± 0.2	$CI \geq 0.95$	5.40 ± 0.2
P-Loop	A614	$CI \leq 0.15$	0.79 ± 0.1	$0.70 \leq CI \leq 0.80$	2.75 ± 0.4
	L615	$0.70 \leq CI \leq 0.80$	1.54 ± 0.2	$CI \geq 0.95$	3.94 ± 0.2
	Y616	$0.70 \leq CI \leq 0.80$	3.50 ± 0.1	$CI \geq 0.95$	5.05 ± 0.2
	F617	$CI \leq 0.15$	3.50 ± 0.1	$CI \geq 0.95$	4.95 ± 0.2
	T618	$CI \leq 0.15$	2.50 ± 0.3	$0.65 \leq CI \leq 0.75$	1.75 ± 0.3
SF	G626	$CI \leq 0.15$	0.00	$CI \geq 0.95$	10.31 ± 0.2
	F627	$CI \leq 0.15$	0.00	$CI \geq 0.95$	7.90 ± 0.1
S6	E637	$0.75 \leq CI \leq 0.85$	1.65 ± 0.1	$CI \leq 0.15$	3.65 ± 0.3
	F640	$0.70 \leq CI \leq 0.80$	1.25 ± 0.1	$CI \leq 0.15$	0.80 ± 0.4
	V644	$0.70 \leq CI \leq 0.80$	3.37 ± 0.1	$CI \leq 0.15$	0.42 ± 0.2
	M645	$CI \geq 0.95$	4.11 ± 0.3	$CI \leq 0.15$	0.19 ± 0.1
	I647	$CI \geq 0.95$	7.31 ± 0.1	$CI \leq 0.15$	0.23 ± 0.1
	L650	$CI \geq 0.95$	14.62 ± 0.2	$CI \leq 0.15$	0.10 ± 0.1
	M651	$CI \geq 0.95$	9.46 ± 0.1	$CI \leq 0.15$	0.00
	S654	$0.45 \leq CI \leq 0.55$	8.00 ± 0.3	$CI \leq 0.15$	0.01 ± 0.1
	F656	$0.75 \leq CI \leq 0.85$	10.15 ± 0.1	$CI \leq 0.15$	0.00
	N658	$CI \geq 0.95$	8.50 ± 0.1	$CI \leq 0.15$	0.00
	I662	$CI \geq 0.95$	8.16 ± 0.2	$CI \leq 0.15$	0.00
	I663	$CI \geq 0.95$	9.01 ± 0.1	$CI \leq 0.15$	0.00
C-Linker	Y673	$CI \geq 0.95$	8.95 ± 0.2	$CI \leq 0.15$	0.00
	H674	$CI \geq 0.95$	7.49 ± 0.2	$CI \leq 0.15$	0.00

Table 3.4. Centrality Index (CI) and betweenness (B) values of each residue implicated in the activation and inactivation paths.

For the activation, residues on the loop L45 and on helices S1 and S6 have the highest values of CI and B while for the inactivation helices S1, S5 and the P-Loop play the most important role in the path. Interestingly, we found that the interfaces S4/S1 and S1/S5 are involved in both the activation and inactivation paths suggesting a dual role of the noncanonical path in non-domain-swapped channels such as hERG. For this reason, we focused on the noncanonical paths that in the first part follow the same route, comparing the B values of residues that lay on them with the free-energy perturbation computed by electro-physiological experiments. This part of the work was done in collaboration with the group led by Prof. Bezanilla from the University of Chicago that realized all the electrophysiological experiments. In particular, from their experimental measurements the free-energy perturbation is obtained. It corresponds to $\Delta\Delta G = \Delta G_{mutant} - \Delta G_{wt} = (zV_{0.5}F)_{mutant} - (zV_{0.5}F)_{wt}$ where z is the apparent charge of the activation or inactivation expressed in multiples of elementary charge, $V_{0.5}$ is the voltage for 50% of the maximal conductance and F is the Faraday constant. From the plots shown in Figure 3.15, it is possible to appreciate correlations between the betweenness centrality with the free-energy perturbation. Higher effects on the gating are determined by mutations of residues that were predicted to have a higher B value.

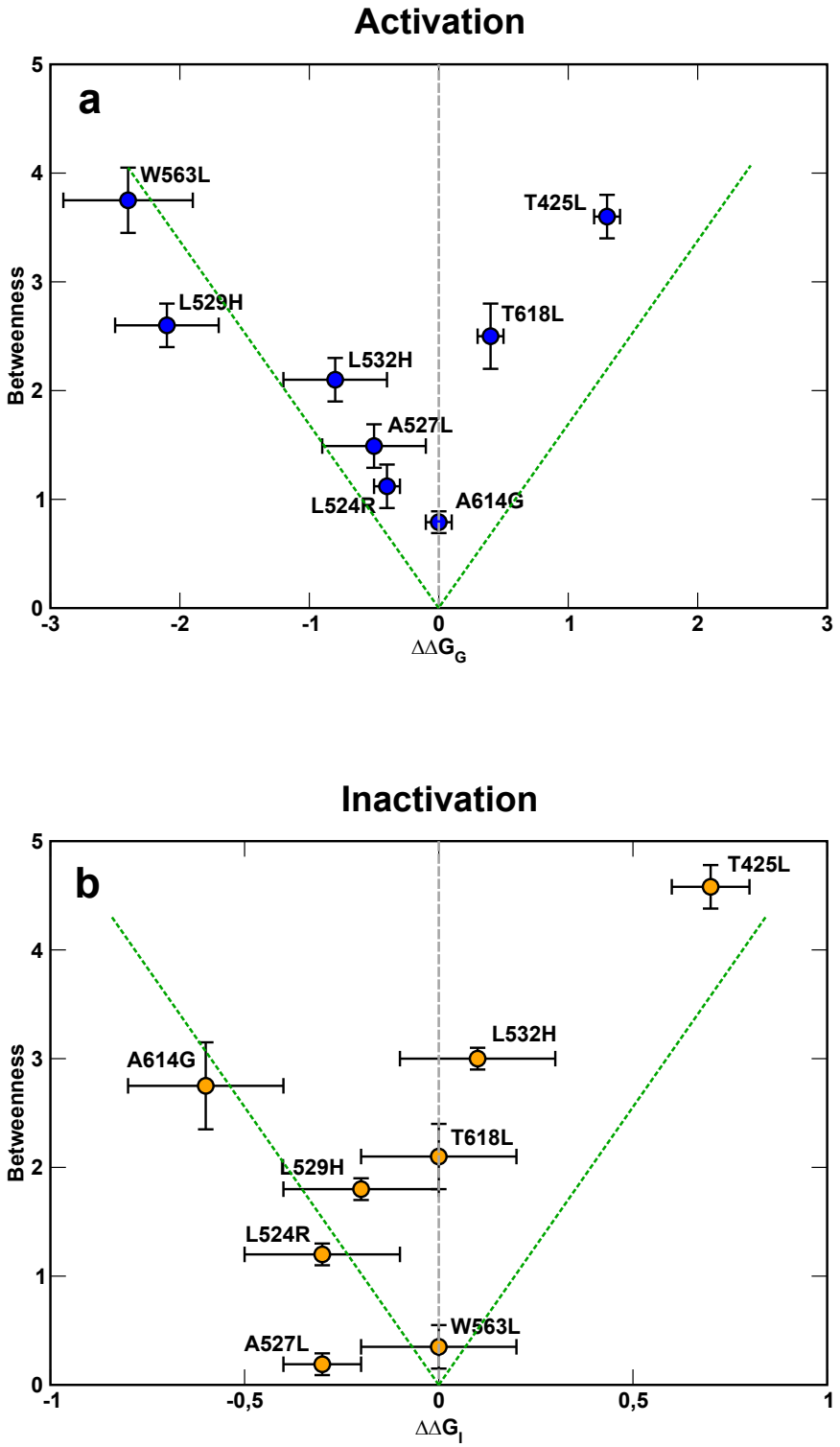

Figure 3.15. Scatter plots comparing the betweenness centrality of residues along the noncanonical paths against the free-energy perturbation of activation ($\Delta\Delta G_G$) (**a**) and of inactivation ($\Delta\Delta G_I$) (**b**).

3.5 Simulations of mutants

The reliability of our results was tested producing computational mutants that have been experimentally identified to impair the gating mechanism of hERG. For instance, mutants T421M [152] and R531Q [130] are known to traffic normally while they are characterized by a depolarizing or hyperpolarizing shift of the half-maximal activation voltage $V_{1/2}$, indicating an impairment of the activation or deactivation processes. In both cases activation/deactivation follow qualitatively similar routes as compared to the wild type but their length is significantly increased of two orders of magnitude, underscoring that the VSD-PD coupling becomes weaker. As a negative control we also simulated two random mutants not lying along the predicted communication paths, A505V and F627A. Indeed, these mutations appear not to affect either the communication paths or their length that remain unchanged as compared to the wild type.

Then, we focused on the noncanonical activation and inactivation paths. Precisely, in collaboration with the group by Prof. Bezanilla from the University of Chicago, we mutated computationally and experimentally residues T425, P426, A527, H562, W563, A565, W568, A614, Y616, F617, and T618 to leucine to perturb the identified chain and assess their role in the paths. Moreover, mutations of residues on the S4 helix (L524R, L529H, and L532H) were produced as they had already been identified to affect the Shaker noncanonical gating mechanism [13]. Finally, A614 was mutated into glycine because bulkier residues such as valine or leucine did not experimentally exhibit constructs able to generate currents. Due to the lack of expression in the experiments, we were not able to characterize the following mutants: P426L, H562L, A565L, A614L. We analyzed 150 ns simulation of each mutant with the same network theoretical approach using the more accurate metrics $w_{ij} = -log(C_{ij}M_{ij})$ that consider both the contacts and the correlation of motion between residues. To relate the computational and the experimental data, we plotted the mutational variation of the average minimal noncanonical path length (Δd_{min}) against the free-energy perturbation of activation ($\Delta\Delta G_G$) and of inactivation ($\Delta\Delta G_I$). From the plots shown in Figure 3.16, correlations were observed between Δd_{min} with $\Delta\Delta G_G$ for activation and $\Delta\Delta G_I$ for inactivation. These plots highlight that lower efficiency in the motion propagation (higher Δd_{min}) correlates increasing impairment of the activation/inactivation mechanisms (higher $\Delta\Delta G$). Similarly, a more efficient transfer of motion (lower Δd_{min}) correlates with enhanced mechanisms measured by experiments (lower $\Delta\Delta G$). These data demonstrate a fair agreement between computational and experimental results reinforcing that the residues identified are part of the noncanonical electromechanical coupling in hERG.

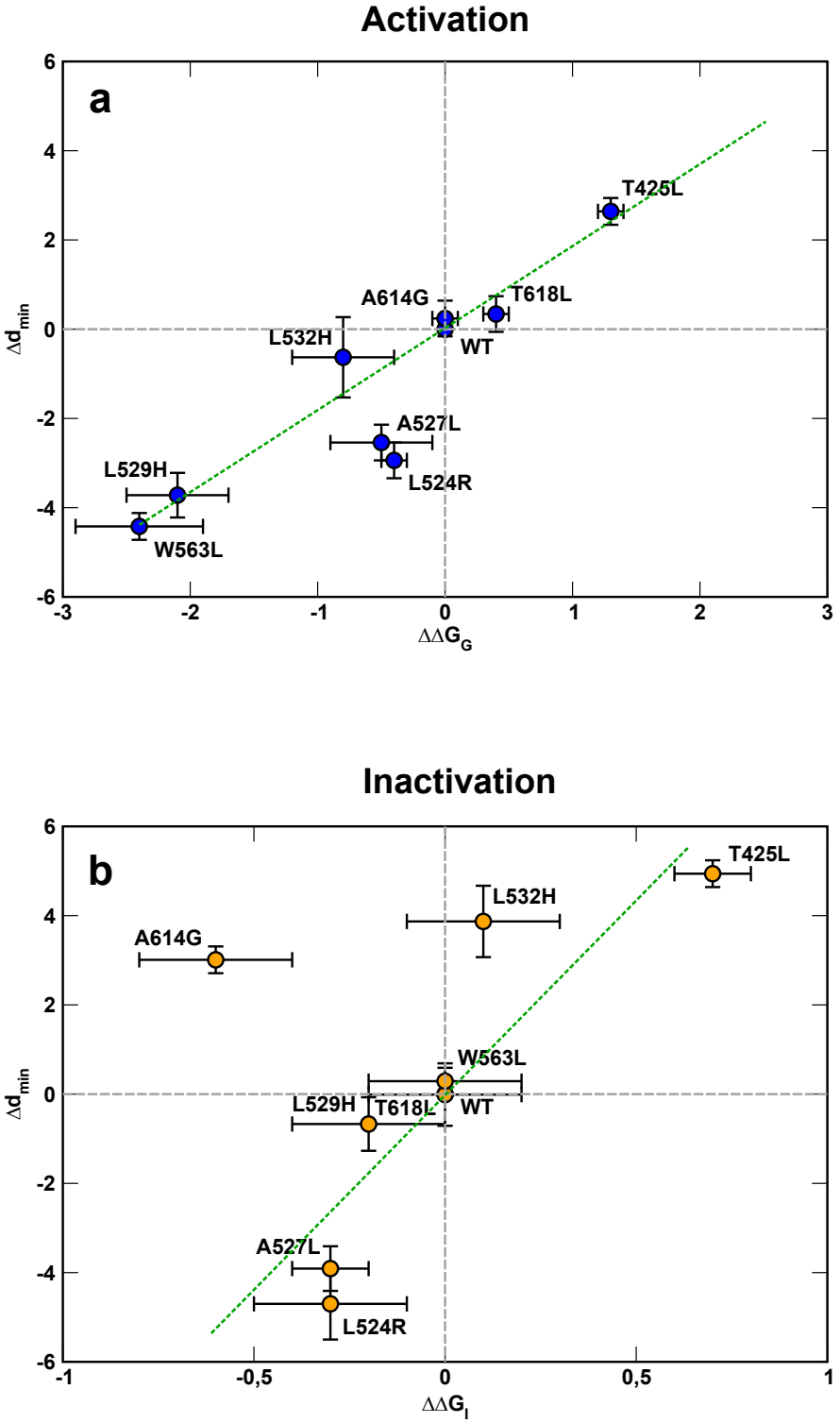

Figure 3.16. Scatter plots comparing the Δd_{min} of mutations along the noncanonical paths against the free-energy perturbation of activation ($\Delta\Delta G_G$) (**a**) and of inactivation ($\Delta\Delta G_I$) (**b**).

3.6 Simulations of split channels

In order to further clarify the activation/deactivation mechanisms and confirm the role of the L45 loop that plays a key role in the gating of domain-swapped channels [26], the split channels of Ref. [47] were reproduced *in silico*, which shows that cutting the L45 loop near the S4 helix a destabilization of the closed state is caused while channels split near the S5 helix open and close like the wild type. Starting from the pre-equilibrated closed states, two split channels were produced introducing a disconnection before D540 and after G546, respectively (Figure 3.17). In agreement with the literature [47], no communication path was detected in

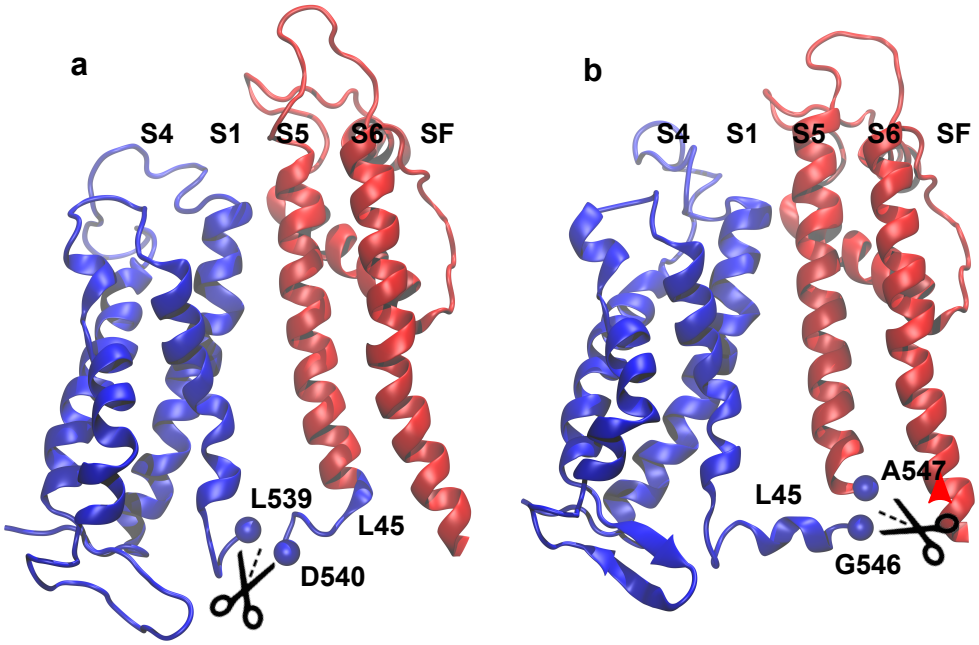

Figure 3.17. Split channels disconnected before D540 (**a**) and after G546 (**b**).

channels split before D540 (Figure 3.17a), while those cut after G546 exhibited the same activation/deactivation paths as in the wild type (Figure 3.17b). More specifically, in the G546-split system, the canonical path S4→L45→S6 followed the same route as in the wild type and have approximately the same length. Moreover, the noncanonical path S4→S1→S5→S6 was also qualitatively similar to that of the wild type, but somewhat longer. In the D540-split channel, no path was identified. Unexpectedly, a noncanonical activation/deactivation path could not be found, which does not pass through the L45 loop (green line in Figure 3.9e). This result could be justified observing that in the G546-split channel the S4-S1 distance matched that of the close state in the wild type, whereas in the D540-split construct the S4-S1 distance was larger than that of the wild-type closed state reaching values close to that of the open state at the bottom of the two helices (Table 3.5). These results confirm the difficulty of the D540 split channel to reach the closed state highlighted in the experiments [47] and rationalize the pattern in terms of an interruption of both communication paths.

	Open WT	Closed WT	Split D540	Split G546
S4-S1 distance (Å)	12.0	7.0	10.0	7.5
S1-S5 distance (Å)	8.5	9.0	11.0	8.5

Table 3.5. Average distances between S4-S1 and S1-S5 in WT and split channels.

3.7 Pseudo Potential of Mean Force

Useful mechanistic insights in the hERG activation/deactivation mechanisms are provided by a few geometrical observables that were monitored during the transition (Figure 3.18a-b): displacement and rotation of helices S4; bending of helices S6; rotation of the cytosolic domains with respect to the transmembrane ones. Since the TMD simulations were run out of equilibrium, the calculation of a Potential of Mean Force (PMF) is, strictly speaking, not possible. The driving speed is however sufficiently slow to allow to compute the pseudo-PMF graphs shown in Figure 3.18, see Methods for details. In Figure 3.18c the rotation and displacement of helix S4 proceed simultaneously almost throughout their entire range of values. However, when the roto-translation process is almost completed, the low free energy region of the PMF shows a decrease in slope which means that rotation continues even after the translation has come to an end. Near the point of slope change a discontinuity indicates the presence of a PMF barrier, probably depending on steric clashes that slowed the rotation. In the systems with gating charge $Q_g = 6e$ and $Q_g = 4e$ the change in slope tends to occur earlier and the discontinuity is more pronounced (Figure 3.19 and Figure 3.20). Figure 3.18d-e shows that helix S6 bending and the roto-translation of helix S4 also proceed simultaneously for a large part of their range of values. However, after helix S6 bending has reached its maximum value, the roto-translation of helix S4 continues. This observation confirms our intra-subunit activation/deactivation hypothesis: since helix S4 is close to helix S5, a small initial motion of helix S4 is sufficient to induce a correspondingly small motion of helix S5 that pushes onto S6 inducing its bending. The function of helix S4, however, is not limited to the propagation of motion to helix S6. The ongoing motion of helix S4 after the bending of helix S6 is completed is probably finalized to the establishment of contacts (with a possible regulatory function) between L45 and the C-linker and/or the CTD. This pattern is also displayed by the systems with gating charge $Q_g = 6e$ (Figure 3.19b-c) and $Q_g = 4e$ (Figure 3.20b-c).

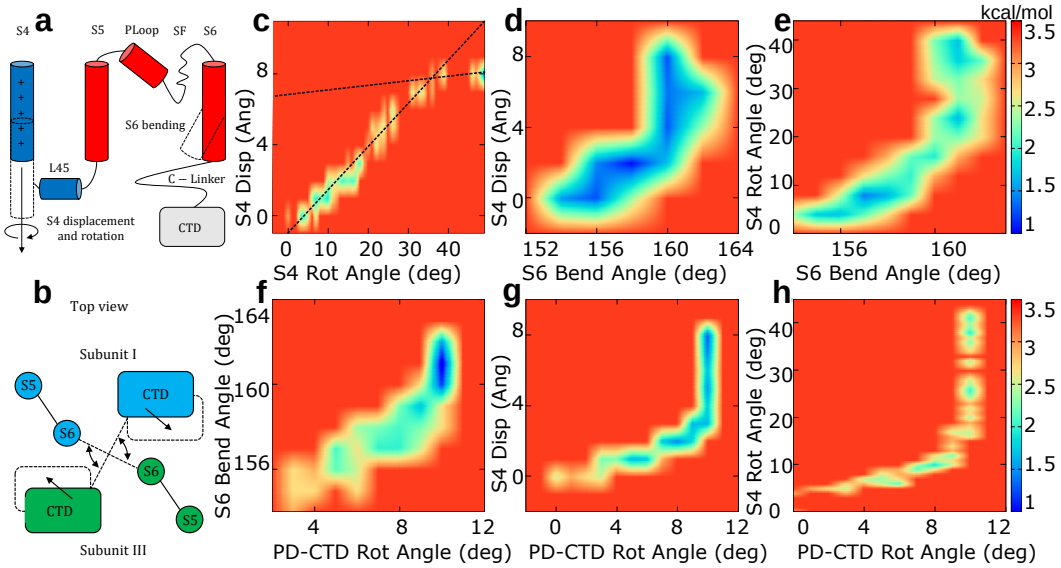

Figure 3.18. Pseudo-potential of Mean Force for hERG closed state with $Q_g = 8e$ as a function of geometrical descriptors, relevant for the O→C transition. The geometrical observables are: displacement and rotation of helices S4 and bending of helices S6 (**a**); rotation of the cytosolic domains with respect to the transmembrane ones (**b**). Pseudo-PMF maps as follows: S4 rotation vs S4 displacement (**c**); S6 bending vs S4 displacement (**d**); S6 bending vs S4 rotation (**e**); PD-CTD rotation vs S6 bending (**f**); PD-CTD rotation vs S4 displacement (**g**); PD-CTD rotation vs S4 rotation (**h**). Dashed lines are a guide to the eye. Bin widths are as follows: S4 displacement: 1.0 Å; S4 rotation: 2°; S6 bending: 1°; PD-CTD rot: 1°. Free energies were expressed in kcal/mol.

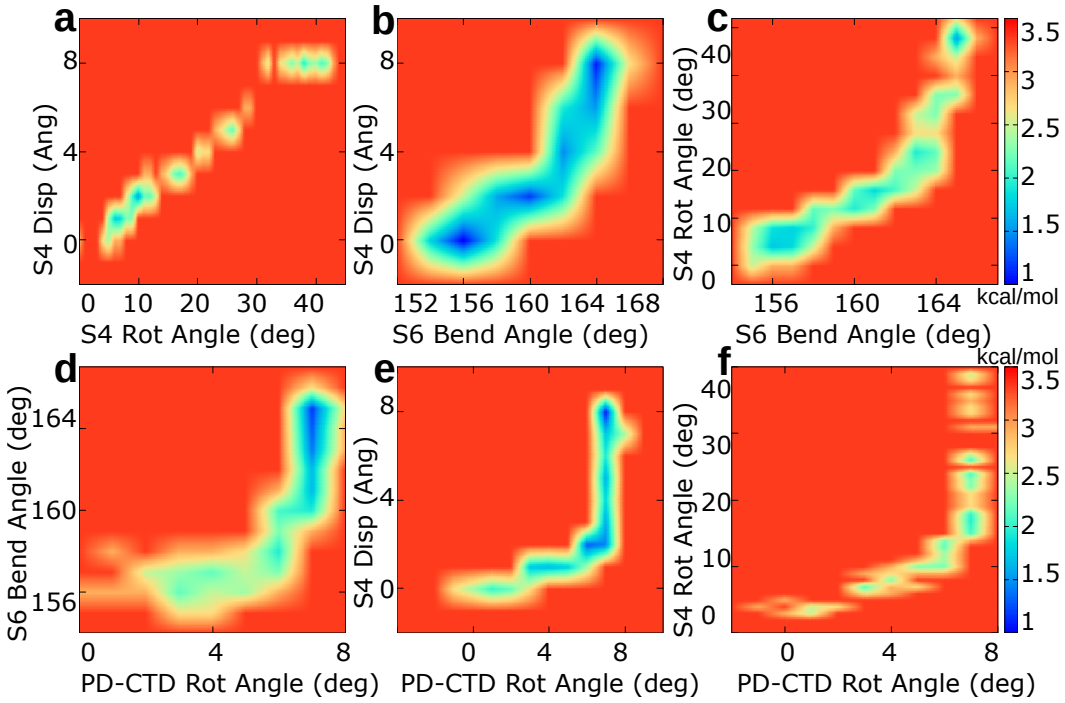

Figure 3.19. Pseudo-potential of Mean Force for hERG closed state with $Q_g = 6e$ as a function of geometrical descriptors, relevant for the O→C transition. The geometrical observables are: displacement and rotation of helices S4 and bending of helices S6 (**a**); rotation of the cytosolic domains with respect to the transmembrane ones (**b**). Pseudo-PMF maps as follows: S4 rotation vs S4 displacement (**c**); S6 bending vs S4 displacement (**d**); S6 bending vs S4 rotation (**e**); PD-CTD rotation vs S6 bending (**f**); PD-CTD rotation vs S4 displacement (**g**); PD-CTD rotation vs S4 rotation (**h**). Dashed lines are a guide to the eye. Bin widths are as follows: S4 displacement: 1.0 Å; S4 rotation: 2°; S6 bending: 1°; PD-CTD rot: 1°. Free energies were expressed in kcal/mol.

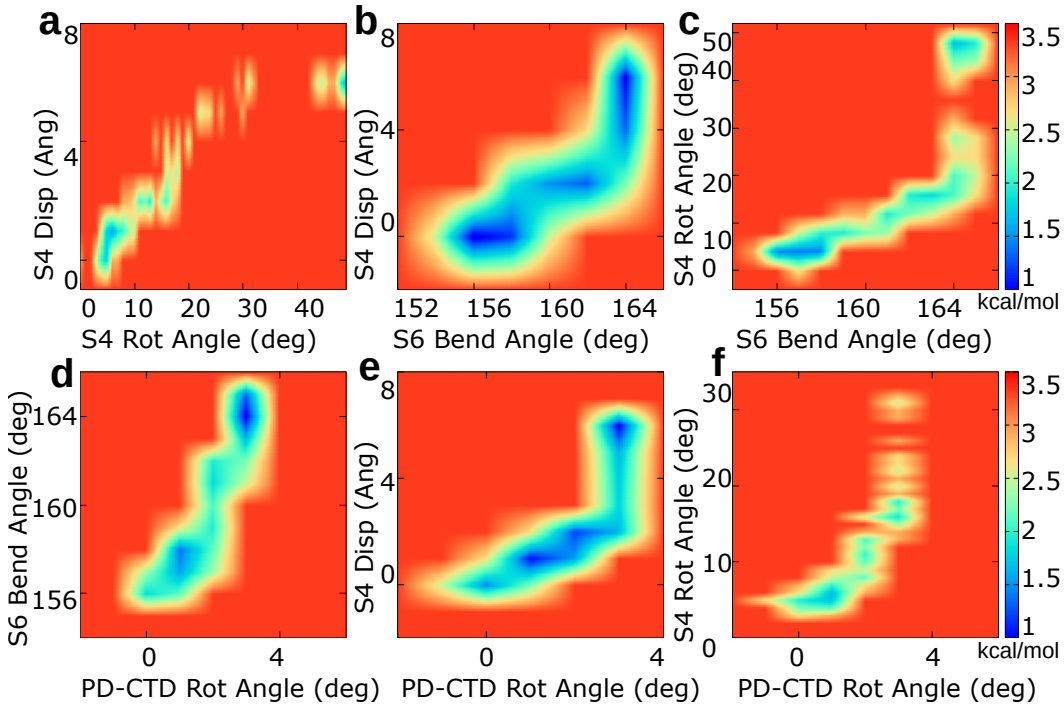

Figure 3.20. Pseudo-potential of Mean Force for hERG closed state with $Q_g = 4e$ as a function of geometrical descriptors, relevant for the O→C transition. The geometrical observables are: displacement and rotation of helices S4 and bending of helices S6 (**a**); rotation of the cytosolic domains with respect to the transmembrane ones (**b**). Pseudo-PMF maps as follows: S4 rotation vs S4 displacement (**c**); S6 bending vs S4 displacement (**d**); S6 bending vs S4 rotation (**e**); PD-CTD rotation vs S6 bending (**f**); PD-CTD rotation vs S4 displacement (**g**); PD-CTD rotation vs S4 rotation (**h**). Dashed lines are a guide to the eye. Bin widths are as follows: S4 displacement: 1.0 Å; S4 rotation: 2°; S6 bending: 1°; PD-CTD rot: 1°. Free energies were expressed in kcal/mol.

Chapter 4

Discussion

The main object of this thesis was to characterize the gating paths of the hERG channel. To achieve this goal, a combined simulations/network theoretical approach was used. Before focusing on the elusive mechanism of hERG, we applied the network analysis on the $K_v1.2$ channel, a Shaker-like channel that has been extensively characterized by experimental works. Here, the analysis allowed us to identify two routes of motion propagation that occur during the inactivation. In particular, our results revealed that the constriction of the SF is coupled to the VSD displacement i) through helix S5 and the P-Loop and ii) through a direct connection with the PD. In the first path, the inactivation starts from helix S4, which is the only part of the channel that responds to changes in the membrane potential. From here, the motion propagates to helix S5 of the neighbouring subunit using two bridges in the middle helix, corresponding to residues V301 and I304 respectively. By mutating residues on the top of the helix we noticed an impairment of inactivation, in agreement with the experimental results obtained in Shaker channels [203, 13]. It is noteworthy that this path encompasses residues L293 and F302 whose mutations into histidine and leucine, respectively, are known to modify the inactivation of $K_v1.2$ leading to epileptic encephalopathy [129, 143]. Moreover, a second communication path was identified coupling the SF to the PD excluding the VSD. In this case the starting point of the motion propagation is represented by the bending region on helix S6 whose movements, after the channel opening, are transferred to Y377 on the SF through the contact between I402 and T373. Interestingly, residue P405 lays on this path and it is correlated to slight changes in the inactivation if mutated into a leucine: similar to L293H and F302L, mutation P405L has been shown to induce epilepsy [182]. Finally, in order to support our computational results, we mutated some residues implicated in the paths whose effects have been demonstrated to modify the inactivation in Shaker channels. The computed changes in the path lengths account for a delayed inactivation in the majority of cases while an acceleration occurs for W366F, see Tab. 3.2; these results yield microscopic insights into experimental results [203, 146, 44, 42, 13], in particular on the allosteric mechanism of inactivation. The good agreement between our computational results and the rich body of experimental data on $K_v1.2$ available in the literature [203, 146, 44, 42, 13] represents a strong validation of our computational protocol in view of the application to the study of hERG about which experimental data were more scarce.

Once the theoretical procedure was set, we focused on the hERG channel. The first challenge in this investigation was the lack of an experimental structure of the closed state. A homology model based on a template with high sequence identity (EAG1, [199]) was built and the S4 helix from the experimental conformation was subsequently pulled down by Steered MD simulations to reach the closed conformation. Using this approach, three systems were generated with gating charge $Q_g = 4e$, $6e$, and $8e$ that differ in the number of S4 basic residues displaced below the GCTC. This choice was motivated by the uncertainty of the experimental value of the gating charge. Indeed, as already discussed, the value $Q_g = 6.4e$ deriving from the limiting slope value is likely an underestimate of the true value and even if an empirical correction yields a more likely value $Q_g = 8e$, we considered more prudent to explore multiple gating scenarios. As a matter of fact, the analysis of gating paths revealed communication to be more efficient in the system with gating charge $Q_g = 8e$ than in the system with gating charge $Q_g = 6e$. Our simulations thus, are in agreement with the assumption that the limiting slope method underestimates the gating charge by 20% [207, 170, 204]. However, an ultimate answer on the conformation of the closed state of hERG will have to wait until an experimental structure (or structures) is resolved. In particular, consensus has not been reached concerning even the number of open and closed states. Experimental evidence seems to suggest that a series of non-permeant structures exists, see, e.g., Liu et al [117] and Wang et al [194]. These authors, performing tail current analysis, were able to study the time course of hERG activation excluding the complicating effect of fast inactivation. A substantial sigmoidal deviation from single-exponential activation was reported, which suggests the existence of multiple closed states. They also showed a voltage-independent step preceding activation which is a unique feature among potassium channels. Indeed, the study of deactivation tail currents also suggested that the open state may act as an aggregate conducting state, i.e., an ensemble of inter-converting conformations. Despite this evidence from electrophysiology and kinetic modelling studies [145], the structural differences between these multiple open and closed states remain elusive, calling for more experimental and computational studies.

Aside for the intriguing issue of the coupling between pore domains and transmembrane domains, the activation/deactivation mechanisms of hERG, like that of all non-domain-swapped potassium channels, remained to date elusive. In domain-swapped channels the long helical L45 linker acts as a mechanical lever pushing onto the neighbouring S6 helix and thus closing the pore. In hERG, however, the L45 loop is too short to exert a force and the experiments on split channels show that mutants with an interrupted L45 have nearly normal activation and deactivation. Our contact analysis suggested two possible mechanisms of activation: in the inter-subunit mechanism loop L45 of subunit n pushes onto the C-Linker of subunit $n+1$ causing a straightening of helix S6 and closure of the pore. Conversely, in the intra-subunit mechanism, loop L45 and helix S4 push onto helix S5 that transmits the pressure across its extensive interface with helix S6. The inter-subunit mechanism corresponds to the experimentally observed mode of action of KAT1 channel from Arabidopsis thaliana [39]. This kind of mechanism was also proposed for EAG1 channel [199]; the authors hypothesized that the downward displacement of helix S4 during hyperpolarization could play a role similar to the binding of

calmodulin which was found to induce the rotation of the C-Linker. On the other hand, the hypothetical intra-subunit mechanism of activation was supported by experiments on split channels [47], showing that a covalent connection between VSD and PD is not necessary for the electromechanical coupling that can instead rely on the extensive network of anti-parallel non-covalent interactions between helices S5 and S6 and on the contacts established by the intracellular end of S4 and S5.

Network theoretical techniques allowed us to validate the hypothetical mechanisms by quantitatively assessing all possible communication paths between helices S4 and S6. The choice to predict the activation path on the closed state of hERG relies on a large body of experimental evidence suggesting that the open state is intrinsically more stable than the closed state [1, 62, 77, 190]. It has been shown that the VSD must exert work to close the pore [190, 106, 37, 38] and when no electric field is applied the channel "falls" into the open state [144]. These results suggest that the communication paths for activation are not present in the open state, and they gradually build as the channel approaches the closed state. Determining the weights of the protein network from simulations of the closed state therefore seems the best strategy to capture the feature of a fully developed communication network. The analysis revealed two families of activation paths with the residues characterized by the highest value of the centrality index and the betweenness (Table 3.4). The first essentially corresponds to the hypothetical intra-subunit mechanism and involves helices routes S4→L45→S5→S6 and S4→L45→S6. The second family, S4→S1→S5→S6, is similar to the noncanonical path identified in Ref. [60] in their study of the domain-swapped $K_v1.2/2.1$ chimera. The latter is also reminiscent of the noncanonical path recently discovered by Carvalho-de Souza and Bezanilla [28] in the Shaker-like channel $K_v1.2$ and it explains the seamless function of the channel without a covalent interaction between the voltage sensor and the pore gate [47]. The analysis also highlighted an asymmetry between the routes originating from the opposite ends of loop L45 with the paths starting from the S5 side being significantly shorter. This asymmetry was confirmed by simulations of the C state of split channels with a cut in the S4-S5 linker. When the interruption was introduced after G546 (S5 end) paths similar to those of the wild type were obtained. However, when the cut was placed before D540 (S4 end), no communication path could be found. Surprisingly, also the upper path was indirectly affected by the D540 cut because of the increased separation of helices S4-S1 and S1-S5. These results are consistent with experiments on split channels [47], which showed an increasing difficulty to reach the closed state as the split point was moved closer to the S4 end. Based on the simulations, these results can be interpreted as a greater impairment of both communication paths when the cut point is close to the S4 end.

On the other hand, the network weights for the computation of the inactivation paths were derived from equilibrium simulations of the open state because the structure of hERG inactivated state is currently rather elusive. A recent computational work [112] has suggested a mechanism of constriction of the SF as the basis of the C-type inactivation. In this view, we tried to reproduce the proposed inactivated state *via* MD simulations. As described in the Results, the inactivated state simulated by Li et al. [112] was not obtained by our simulations. It is true that the systems were reproduced under the same conditions but, on the other hand, we need to precise that our simulations were shorter than those shown in Li et al. [112]. However, it

is reasonable to believe that our results are reliable since the constriction events reported in that paper were observed in the first nanoseconds of the simulations that correspond to our simulation time. Anyway, a very similar constricted state was obtained only when the system was simulated with CHARMM force field and initialized without ions inside the SF. This suggests that the starting configuration of the system associated with the specific force field can represent a bias for this result. Indeed, there are previous works showing that the force field is an important determinant of little structural modifications on proteins, for example as occurred in the inactivation. Precisely, it has been shown that in KcsA, the CHARMM force field favors a fast collapse of the SF toward an occluded state when it has no ions inside. On the other hand, using AMBER no major deviations from the experimental structure are recorded [65]. Moreover, it has been observed that the initial conditions influence the stability of the selectivity filter. In TRAAK channels, when the 2 K^+ configuration is chosen to start with, the SF undergoes a constriction only with the CHARMM force field. Then, the conduction is virtually suppressed if the starting configuration is with 2 K+ with a water molecule between them [141]. This is a clear indication that AMBER and CHARMM force fields behave differently, highlighting an incipient instability of the SF when the CHARMM force field is considered. For this reason, since an experimental validation of this constricted model is still missing and the structure of the inactivated state may be very similar to that of the open state [195], we thought that using the open state to predict the inactivation path was the safest approach. The basis of this choice is that the open state is the only structure that has been experimentally solved [195] and other structures associated with a very elusive state such as the inactivated state are speculative. Here, we identified a kinematic chain of residues that electromechanically mediates the movements of VSD and the constriction of the SF following the S4→S1→S5→P-Loop→SF route relevant for the C-type inactivation. First of all, it is interesting to note that this inactivation path is very similar to the one we identified in $K_v1.2$. This suggests that, despite different molecular architectures, domain-swapped and non-domain-swapped potassium channels make use of similar inactivation routes, exploiting sequences of highly conserved residues optimized by evolution.

The importance of residues in the electromechanical activation and inactivation couplings was quantified computing the Centrality Index (CI) and the betweenness (B) centrality of each residue. We showed that residues on L45 involved in the S4→L45→S5→S6 route have high CI and B values. This result confirms the experimental evidence that mutations on the loop L45 impair the gating of hERG [163, 188, 26] and suggests that it is crucial in the VSD-PD coupling not only for domain-swapped channels but also for non-domain-swapped channels such as hERG. More interestingly, we identified residues on helix S1 to play a key role in both activation and inactivation. We demonstrated the presence of an alternative path that excludes the loop L45 and that resembles the noncanonical path found firstly in the Shaker-like channels [60, 28, 13]. These results agree with previous studies where it has been shown that mutations impairing the gating mechanism were mapped to helices S1 [152], S4 [130] and S5 [61] confirming the role of the S4/S1 and S1/S5 interfaces in the VSD-PD coupling also in non-domain-swapped channels.

The analysis of pseudo-PMFs revealed that hERG dynamics can be described in terms of a few geometric variables. This approach, however, also raised a number of

issues that will require extensive computational and experimental testing. A clue on the role of the rotation of cytosolic domains may be provided by the plot PD-CTD rotation vs S6 bending (Figure 3.18f). The alignment of this graph along the diagonal suggests a possible auxiliary mechanism whereby the rotation of cytosolic domains is propagated to the C-Linker and from here to S6 helices. This trend, however, is only partially followed by the systems with gating charge $6e$ (first part of the trajectory; Figure 3.19d) and with gating charge $4e$ (last part of the trajectory; Figure 3.20d), so that more experimental validations are required. PMF results, for instance, pose the following question: what is the need for a long roto-translation of helix S4 if the extension of helix S6 is rapidly concluded? The contact analysis suggests that the motion of S4 is finalized to the establishment of contacts between loop L45 of subunit n and the C-Linker of subunit $n + 1$ (Figure 3.8b). This leads to the tempting speculation of a coupling between the motion of helix S4 and the rotation of the cytosolic domains with respect to the transmembrane ones. This hypothesis is tested analysing the pseudo-PMFs PD-CTD rotation vs S4 displacement and PD-CTD rotation vs S4 rotation: Figure 3.18g-h and Figures 3.19e-f and 3.20e-f clearly show that the rotation of the cytoplasmic domains ended before the motion of helix S4 was completed. As a result, it cannot be the motion of helix S4 that causes the rotation of the cytosolic domains that still remains unclear. Concluding, the work excludes a causal role of S4 motion, so that the binding of the intrinsic ligand might play a role, possibly acting as a secondary voltage sensor [40]; at this stage, however, other factors cannot be ruled out.

Finally, we collaborated with the experimental group led by Prof. Francisco Bezanilla from the University of Chicago. The electrophysiological analysis of mutants laying on the computationally predicted activation and inactivation paths provided a sound experimental validation of our simulation/network-theoretical approach. Indeed, the scatter plots of Figure 3.15 show that the betweenness of the wild type systems captures all the relevant information needed to guide experimental mutagenesis. Residues with high betweenness centrality in simulations affect prominently the gating mechanism also in experiments. Indeed, the greater the betweenness centrality, the higher the absolute values of $\Delta\Delta$G (measured experimentally) for activation and inactivation.

Chapter 5

Conclusions

In this thesis, we have used MD simulations combined with a network theoretical approach to reveal the hereby unknown gating mechanism of hERG, a cardiac ion channel which plays a crucial role in the heart mechanics. Alterations in the opening of the channel are linked to serious cardiac diseases, including the Long QT syndrome type 2 (LQTS2) that affects an estimated 1 in 5,000-10,000 people worldwide and may lead to sudden cardiac death [166]. The disease can also be induced by the unspecific interactions between hERG and a wide range of drugs such as anti-arrhythmics, antibiotics, and antihistamines [158]. The severity of these conditions is such that regulatory agencies prescribe the testing of all new drugs for hERG block. For this reason, the FDA and a consortium of other regulatory agencies have promoted the Comprehensive in Vitro Proarrhythmia Assays (CiPA) [32, 41], a large scale screening program to test candidate new drugs for cross-reactivity and block of hERG channel where *in silico* steps are included with the objective of expediting and making cost-effective the screening of new drugs.

In this context, we microscopically identified the electromechanical paths between the sensor (Voltage Sensor Domain) and the actuator (Pore Domain) of the channel as the chain of residues that with their interactions transmit the motion from the sensor to the pore. For the first time, we shared with the community three different models of the closed state of the channel, whose experimental structure has not been solved yet. Moreover, on the methodological side, mutagenesis experiments by the group of Prof. Francisco Bezanilla from the University of Chicago guided by insights from our simulations on the wild type, suggested a time and cost-effective approach to analyze gating mechanisms in ion channels.

To sum up, our results shed new light on the elusive gating mechanism of the hERG channel which might serve as the basis for studying the origin of LQTS2. They clarify the gating mechanism of the non-domain-swapped family of channels characterized by a close contact between the sensor and the actuator of the same subunit. The identified paths resemble the gating paths previously identified in other potassium channels [12, 60, 28, 13]. Moreover, our work extends the scope of CiPA, by providing molecular-level computational tools [161] useful for fast and inexpensive screening of new drugs [31]. Similar to the current CiPA approach, we also applied mathematical modeling but we moved from the cellular to the molecular level with the possibility not only to identify molecules with undesired side effects but also

to rationally design specific and safe drugs targeting a channel whose impairment might have a lethal effect.

Chapter 6

Future directions

Due to the severity of the acquired LQTS2 induced by the blockage of hERG by unspecific drugs, we are currently focusing on the interactions between the channel and the RPR260243 molecule. Precisely, RPR260243 is a recently discovered molecule that activates hERG increasing its probability to be in the open state. For this reason, it is considered as a candidate to treat LQTS2 in the future. Mutagenesis studies showed that mutating residues L553, F557, V659, N658, and I662 reduced the gating effects of RPR260243 while mutating V549, L550 and L666 prevented the slowing of deactivation [150]. This evidence suggests a putative binding site for RPR260243 at the VSD/PD interface, between helices S5 and S6. However, more studies need to be done to confirm this prediction. Interestingly, many of these residues lay on the canonical activation path and have high betweenness centrality values (as shown in Table 3.4). In this context, in collaboration with the group led by Prof. Matteo Masetti from the University of Bologna, we are studying the binding mode of RPR260243 with a combination of docking methods and molecular dynamics simulations.

To date, the molecular determinants of the high tropism of hERG for drugs raised a lot of interest. However, this research line opens new questions that need to be solved. The main one is connected to the lack of structural information on the hERG inactivation since most drugs preferentially interact with the inactivated state. This structure has not been solved. Recent studies suggest that the hERG inactivation is similar to that of the Shaker-family channels where there is a constriction of the Selectivity Filter that stops the ion flow [112]. On the other hand, it has been proposed that hERG can be characterized by a different mechanism where the potassium flow is blocked by the increase of sodium permeability [66]. It is possible that these mechanisms can be part of the same process but more studies are needed. In our simulations, we were not able to reproduce the constriction of the Selectivity Filter but we noticed that in the extracellular portion it became wider than the wild type. These observations allow to speculate on a new mechanism of inactivation that, however, will need further experimental and computational validation.

Chapter 7

Appendix

7.1 Role of the d_{cut} parameter in the network analysis

In the network analysis the critical parameter is represented by d_{cut}, the communication distance cutoff below which two nodes of the protein graph are connected by an arc. It differs from the physical distance between two residues (used in the contact map analysis) that comes into play only in a second stage, when the communication paths computed through the network approach must be validated. Indeed, it may happen that two residues lie next to each other on a path (because their motion is highly correlated) but they are physically very far from each other, so that motion cannot be propagated from a residue to the other. The distance between two residues therefore determines whether a path is accepted or discarded but has no influence on the length and route followed by the path. These features instead depend on the d_{cut} parameter that is related to the minimal correlation coefficient required for two residues to be considered linked by an edge in the protein graph: $d_{cut} = -log|C|_{cut}$. In the network analysis we used d_{cut}=0.40 that corresponds to a minimum correlation $|C|_{cut}$=0.67. In order to show the role of the d_{cut} parameter, we repeated the path analysis with two values higher than 0.40 and two values smaller than 0.40 (d_{cut} = 0.16, 0.28, 0.69, 1.20).

As d_{cut} decreases two residues will be connected by an edge only if their correlation is very high. As a result the number of arcs of the network decreases. Consequently the number of paths connecting a given source node and a given target node is also expected to decrease. Consistently with this scenario when d_{cut}=0.16 no path can be detected in any of the closed structures we produced. If d_{cut} is increased to 0.28 no path can be observed in 3 out of 4 subunits of the systems with gating charge 6e and 8e while in the fourth subunit we observe a path that is much longer and qualitatively different with respect to the path computed with d_{cut}=0.4. Interestingly, in the system with gating charge 4e the paths computed with d_{cut}=0.28 are qualitatively similar and of comparable length as compared to the paths computed with d_{cut}=0.4. It is thus likely that the edges lying along the minimal paths computed with d_{cut}=0.4 connected pairs of residues with such a highly correlated motion that they were not removed when d_{cut} was decreased from 0.40 to 0.28.

Conversely as d_{cut} increases, a smaller and smaller correlation is required for two residues to be linked by an edge in the graph. As a result, the number of edges

of the network increases and also the number of paths connecting given end states is expected to grow. However, the minimal paths between a source and a target node tend to proceed along the shortest edges, i.e., those connecting the pairs of residues with the most correlated motion. As a result, minimal paths should to some extent be retained even in the face of an increase of d_{cut}, even if the presence of a greater number of edges allows shortcuts that decrease the length of the path. This is exactly what can be observed with d_{cut}=0.69 and d_{cut}=1.20: in most cases the minimal paths are qualitatively similar and their lengths are comparable or slightly shorter than those of the paths computed with d_{cut}=0.40. A few paths however, are qualitatively different from those computed with d_{cut}=0.40.

In hindsight, this analysis shows that the value d_{cut}=0.40 used in the article corresponds to the maximum value of correlation compatible with the establishment of efficient communication paths. The paths computed with this value of d_{cut} are qualitatively retained up to d_{cut}=1.20 even if some alternative route starts to appear. The number of these alternative routes is expected to increase at even higher values of d_{cut}. The reliability of the results attained using a graph with edges connecting even weakly correlated pairs of residues, however, is highly questionable.

Bibliography

[1] C. Alonso-Ron, P. De la Pena, P. Miranda, P. Domínguez, and F. Barros. Thermodynamic and kinetic properties of amino-terminal and S4-S5 loop HERG channel mutants under steady-state conditions. *Biophysical journal*, 94(10):3893–3911, 2008.

[2] C. L. Anderson, B. P. Delisle, B. D. Anson, J. A. Kilby, M. L. Will, D. J. Tester, Q. Gong, Z. Zhou, M. J. Ackerman, and C. T. January. Most LQT2 mutations reduce Kv11. 1 (hERG) current by a class 2 (trafficking-deficient) mechanism. *Circulation*, 113(3):365–373, 2006.

[3] C. L. Anderson, C. E. Kuzmicki, R. R. Childs, C. J. Hintz, B. P. Delisle, and C. T. January. Large-scale mutational analysis of Kv11. 1 reveals molecular insights into type 2 long QT syndrome. *Nature communications*, 5(1):1–13, 2014.

[4] J. Åqvist and V. Luzhkov. Ion permeation mechanism of the potassium channel. *Nature*, 404(6780):881–884, 2000.

[5] P. Aryal, M. S. Sansom, and S. J. Tucker. Hydrophobic gating in ion channels. *Journal of molecular biology*, 427(1):121–130, 2015.

[6] T. Asai, N. Adachi, T. Moriya, H. Oki, T. Maru, M. Kawasaki, K. Suzuki, S. Chen, R. Ishii, K. Yonemori, et al. Cryo-EM structure of K+-bound hERG channel complexed with the blocker astemizole. *Structure*, 29(3):203–212, 2021.

[7] F. M. Ashcroft. *Ion channels and disease*. Academic press, 1999.

[8] N. A. Baker, D. Sept, S. Joseph, M. J. Holst, and J. A. McCammon. Electrostatics of nanosystems: application to microtubules and the ribosome. *Proceedings of the National Academy of Sciences*, 98(18):10037–10041, 2001.

[9] D. Baracaldo-Santamaría, K. Llinás-Caballero, J. M. Corso-Ramirez, C. M. Restrepo, C. A. Dominguez-Dominguez, D. J. Fonseca-Mendoza, and C. A. Calderon-Ospina. Genetic and molecular aspects of drug-induced QT interval prolongation. *International journal of molecular sciences*, 22(15):8090, 2021.

[10] A. F. Barber, V. Carnevale, S. Raju, C. Amaral, W. Treptow, and M. L. Klein. Hinge-bending motions in the pore domain of a bacterial voltage-gated sodium channel. *Biochimica et Biophysica Acta (BBA)-Biomembranes*, 1818(9):2120–2125, 2012.

[11] F. Barros, P. de la Peña, P. Domínguez, L. M. Sierra, and L. A. Pardo. The EAG voltage-dependent K+ channel subfamily: similarities and differences in structural organization and gating. *Frontiers in pharmacology*, 11:411, 2020.

[12] F. Barros, L. A. Pardo, P. Domínguez, L. M. Sierra, and P. De la Peña. New structures and gating of voltage-dependent potassium (Kv) channels and their relatives: a multi-domain and dynamic question. *International journal of molecular sciences*, 20(2):248, 2019.

[13] C. A. Bassetto, J. L. Carvalho-de Souza, and F. Bezanilla. Molecular basis for functional connectivity between the voltage sensor and the selectivity filter gate in Shaker K+ channels. *Elife*, 10, 2021.

[14] O. Beckstein, P. C. Biggin, P. Bond, J. N. Bright, C. Domene, A. Grottesi, J. Holyoake, and M. S. Sansom. Ion channel gating: insights via molecular simulations. *FEBS letters*, 555(1):85–90, 2003.

[15] D. Beglov and B. Roux. Finite representation of an infinite bulk system: solvent boundary potential for computer simulations. *The Journal of chemical physics*, 100(12):9050–9063, 1994.

[16] E. E. Benarroch. Potassium channels: brief overview and implications in epilepsy. *Neurology*, 72(7):664–669, 2009.

[17] H. J. Berendsen, J. v. Postma, W. F. Van Gunsteren, A. DiNola, and J. R. Haak. Molecular dynamics with coupling to an external bath. *The Journal of chemical physics*, 81(8):3684–3690, 1984.

[18] R. B. Best, X. Zhu, J. Shim, P. E. Lopes, J. Mittal, M. Feig, and A. D. MacKerell Jr. Optimization of the additive CHARMM all-atom protein force field targeting improved sampling of the backbone ϕ, ψ and side-chain $\chi 1$ and $\chi 2$ dihedral angles. *Journal of chemical theory and computation*, 8(9):3257–3273, 2012.

[19] F. Bezanilla. The voltage sensor in voltage-dependent ion channels. *Physiological reviews*, 80(2):555–592, 2000.

[20] M. Bohnen, G. Peng, S. Robey, C. Terrenoire, V. Iyer, K. Sampson, and R. Kass. Molecular pathophysiology of congenital long QT syndrome. *Physiological reviews*, 97(1):89–134, 2017.

[21] J. A. Bondy, U. S. R. Murty, et al. *Graph theory with applications*, volume 290. Macmillan London, 1976.

[22] M. R. Bowlby, R. Peri, H. Zhang, and J. Dunlop. hERG (KCNH2 or Kv11. 1) K+ channels: screening for cardiac arrhythmia risk. *Current drug metabolism*, 9(9):965–970, 2008.

[23] U. Brandes. A faster algorithm for betweenness centrality. *Journal of mathematical sociology*, 25(2):163–177, 2001.

[24] T. I. Brelidze, A. E. Carlson, B. Sankaran, and W. N. Zagotta. Structure of the carboxy-terminal region of a KCNH channel. *Nature*, 481(7382):530–533, 2012.

[25] B. R. Brooks, C. L. Brooks III, A. D. Mackerell Jr, L. Nilsson, R. J. Petrella, B. Roux, Y. Won, G. Archontis, C. Bartels, S. Boresch, et al. CHARMM: the biomolecular simulation program. *Journal of computational chemistry*, 30(10):1545–1614, 2009.

[26] A. Butler, M. V. Helliwell, Y. Zhang, J. C. Hancox, and C. E. Dempsey. An Update on the Structure of hERG. *Frontiers in pharmacology*, 10:1572, 2020.

[27] J. H. M. Cabral, A. Lee, S. L. Cohen, B. T. Chait, M. Li, and R. Mackinnon. Crystal structure and functional analysis of the HERG potassium channel N terminus: a eukaryotic PAS domain. *Cell*, 95(5):649–655, 1998.

[28] J. L. Carvalho-de Souza and F. Bezanilla. Noncanonical mechanism of voltage sensor coupling to pore revealed by tandem dimers of Shaker. *Nature communications*, 10(1):1–12, 2019.

[29] D. A. Case, T. E. Cheatham III, T. Darden, H. Gohlke, R. Luo, K. M. Merz Jr, A. Onufriev, C. Simmerling, B. Wang, and R. J. Woods. The Amber biomolecular simulation programs. *Journal of computational chemistry*, 26(16):1668–1688, 2005.

[30] O. Casis, S.-P. Olesen, and M. C. Sanguinetti. Mechanism of action of a novel human ether-a-go-go-related gene channel activator. *Molecular pharmacology*, 69(2):658–665, 2006.

[31] A. Cavalli, R. Buonfiglio, C. Ianni, M. Masetti, L. Ceccarini, R. Caves, M. W. Chang, J. S. Mitcheson, M. Roberti, and M. Recanatini. Computational design and discovery of "minimally structured" hERG blockers. *Journal of medicinal chemistry*, 55(8):4010–4014, 2012.

[32] I. Cavero, J.-M. Guillon, V. Ballet, M. Clements, J.-F. Gerbeau, and H. Holzgrefe. Comprehensive in vitro Proarrhythmia Assay (CiPA): Pending issues for successful validation and implementation. *Journal of pharmacological and toxicological methods*, 81:21–36, 2016.

[33] L. Ceccarini, M. Masetti, A. Cavalli, and M. Recanatini. Ion conduction through the hERG potassium channel. *PLoS One*, 7(11):e49017, 2012.

[34] X. Chen, Q. Wang, F. Ni, and J. Ma. Structure of the full-length Shaker potassium channel Kv1. 2 by normal-mode-based X-ray crystallographic refinement. *Proceedings of the National Academy of Sciences*, 107(25):11352–11357, 2010.

[35] Y. M. Cheng, C. M. Hull, C. M. Niven, J. Qi, C. R. Allard, and T. W. Claydon. Functional interactions of voltage sensor charges with an S2 hydrophobic plug in hERG channels. *Journal of General Physiology*, 142(3):289–303, 2013.

[36] S.-H. Choi, T.-J. Shin, S.-H. Hwang, B.-H. Lee, J. Kang, H.-J. Kim, S.-H. Jo, H. Choe, and S.-Y. Nah. Ginsenoside Rg3 decelerates hERG K+ channel deactivation through Ser631 residue interaction. *European journal of pharmacology*, 663(1-3):59–67, 2011.

[37] F. S. Choveau, F. Abderemane-Ali, F. C. Coyan, Z. Es-Salah-Lamoureux, I. Baro, and G. Loussouarn. Opposite effects of the S4–S5 linker and PIP2 on voltage-gated channel function: KCNQ1/KCNE1 and other channels. *Frontiers in Pharmacology*, 3:125, 2012.

[38] S. Chowdhury and B. Chanda. Thermodynamics of electromechanical coupling in voltage-gated ion channels. *Journal of General Physiology*, 140(6):613–623, 2012.

[39] M. D. Clark, G. F. Contreras, R. Shen, and E. Perozo. Electromechanical coupling in the hyperpolarization-activated K+ channel KAT1. *Nature*, 583(7814):145–149, 2020.

[40] S. J. Codding and M. C. Trudeau. The hERG potassium channel intrinsic ligand regulates N-and C-terminal interactions and channel closure. *Journal of General Physiology*, 151(4):478–488, 2019.

[41] T. Colatsky, B. Fermini, G. Gintant, J. B. Pierson, P. Sager, Y. Sekino, D. G. Strauss, and N. Stockbridge. The comprehensive in vitro proarrhythmia assay (CiPA) initiative—update on progress. *Journal of pharmacological and toxicological methods*, 81:15–20, 2016.

[42] J. F. Cordero-Morales, V. Jogini, S. Chakrapani, and E. Perozo. A multipoint hydrogen-bond network underlying KcsA C-type inactivation. *Biophysical journal*, 100(10):2387–2393, 2011.

[43] D. S. Corti. Isothermal-isobaric ensemble for small systems. *Physical Review E*, 64(1):016128, 2001.

[44] L. G. Cuello, V. Jogini, D. M. Cortes, and E. Perozo. Structural mechanism of C-type inactivation in K+ channels. *Nature*, 466(7303):203–208, 2010.

[45] J. Cui, H. Yang, and U. S. Lee. Molecular mechanisms of BK channel activation. *Cellular and Molecular Life Sciences*, 66(5):852–875, 2009.

[46] M. E. Curran, I. Splawski, K. W. Timothy, G. M. Vincen, E. D. Green, and M. T. Keating. A molecular basis for cardiac arrhythmia: hERG mutations cause long QT syndrome. *Cell*, 80(5):795–803, 1995.

[47] P. de la Peña, P. Domínguez, and F. Barros. Gating mechanism of Kv11. 1 (hERG) K+ channels without covalent connection between voltage sensor and pore domains. *Pflügers Archiv-European Journal of Physiology*, 470(3):517–536, 2018.

[48] D. del Camino and G. Yellen. Tight steric closure at the intracellular activation gate of a voltage-gated K+ channel. *Neuron*, 32(4):649–656, 2001.

[49] L. Delemotte, M. A. Kasimova, M. L. Klein, M. Tarek, and V. Carnevale. Free-energy landscape of ion-channel voltage-sensor–domain activation. *Proceedings of the National Academy of Sciences*, 112(1):124–129, 2015.

[50] C. J. Dickson, B. D. Madej, Å. A. Skjevik, R. M. Betz, K. Teigen, I. R. Gould, and R. C. Walker. Lipid14: the amber lipid force field. *Journal of chemical theory and computation*, 10(2):865–879, 2014.

[51] E. W. Dijkstra et al. A note on two problems in connexion with graphs. *Numerische mathematik*, 1(1):269–271, 1959.

[52] B. T. Donovan, D. Bandyopadhyay, C. Duraiswami, C. J. Nixon, C. Y. Townsend, and S. F. Martens. Discovery and electrophysiological characterization of SKF-32802: a novel hERG agonist found through a large-scale structural similarity search. *European Journal of Pharmacology*, 818:306–327, 2018.

[53] D. A. Doyle, J. M. Cabral, R. A. Pfuetzner, A. Kuo, J. M. Gulbis, S. L. Cohen, B. T. Chait, and R. MacKinnon. The structure of the potassium channel: molecular basis of K+ conduction and selectivity. *science*, 280(5360):69–77, 1998.

[54] R. O. Dror, R. M. Dirks, J. Grossman, H. Xu, and D. E. Shaw. Biomolecular simulation: a computational microscope for molecular biology. *Annual review of biophysics*, 41:429–452, 2012.

[55] F. Ercolessi. A molecular dynamics primer. *Spring college in computational physics, ICTP, Trieste*, 19, 1997.

[56] N. Eswar, B. Webb, M. A. Marti-Renom, M. Madhusudhan, D. Eramian, M.-y. Shen, U. Pieper, and A. Sali. Comparative protein structure modeling using Modeller. *Current protocols in bioinformatics*, 15(1):5–6, 2006.

[57] A. Fabiato and F. Fabiato. Calcium and cardiac excitation-contraction coupling. *Annual review of physiology*, 41(1):473–484, 1979.

[58] S. E. Feller, Y. Zhang, R. W. Pastor, and B. R. Brooks. Constant pressure molecular dynamics simulation: the Langevin piston method. *The Journal of chemical physics*, 103(11):4613–4621, 1995.

[59] D. Fernandez, A. Ghanta, G. W. Kauffman, and M. C. Sanguinetti. Physicochemical features of the HERG channel drug binding site. *Journal of Biological Chemistry*, 279(11):10120–10127, 2004.

[60] A. I. Fernández-Mariño, T. J. Harpole, K. Oelstrom, L. Delemotte, and B. Chanda. Gating interaction maps reveal a noncanonical electromechanical coupling mode in the Shaker K+ channel. *Nature structural & molecular biology*, 25(4):320–326, 2018.

[61] T. Ferrer, J. F. Cordero-Morales, M. Arias, E. Ficker, D. Medovoy, E. Perozo, and M. Tristani-Firouzi. Molecular coupling in the human ether-a-go-go-related

gene-1 (hERG1) K+ channel inactivation pathway. *Journal of Biological Chemistry*, 286(45):39091–39099, 2011.

[62] T. Ferrer, J. Rupp, D. R. Piper, and M. Tristani-Firouzi. The S4-S5 linker directly couples voltage sensor movement to the activation gate in the human ether-a-go-go-related gene (hERG) K+ channel. *Journal of Biological Chemistry*, 281(18):12858–12864, 2006.

[63] E. Ficker, W. Jarolimek, J. Kiehn, A. Baumann, and A. M. Brown. Molecular determinants of dofetilide block of HERG K+ channels. *Circulation research*, 82(3):386–395, 1998.

[64] D. Frenkel and B. Smit. *Understanding molecular simulation: from algorithms to applications*, volume 1. Elsevier, 2001.

[65] S. Furini and C. Domene. Critical assessment of common force fields for molecular dynamics simulations of potassium channels. *Journal of Chemical Theory and Computation*, 16(11):7148–7159, 2020.

[66] H. Gang and S. Zhang. Na+ permeation and block of hERG potassium channels. *The Journal of general physiology*, 128(1):55–71, 2006.

[67] V. Garg, A. Stary-Weinzinger, F. Sachse, and M. C. Sanguinetti. Molecular determinants for activation of human ether-à-go-go-related gene 1 potassium channels by 3-nitro-n-(4-phenoxyphenyl) benzamide. *Molecular Pharmacology*, 80(4):630–637, 2011.

[68] G. Gessner, R. Macianskiene, J. G. Starkus, R. Schönherr, and S. H. Heinemann. The amiodarone derivative KB130015 activates hERG1 potassium channels via a novel mechanism. *European journal of pharmacology*, 632(1-3):52–59, 2010.

[69] A. Giacomello and R. Roth. Bubble formation in nanopores: a matter of hydrophobicity, geometry, and size. *Advances in Physics: X*, 5(1):1817780, 2020.

[70] S. A. Goldstein, D. A. Bayliss, D. Kim, F. Lesage, L. D. Plant, and S. Rajan. International Union of Pharmacology. LV. Nomenclature and molecular relationships of two-P potassium channels. *Pharmacological reviews*, 57(4):527–540, 2005.

[71] M. Grunnet, J. Abbruzzese, F. B. Sachse, and M. C. Sanguinetti. Molecular determinants of human ether-a-go-go-related gene 1 (hERG1) K+ channel activation by NS1643. *Molecular Pharmacology*, 79(1):1–9, 2011.

[72] C. Guardiani, F. Cecconi, L. Chiodo, G. Cottone, P. Malgaretti, L. Maragliano, M. Barabash, G. Camisasca, M. Ceccarelli, B. Corry, et al. Computational methods and theory for ion channel research. *Advances in Physics: X*, 7(1):2080587, 2022.

[73] C. Guardiani, D. Sun, and A. Giacomello. Unveiling the gating mechanism of CRAC channel: a computational study. *Frontiers in molecular biosciences*, page 1205, 2021.

[74] J. Guo and H.-X. Zhou. Protein allostery and conformational dynamics. *Chemical reviews*, 116(11):6503–6515, 2016.

[75] O. Guvench and A. D. MacKerell. Comparison of protein force fields for molecular dynamics simulations. *Molecular modeling of proteins*, pages 63–88, 2008.

[76] A. Hagberg, P. Swart, and D. S Chult. Exploring network structure, dynamics, and function using NetworkX. Technical report, Los Alamos National Lab.(LANL), Los Alamos, NM (United States), 2008.

[77] R. M. Hardman, P. J. Stansfeld, S. Dalibalta, M. J. Sutcliffe, and J. S. Mitcheson. Activation gating of hERG potassium channels: S6 glycines are not required as gating hinges. *Journal of Biological Chemistry*, 282(44):31972–31981, 2007.

[78] H. Hibino, A. Inanobe, K. Furutani, S. Murakami, I. Findlay, and Y. Kurachi. Inwardly rectifying potassium channels: their structure, function, and physiological roles. *Physiological reviews*, 90(1):291–366, 2010.

[79] B. Hille. Ionic channels in excitable membranes. Current problems and biophysical approaches. *Biophysical Journal*, 22(2):283–294, 1978.

[80] R. K. Hite, X. Tao, and R. MacKinnon. Structural basis for gating the high-conductance Ca2+-activated K+ channel. *Nature*, 541(7635):52–57, 2017.

[81] R. K. Hite, P. Yuan, Z. Li, Y. Hsuing, T. Walz, and R. MacKinnon. Cryo-electron microscopy structure of the Slo2. 2 Na+-activated K+ channel. *Nature*, 527(7577):198–203, 2015.

[82] A. L. Hodgkin and R. Keynes. The potassium permeability of a giant nerve fibre. *The Journal of physiology*, 128(1):61, 1955.

[83] A. Hospital, J. R. Goñi, M. Orozco, and J. L. Gelpí. Molecular dynamics simulations: advances and applications. *Advances and applications in bioinformatics and chemistry: AABC*, 8:37, 2015.

[84] S. Izrailev, S. Stepaniants, B. Isralewitz, D. Kosztin, H. Lu, F. Molnar, W. Wriggers, and K. Schulten. Steered molecular dynamics. In *Computational molecular dynamics: challenges, methods, ideas*, pages 39–65. Springer, 1999.

[85] W. Janke. Statistical analysis of simulations: Data correlations and error estimation. *Quantum Simulations of Complex Many-Body Systems: From Theory to Algorithms*, 10:423–445, 2002.

[86] K. Jeevaratnam, K. R. Chadda, C. L.-H. Huang, and A. J. Camm. Cardiac potassium channels: physiological insights for targeted therapy. *Journal of Cardiovascular Pharmacology and Therapeutics*, 23(2):119–129, 2018.

[87] M. Jenke, A. Sánchez, F. Monje, W. Stühmer, R. M. Weseloh, and L. A. Pardo. C-terminal domains implicated in the functional surface expression of potassium channels. *The EMBO Journal*, 22(3):395–403, 2003.

[88] M. Ø. Jensen, V. Jogini, D. W. Borhani, A. E. Leffler, R. O. Dror, and D. E. Shaw. Mechanism of voltage gating in potassium channels. *Science*, 336(6078):229–233, 2012.

[89] Y. Jiang, A. Lee, J. Chen, V. Ruta, M. Cadene, B. T. Chait, and R. MacKinnon. X-ray structure of a voltage-dependent K+ channel. *Nature*, 423(6935):33–41, 2003.

[90] S. Jo, T. Kim, V. G. Iyer, and W. Im. CHARMM-GUI: a web-based graphical user interface for CHARMM. *Journal of computational chemistry*, 29(11):1859–1865, 2008.

[91] S. Jo, J. B. Lim, J. B. Klauda, and W. Im. CHARMM-GUI Membrane Builder for mixed bilayers and its application to yeast membranes. *Biophysical journal*, 97(1):50–58, 2009.

[92] D. K. Jones, F. Liu, N. Dombrowski, S. Joshi, and G. A. Robertson. Dominant negative consequences of a hERG 1b-specific mutation associated with intrauterine fetal death. *Progress in biophysics and molecular biology*, 120(1-3):67–76, 2016.

[93] D. K. Jones, F. Liu, R. Vaidyanathan, L. L. Eckhardt, M. C. Trudeau, and G. A. Robertson. hERG 1b is critical for human cardiac repolarization. *Proceedings of the National Academy of Sciences*, 111(50):18073–18077, 2014.

[94] K. Kamiya, J. S. Mitcheson, K. Yasui, I. Kodama, and M. C. Sanguinetti. Open channel block of HERG K+ channels by vesnarinone. *Molecular pharmacology*, 60(2):244–253, 2001.

[95] K. Kamiya, R. Niwa, J. S. Mitcheson, and M. C. Sanguinetti. Molecular determinants of HERG channel block. *Molecular pharmacology*, 69(5):1709–1716, 2006.

[96] K. Kamiya, R. Niwa, M. Morishima, H. Honjo, and M. C. Sanguinetti. Molecular determinants of hERG channel block by terfenadine and cisapride. *Journal of pharmacological sciences*, 108(3):301–307, 2008.

[97] J. Kang, X.-L. Chen, H. Wang, J. Ji, H. Cheng, J. Incardona, W. Reynolds, F. Viviani, M. Tabart, and D. Rampe. Discovery of a small molecule activator of the human ether-a-go-go-related gene (HERG) cardiac K+ channel. *Molecular Pharmacology*, 67(3):827–836, 2005.

[98] R. Khanna and V. Sahajwalla. Atomistic Simulations of Properties and Phenomena at High Temperatures. In *Treatise on Process Metallurgy*, pages 287–393. Elsevier, 2014.

[99] J.-B. Kim. Channelopathies. *Korean journal of pediatrics*, 57(1):1, 2014.

[100] J. B. Klauda, R. M. Venable, J. A. Freites, J. W. O'Connor, D. J. Tobias, C. Mondragon-Ramirez, I. Vorobyov, A. D. MacKerell Jr, and R. W. Pastor. Update of the CHARMM all-atom additive force field for lipids: validation on six lipid types. *The journal of physical chemistry B*, 114(23):7830–7843, 2010.

[101] W. Kopec, D. A. Köpfer, O. N. Vickery, A. S. Bondarenko, T. L. Jansen, B. L. De Groot, and U. Zachariae. Direct knock-on of desolvated ions governs strict ion selectivity in K+ channels. *Nature chemistry*, 10(8):813–820, 2018.

[102] C. E. Korman and I. D. Mayergoyz. On hysteresis of ion channels. *Mathematical Modelling of Natural Phenomena*, 15:26, 2020.

[103] A. Kraskov, H. Stögbauer, and P. Grassberger. Estimating mutual information. *Physical review E*, 69(6):066138, 2004.

[104] Y. Kubo, J. P. Adelman, D. E. Clapham, L. Y. Jan, A. Karschin, Y. Kurachi, M. Lazdunski, C. G. Nichols, S. Seino, and C. A. Vandenberg. International Union of Pharmacology. LIV. Nomenclature and molecular relationships of inwardly rectifying potassium channels. *Pharmacological reviews*, 57(4):509–526, 2005.

[105] S. Kupershmidt, T. Yang, S. Chanthaphaychith, Z. Wang, J. A. Towbin, and D. M. Roden. Defective human Ether-a-go-go-related gene trafficking linked to an endoplasmic reticulum retention signal in the C terminus. *Journal of Biological Chemistry*, 277(30):27442–27448, 2002.

[106] A. J. Labro and D. J. Snyders. Being flexible: the voltage-controllable activation gate of kv channels. *Frontiers in Pharmacology*, 3:168, 2012.

[107] A. R. Leach and A. R. Leach. *Molecular modelling: principles and applications*. Pearson education, 2001.

[108] C.-H. Lee and R. MacKinnon. Activation mechanism of a human SK-calmodulin channel complex elucidated by cryo-EM structures. *Science*, 360(6388):508–513, 2018.

[109] J. P. Lees-Miller, Y. Duan, G. Q. Teng, and H. J. Duff. Molecular determinant of high-affinity dofetilide binding toHERG1 expressed in Xenopus oocytes: involvement of S6 sites. *Molecular pharmacology*, 57(2):367–374, 2000.

[110] J. P. Lees-Miller, C. Kondo, L. Wang, and H. J. Duff. Electrophysiological characterization of an alternatively processed ERG K+ channel in mouse and human hearts. *Circulation Research*, 81(5):719–726, 1997.

[111] J. Li, J. Ostmeyer, L. G. Cuello, E. Perozo, and B. Roux. Rapid constriction of the selectivity filter underlies C-type inactivation in the KcsA potassium channel. *Journal of General Physiology*, 150(10):1408–1420, 2018.

[112] J. Li, R. Shen, B. Reddy, E. Perozo, and B. Roux. Mechanism of C-type inactivation in the hERG potassium channel. *Science Advances*, 7(5):eabd6203, 2021.

[113] M. Li, X. Zhou, S. Wang, I. Michailidis, Y. Gong, D. Su, H. Li, X. Li, and J. Yang. Structure of a eukaryotic cyclic-nucleotide-gated channel. *Nature*, 542(7639):60–65, 2017.

[114] Q. Li, S. Wanderling, M. Paduch, D. Medovoy, A. Singharoy, R. McGreevy, C. A. Villalba-Galea, R. E. Hulse, B. Roux, K. Schulten, et al. Structural mechanism of voltage-dependent gating in an isolated voltage-sensing domain. *Nature structural & molecular biology*, 21(3):244–252, 2014.

[115] J. T. Littleton and B. Ganetzky. Ion channels and synaptic organization: analysis of the Drosophila genome. *Neuron*, 26(1):35–43, 2000.

[116] J. Liu, M. Zhang, M. Jiang, and G.-N. Tseng. Negative charges in the transmembrane domains of the HERG K channel are involved in the activation-and deactivation-gating processes. *The Journal of general physiology*, 121(6):599–614, 2003.

[117] S. Liu, R. Rasmusson., D. Campbell, S. Wang, and H. Strauss. Activation and inactivation kinetics of an E-4031 sensitive current (I_{Kr}) from single ferret atrial myocytes. *Biophysical Journal*, 70:2704–2715, 1996.

[118] Y. Liu, M. Holmgren, M. E. Jurman, and G. Yellen. Gated access to the pore of a voltage-dependent K+ channel. *Neuron*, 19(1):175–184, 1997.

[119] S. B. Long, E. B. Campbell, and R. MacKinnon. Voltage sensor of Kv1. 2: structural basis of electromechanical coupling. *Science*, 309(5736):903–908, 2005.

[120] E. Loots and E. Isacoff. Protein rearrangements underlying slow inactivation of the Shaker K+ channel. *The Journal of general physiology*, 112(4):377–389, 1998.

[121] A. D. MacKerell Jr, D. Bashford, M. Bellott, R. L. Dunbrack Jr, J. D. Evanseck, M. J. Field, S. Fischer, J. Gao, H. Guo, S. Ha, et al. All-atom empirical potential for molecular modeling and dynamics studies of proteins. *The journal of physical chemistry B*, 102(18):3586–3616, 1998.

[122] A. D. MacKerell Jr, M. Feig, and C. L. Brooks. Improved treatment of the protein backbone in empirical force fields. *Journal of the American Chemical Society*, 126(3):698–699, 2004.

[123] R. MacKinnon. Potassium channels. *FEBS letters*, 555(1):62–65, 2003.

[124] M. G. Madej and C. M. Ziegler. Dawning of a new era in TRP channel structural biology by cryo-electron microscopy. *Pflügers Archiv-European Journal of Physiology*, 470(2):213–225, 2018.

[125] J. A. Maier, C. Martinez, K. Kasavajhala, L. Wickstrom, K. E. Hauser, and C. Simmerling. ff14SB: improving the accuracy of protein side chain and backbone parameters from ff99SB. *Journal of chemical theory and computation*, 11(8):3696–3713, 2015.

[126] O. A. Malak, Z. Es-Salah-Lamoureux, and G. Loussouarn. hERG S4-S5 linker acts as a voltage-dependent ligand that binds to the activation gate and locks it in a closed state. *Scientific reports*, 7(1):1–12, 2017.

[127] P. Mark and L. Nilsson. Structure and dynamics of the TIP3P, SPC, and SPC/E water models at 298 K. *The Journal of Physical Chemistry A*, 105(43):9954–9960, 2001.

[128] G. J. Martyna, D. J. Tobias, and M. L. Klein. Constant pressure molecular dynamics algorithms. *The Journal of chemical physics*, 101(5):4177–4189, 1994.

[129] S. Masnada, U. B. Hedrich, E. Gardella, J. Schubert, C. Kaiwar, E. W. Klee, B. C. Lanpher, R. H. Gavrilova, M. Synofzik, T. Bast, et al. Clinical spectrum and genotype–phenotype associations of KCNA2-related encephalopathies. *Brain*, 140(9):2337–2354, 2017.

[130] C. M. McBride, A. M. Smith, J. L. Smith, A. R. Reloj, E. J. Velasco, J. Powell, C. S. Elayi, D. C. Bartos, D. E. Burgess, and B. P. Delisle. Mechanistic basis for type 2 long QT syndrome caused by KCNH2 mutations that disrupt conserved arginine residues in the voltage sensor. *The Journal of membrane biology*, 246(5):355–364, 2013.

[131] J. T. Milnes, C. E. Dempsey, J. M. Ridley, O. Crociani, A. Arcangeli, J. C. Hancox, and H. J. Witchel. Preferential closed channel blockade of HERG potassium currents by chemically synthesised BeKm-1 scorpion toxin. *FEBS letters*, 547(1-3):20–26, 2003.

[132] W. E. Miranda, K. R. DeMarco, J. Guo, H. J. Duff, I. Vorobyov, C. E. Clancy, and S. Y. Noskov. Selectivity filter modalities and rapid inactivation of the hERG1 channel. *Proceedings of the National Academy of Sciences*, 117(6):2795–2804, 2020.

[133] J. S. Mitcheson, J. Chen, M. Lin, C. Culberson, and M. C. Sanguinetti. A structural basis for drug-induced long QT syndrome. *Proceedings of the National Academy of Sciences*, 97(22):12329–12333, 2000.

[134] J. Monod, J. Wyman, and J.-P. Changeux. On the nature of allosteric transitions: a plausible model. *J Mol Biol*, 12(1):88–118, 1965.

[135] N. Morrison-Levy, F. Borlot, P. Jain, and R. Whitney. Early-onset Developmental and Epileptic Encephalopathies of Infancy: An Overview of the Genetic Basis and Clinical Features. *Pediatric Neurology*, 2020.

[136] A. J. Moss, W. Zareba, E. S. Kaufman, E. Gartman, D. R. Peterson, J. Benhorin, J. A. Towbin, M. T. Keating, S. G. Priori, P. J. Schwartz, et al. Increased risk of arrhythmic events in long-QT syndrome with mutations in the pore region of the human ether-a-go-go–related gene potassium channel. *Circulation*, 105(7):794–799, 2002.

[137] A. Nardi and S.-P. Olesen. BK channel modulators: a comprehensive overview. *Current medicinal chemistry*, 15(11):1126–1146, 2008.

[138] M. T. Nelson, W. Humphrey, A. Gursoy, A. Dalke, L. V. Kalé, R. D. Skeel, and K. Schulten. NAMD: a parallel, object-oriented molecular dynamics program. *The International Journal of Supercomputer Applications and High Performance Computing*, 10(4):251–268, 1996.

[139] J. M. Nerbonne and R. S. Kass. Molecular physiology of cardiac repolarization. *Physiological reviews*, 85(4):1205–1253, 2005.

[140] Z. Niday and A. V. Tzingounis. Potassium channel gain of function in epilepsy: an unresolved paradox. *The Neuroscientist*, 24(4):368–380, 2018.

[141] R. Ocello, S. Furini, F. Lugli, M. Recanatini, C. Domene, and M. Masetti. Conduction and gating properties of the TRAAK channel from molecular dynamics simulations with different force fields. *Journal of chemical information and modeling*, 60(12):6532–6543, 2020.

[142] R. Olcese, R. Latorre, L. Toro, F. Bezanilla, and E. Stefani. Correlation between charge movement and ionic current during slow inactivation in Shaker K+ channels. *The Journal of general physiology*, 110(5):579–589, 1997.

[143] A. Pantazis, M. Kaneko, M. Angelini, F. Steccanella, A. M. Westerlund, S. H. Lindström, M. Nilsson, L. Delemotte, S. C. Saitta, and R. Olcese. Tracking the motion of the KV1. 2 voltage sensor reveals the molecular perturbations caused by a de novo mutation in a case of epilepsy. *The Journal of Physiology*, 598(22):5245–5269, 2020.

[144] J. B. Patlak. Cooperating to unlock the voltage-dependent K channel. *The Journal of general physiology*, 113(3):385–388, 1999.

[145] L. L. Perissinotti, P. M. De Biase, J. Guo, P.-C. Yang, M. C. Lee, C. E. Clancy, H. J. Duff, and S. Y. Noskov. Determinants of isoform-specific gating kinetics of hERG1 channel: combined experimental and simulation study. *Frontiers in physiology*, 9:207, 2018.

[146] E. Perozo, R. MacKinnon, F. Bezanilla, and E. Stefani. Gating currents from a nonconducting mutant reveal open-closed conformations in Shaker K+ channels. *Neuron*, 11(2):353–358, 1993.

[147] M. J. Perrin, P. W. Kuchel, T. J. Campbell, and J. I. Vandenberg. Drug binding to the inactivated state is necessary but not sufficient for high-affinity binding to human ether-a-go-go-related gene channels. *Molecular Pharmacology*, 74(5):1443–1452, 2008.

[148] M. Perry, M. J. de Groot, R. Helliwell, D. Leishman, M. Tristani-Firouzi, M. C. Sanguinetti, and J. Mitcheson. Structural determinants of HERG channel block by clofilium and ibutilide. *Molecular pharmacology*, 66(2):240–249, 2004.

[149] M. Perry, F. B. Sachse, J. Abbruzzese, and M. C. Sanguinetti. PD-118057 contacts the pore helix of hERG1 channels to attenuate inactivation and enhance K+ conductance. *Proceedings of the National Academy of Sciences*, 106(47):20075–20080, 2009.

[150] M. Perry, F. B. Sachse, and M. C. Sanguinetti. Structural basis of action for a human ether-a-go-go-related gene 1 potassium channel activator. *Proceedings of the National Academy of Sciences*, 104(34):13827–13832, 2007.

[151] C. J. Peters, D. Fedida, and E. A. Accili. Allosteric coupling of the inner activation gate to the outer pore of a potassium channel. *Scientific reports*, 3(1):1–8, 2013.

[152] K. Phan, C. A. Ng, E. David, D. Shishmarev, P. W. Kuchel, J. I. Vandenberg, and M. D. Perry. The S1 helix critically regulates the finely tuned gating of Kv11. 1 channels. *Journal of Biological Chemistry*, 292(18):7688–7705, 2017.

[153] J. C. Phillips, R. Braun, W. Wang, J. Gumbart, E. Tajkhorshid, E. Villa, C. Chipot, R. D. Skeel, L. Kale, and K. Schulten. Scalable molecular dynamics with NAMD. *Journal of computational chemistry*, 26(16):1781–1802, 2005.

[154] W. F. Pickard. Generalizations of the goldman-hodgkin-katz equation. *Mathematical biosciences*, 30(1-2):99–111, 1976.

[155] D. R. Piper, M. C. Sanguinetti, and M. Tristani-Firouzi. Voltage sensor movement in the hERG K+ channel. In *The hERG Cardiac Potassium Channel: Structure, Function and Long QT Syndrome: Novartis Foundation Symposium 266*, pages 46–56. Wiley Online Library, 2005.

[156] K. L. Poulsen, M. Hotait, K. Calloe, D. A. Klaerke, A. Rebeiz, G. Nemer, M. A. Tejada, and M. M. Refaat. The mutation p. T613A in the pore helix of the KV11. 1 potassium channel is associated with long QT syndrome. *Pacing and Clinical Electrophysiology*, 38(11):1304–1309, 2015.

[157] R. L. Rasmusson, M. J. Morales, S. Wang, S. Liu, D. L. Campbell, M. V. Brahmajothi, and H. C. Strauss. Inactivation of voltage-gated cardiac K+ channels. *Circulation research*, 82(7):739–750, 1998.

[158] M. Recanatini, E. Poluzzi, M. Masetti, A. Cavalli, and F. De Ponti. QT prolongation through hERG K+ channel blockade: current knowledge and strategies for the early prediction during drug development. *Medicinal research reviews*, 25(2):133–166, 2005.

[159] B. Rosati, P. Marchetti, O. Crociani, M. Lecchi, R. Lupi, A. Arcangeli, M. Olivotto, and E. Wanke. Glucose-and arginine-induced insulin secretion by human pancreatic β-cells: the role of HERG K+ channels in firing and release. *The FASEB Journal*, 14(15):2601–2610, 2000.

[160] R. Roth, D. Gillespie, W. Nonner, and R. E. Eisenberg. Bubbles, gating, and anesthetics in ion channels. *Biophysical journal*, 94(11):4282–4298, 2008.

[161] B. Roux, T. Allen, S. Berneche, and W. Im. Theoretical and computational models of biological ion channels. *Quarterly reviews of biophysics*, 37(1):15–103, 2004.

[162] L. Sala, Z. Yu, D. Ward-van Oostwaard, J. P. van Veldhoven, A. Moretti, K.-L. Laugwitz, C. L. Mummery, A. P. IJzerman, and M. Bellin. A new hERG allosteric modulator rescues genetic and drug-induced long-QT syndrome phenotypes in cardiomyocytes from isogenic pairs of patient induced pluripotent stem cells. *EMBO molecular medicine*, 8(9):1065–1081, 2016.

[163] M. Sanguinetti and Q. Xu. Mutations of the S4-S5 linker alter activation properties of HERG potassium channels expressed in Xenopus oocytes. *The Journal of Physiology*, 514(3):667–675, 1999.

[164] M. C. Sanguinetti. HERG1 channel agonists and cardiac arrhythmia. *Current opinion in pharmacology*, 15:22–27, 2014.

[165] M. C. Sanguinetti and J. S. Mitcheson. Predicting drug–hERG channel interactions that cause acquired long QT syndrome. *Trends in pharmacological sciences*, 26(3):119–124, 2005.

[166] M. C. Sanguinetti and M. Tristani-Firouzi. hERG potassium channels and cardiac arrhythmia. *Nature*, 440(7083):463–469, 2006.

[167] L. F. Santana, E. P. Cheng, and W. J. Lederer. How does the shape of the cardiac action potential control calcium signaling and contraction in the heart? *Journal of molecular and cellular cardiology*, 49(6):901, 2010.

[168] J. Schlitter, M. Engels, and P. Krüger. Targeted molecular dynamics: a new approach for searching pathways of conformational transitions. *Journal of molecular graphics*, 12(2):84–89, 1994.

[169] R. Schönherr and S. H. Heinemann. Molecular determinants for activation and inactivation of HERG, a human inward rectifier potassium channel. *The Journal of physiology*, 493(3):635–642, 1996.

[170] N. E. Schoppa, K. McCormack, M. A. Tanouye, and F. J. Sigworth. The size of gating charge in wild-type and mutant Shaker potassium channels. *Science*, 255(5052):1712–1715, 1992.

[171] S. Sharma. *Molecular dynamics simulation of nanocomposites using BIOVIA materials studio, lammps and gromacs*. Elsevier, 2019.

[172] M. Sheng and D. T. Pak. Ligand-gated ion channel interactions with cytoskeletal and signaling proteins. *Annual review of physiology*, 62(1):755–778, 2000.

[173] Y. P. Shi, S. Thouta, and T. W. Claydon. Modulation of hERG K+ channel deactivation by voltage sensor relaxation. *Frontiers in pharmacology*, 11:139, 2020.

[174] N. Shuichi. Constant temperature molecular dynamics methods. *Progress of Theoretical Physics Supplement*, 103:1–46, 1991.

[175] N. V. Shults, V. Rybka, Y. J. Suzuki, and T. I. Brelidze. Increased smooth muscle Kv11. 1 channel expression in pulmonary hypertension and protective role of Kv11. 1 channel blocker dofetilide. *The American Journal of Pathology*, 190(1):48–56, 2020.

[176] I. Splawski, J. Shen, K. W. Timothy, G. M. Vincent, M. H. Lehmann, and M. T. Keating. Genomic structure of three long QT syndrome genes: KVLQT1, HERG, andKCNE1. *Genomics*, 51(1):86–97, 1998.

[177] P. J. Stansfeld, P. Gedeck, M. Gosling, B. Cox, J. S. Mitcheson, and M. J. Sutcliffe. Drug block of the hERG potassium channel: insight from modeling. *Proteins: Structure, Function, and Bioinformatics*, 68(2):568–580, 2007.

[178] E. Suárez-Delgado, T. G. Rangel-Sandín, I. G. Ishida, G. E. Rangel-Yescas, T. Rosenbaum, and L. D. Islas. KV1. 2 channels inactivate through a mechanism similar to C-type inactivation. *Journal of General Physiology*, 152(6), 2020.

[179] R. N. Subbiah, C. E. Clarke, D. J. Smith, J. Zhao, T. J. Campbell, and J. I. Vandenberg. Molecular basis of slow activation of the human ether-a-go-go related gene potassium channel. *The Journal of physiology*, 558(2):417–431, 2004.

[180] A. Sula, J. Booker, L. C. Ng, C. E. Naylor, P. G. DeCaen, and B. A. Wallace. The complete structure of an activated open sodium channel. *Nature communications*, 8(1):1–9, 2017.

[181] J. Sun and R. MacKinnon. Cryo-EM structure of a KCNQ1/CaM complex reveals insights into congenital long QT syndrome. *Cell*, 169(6):1042–1050, 2017.

[182] S. Syrbe, U. B. Hedrich, E. Riesch, T. Djémié, S. Müller, R. S. Møller, B. Maher, L. Hernandez-Hernandez, M. Synofzik, H. S. Caglayan, et al. De novo loss-or gain-of-function mutations in KCNA2 cause epileptic encephalopathy. *Nature genetics*, 47(4):393–399, 2015.

[183] S. Thouta, C. M. Hull, Y. P. Shi, V. Sergeev, J. Young, Y. M. Cheng, and T. W. Claydon. Stabilization of the activated hERG channel voltage sensor by depolarization involves the S4-S5 linker. *Biophysical journal*, 112(2):300–312, 2017.

[184] S. Toyabe, T. Sagawa, M. Ueda, E. Muneyuki, and M. Sano. Experimental demonstration of information-to-energy conversion and validation of the generalized Jarzynski equality. *Nature physics*, 6(12):988–992, 2010.

[185] J. S. Trimmer and K. J. Rhodes. Localization of voltage-gated ion channels in mammalian brain. *Annu. Rev. Physiol.*, 66:477–519, 2004.

[186] M. Tristani-Firouzi, J. Chen, and M. C. Sanguinetti. Interactions between S4-S5 linker and S6 transmembrane domain modulate gating of HERG K+ channels. *Journal of Biological Chemistry*, 277(21):18994–19000, 2002.

[187] M. C. Trudeau, J. W. Warmke, B. Ganetzky, and G. A. Robertson. HERG, a human inward rectifier in the voltage-gated potassium channel family. *Science*, 269(5220):92–95, 1995.

[188] A. C. Van Slyke, S. Rezazadeh, M. Snopkowski, P. Shi, C. R. Allard, and T. W. Claydon. Mutations within the S4–S5 linker alter voltage sensor constraints in hERG K+ channels. *Biophysical journal*, 99(9):2841–2852, 2010.

[189] J. I. Vandenberg, M. D. Perry, M. J. Perrin, S. A. Mann, Y. Ke, and A. P. Hill. hERG K+ channels: structure, function, and clinical significance. *Physiological reviews*, 2012.

[190] V. Vardanyan and O. Pongs. Coupling of voltage-sensors to the channel pore: a comparative view. *Frontiers in Pharmacology*, 3:145, 2012.

[191] L. Verlet. Computer" experiments" on classical fluids. I. Thermodynamical properties of Lennard-Jones molecules. *Physical review*, 159(1):98, 1967.

[192] G. Vriend. WHAT IF: a molecular modeling and drug design program. *Journal of molecular graphics*, 8(1):52–56, 1990.

[193] H. Wang, D. Kunkel, P. A. Schwartzkroin, and B. L. Tempel. Localization of Kv1. 1 and Kv1. 2, two K channel proteins, to synaptic terminals, somata, and dendrites in the mouse brain. *Journal of Neuroscience*, 14(8):4588–4599, 1994.

[194] S. Wang, S. Liu, M. J. Morales, H. C. Strauss, and R. L. Rasmusson. A quantitative analysis of the activation and inactivation kinetics of HERG expressed in Xenopus oocytes. *The Journal of Physiology*, 502(1):45–60, 1997.

[195] W. Wang and R. MacKinnon. Cryo-EM structure of the open human ether-à-go-go-related K+ channel hERG. *Cell*, 169(3):422–430, 2017.

[196] Z. Wang, J. C. Hesketh, and D. Fedida. A high-Na+ conduction state during recovery from inactivation in the K+ channel Kv1. 5. *Biophysical Journal*, 79(5):2416–2433, 2000.

[197] A. D. Wei, G. A. Gutman, R. Aldrich, K. G. Chandy, S. Grissmer, and H. Wulff. International Union of Pharmacology. LII. Nomenclature and molecular relationships of calcium-activated potassium channels. *Pharmacological reviews*, 57(4):463–472, 2005.

[198] A. M. Westerlund, O. Fleetwood, S. Perez-Conesa, and L. Delemotte. Network analysis reveals how lipids and other cofactors influence membrane protein allostery. *The Journal of Chemical Physics*, 153(14):141103, 2020.

[199] J. R. Whicher and R. MacKinnon. Structure of the voltage-gated K+ channel Eag1 reveals an alternative voltage sensing mechanism. *Science*, 353(6300):664–669, 2016.

[200] S. H. Wright. Generation of resting membrane potential. *Advances in physiology education*, 28(4):139–142, 2004.

[201] E. L. Wu, X. Cheng, S. Jo, H. Rui, K. C. Song, E. M. Dávila-Contreras, Y. Qi, J. Lee, V. Monje-Galvan, R. M. Venable, et al. CHARMM-GUI membrane builder toward realistic biological membrane simulations, 2014.

[202] J. Wu, Z. Yan, Z. Li, X. Qian, S. Lu, M. Dong, Q. Zhou, and N. Yan. Structure of the voltage-gated calcium channel Cav1. 1 at 3.6 Å resolution. *Nature*, 537(7619):191–196, 2016.

[203] Y.-C. Yang, C.-J. Own, and C.-C. Kuo. A hydrophobic element secures S4 voltage sensor in position in resting Shaker K+ channels. *The Journal of physiology*, 582(3):1059–1072, 2007.

[204] W. N. Zagotta, T. Hoshi, J. Dittman, and R. W. Aldrich. Shaker potassium channel gating. II: Transitions in the activation pathway. *The Journal of general physiology*, 103(2):279–319, 1994.

[205] H. Zeng, I. M. Lozinskaya, Z. Lin, R. N. Willette, D. P. Brooks, and X. Xu. Mallotoxin is a novel human ether-a-go-go-related gene (hERG) potassium channel activator. *Journal of Pharmacology and Experimental Therapeutics*, 319(2):957–962, 2006.

[206] M. Zhang, J. Liu, M. Jiang, D.-M. Wu, K. Sonawane, H. Guy, and G.-N. Tseng. Interactions between charged residues in the transmembrane segments of the voltage-sensing domain in the hERG channel. *The Journal of membrane biology*, 207(3):169–181, 2005.

[207] M. Zhang, J. Liu, and G.-N. Tseng. Gating charges in the activation and inactivation processes of the HERG channel. *The Journal of general physiology*, 124(6):703–718, 2004.

[208] J. Zhou, C. E. Augelli-Szafran, J. A. Bradley, X. Chen, B. J. Koci, W. A. Volberg, Z. Sun, and J. S. Cordes. Novel potent human ether-a-go-go-related gene (hERG) potassium channel enhancers and their in vitro antiarrhythmic activity. *Molecular Pharmacology*, 68(3):876–884, 2005.

[209] Y. Zhou, J. H. Morais-Cabral, A. Kaufman, and R. MacKinnon. Chemistry of ion coordination and hydration revealed by a K+ channel–Fab complex at 2.0 Å resolution. *Nature*, 414(6859):43–48, 2001.